Chapter 3 Appendix 4

DELAYED GAMMA RAYS

Dean C. Kaul, Michael L. Gritzner, William H. Scott Jr.,
Farhad Dolatshahi, Stephen D. Egbert, and C. Woodrow Wilson
Science Applications International Corporation

Delayed gamma ray radiation is that component of initial nuclear weapon radiation emitted within the first 60 seconds following initiation by products of fission and of neutron activation that are parts of the debris of the nuclear explosion. The debris initially resides within the fireball, a luminous sphere of hot gases generated by the interaction with the air of x rays radiated from the hot debris within a millionth of a second after initiation.

The fireball also defines the edge of a region of very low density air created by the expansion of the very hot gases within. The high pressure region created at the edge of this density well forms the shock wave that breaks away from the fireball and travels outward, superimposed on the ambient air. The net effect of these perturbations is to decrease the amount of air on a line from the source to a target, thereby enhancing the transmission of delayed radiation over that which would occur in unperturbed air. This effect is often referred to as hydrodynamic enhancement.

The density well is buoyant and begins to rise within a fraction of a second of its creation. Its momentum is augmented by the returning shock wave, now reflected off the ground. The rise of the fireball, which includes the radiation source, causes the distance between source and target to increase, thereby causing the radiation transmission to decrease once the expansion of the fireball has slowed or stopped.

As the fireball rises the outer surface cools and is subject to drag forces from the surrounding atmosphere. The drag causes the spherical fireball to become a toroidal cloud of condensed gases, containing the weapon debris.

Throughout this process, the weapon debris, including the fission products, are in motion relative to the fireball. First, the debris are propelled toward the top of the fireball with an initial impulse provided by the reflected shock. Eventually the debris pierce the top of the rising fireball and flow down the side, with most becoming incorporated in the torus or in the cloud skirt below the torus. These effects become less pronounced as the scaled burst height increases, where the scaled burst height is defined to be the burst height divided by the yield to the one-third power (HOB $\div$ $y^{1/3}$).

This complex system, consisting of a radioactive, hence time-varying, source of gamma rays and similarly time-varying geometry, in which the amount of air between source and target is changing even as the source rises from its original location, must be modeled in some detail to describe properly the intensity of the delayed radiation component. The motive for doing so is that the delayed gamma radiation produces on the order of half the gamma-ray dose at Hiroshima and Nagasaki.

Three technical areas must be addressed in the modeling process. They are: (1) the fission product gamma-ray source, (2) gamma-ray transport, and (3) nuclear-weapon hydrodynamics. Data required for modeling the processes of interest in these areas have been acquired through laboratory and field measurements. However, these data are by no means complete. Here follows a discussion of such modeling as it affects the prediction of A-bomb survivor dose as computed using the 1986 Dosimetry System for Japanese A-bomb survivors (DS86).

Fission Product Gamma-ray Source

Measurements of gamma and beta radiation source rates as functions of time after fission have been made in the laboratory. Maienschein et al[1,2] reported measurements made in the late 1950s and early 1960s at Oak Ridge National Laboratory (ORNL) in terms of spectra and of total number and energy rates. In the early 1960s, Fisher and Engle[3,4] of Los Alamos National Laboratory performed similar experiments using a fast reactor, which allowed them to obtain results at very early times (0.35 seconds). They also performed such measurements for several fissionable materials including ^{235}U, ^{238}U, and ^{239}Pu.

Dickens et al[5,6] published results of recent measurements made at ORNL, including those of spectra, again using thermal neutron fission. Also, Japanese scientists Akiyama and An[7] published results of their measurements using a fast reactor. The Japanese data are in terms of total energy rate only and are limited to times of 20 seconds or greater.

Results of several measurements in terms of energy emission rates at 40 seconds, the earliest time common to all the available measurements, are provided in Table 1. There is a limit to what can be construed from these data because of the disparities in the uncertainties quoted by the individual measurers. The data of Maienschein et al are assigned a standard deviation of approximately 25%, those of Fisher and Engle 12% (^{235}U and ^{238}U) and 21% (^{239}Pu), and those of Dickens et al and Akiyama and An less than 5%. Nevertheless, the data having the lowest uncertainties are consistent with each other and are not inconsistent with the values provided by Maienschein et al, whereas the data of Fisher and Engle stand apart from the high precision data. Unfortunately, the latter provide the only available spectral data for very early times and for fission by ^{238}U. Therefore, it is desirable to reconcile them to those of the other measurers. To accomplish this, the spectra of Dickens et al and of Fisher and Engle were compared for ^{235}U and ^{239}Pu, common to both experiments (Table 2, columns 3 and 4). It was found that the two sets of spectra differ from each other by the same energy-dependent ratio (last column) after removal of a constant correction term in the Fisher and Engle measurement of ^{239}Pu (0.85, column 5). This correction is consistent with the Fisher and Engle disclaimer concerning their estimate of the number of fissions in the plutonium sample. The energy-dependent relationship found to exist between the Dickens et al and the Fisher and Engle ^{235}U and ^{239}Pu was applied to the latter's ^{238}U measurements. The results, in terms of total gamma-ray energy emission rate agrees within a few percent

Table 1. Energy Emission Rate of Gamma Rays (0.1 to 5 MeV) from Fission Products 40 Seconds after Fission

Nuclide Experimentor	MeV/s per Fission		
	^{235}U	^{238}U	^{239}Pu
Maienschein et al[1]	0.0193[a]	–	–
Fisher and Engle[4]	0.0216	0.0275	0.0194
Dickens et al[5]	0.0166	–	0.0130
Akiyama and An[7]	0.0171	0.0205	0.0131

[a]Energy contribution $0.1 < E < 0.28$ estimated by extrapolation.

Table 2. Mean Values of the Ratios of the Energy Emission Rates of Dickens to those of Fisher and Engle by Energy Group for ^{235}U and ^{239}Pu

Group	Upper Energy (MeV)	$S_D/S_{F\&E}$		$S_D/S_{F\&E}$		
		^{235}U	^{239}Pu	R_{239}/R_{235}[a]	^{239}Pu Adjusted	Mean
1	6.419	.394 (.179)[b]	.360 (.161)	.914	.424	.409 (.170)
2	5.636	.820 (.096)	.654 (.217)	.798	.769	.795 (.164)
3	4.918	.627 (.416)	.630 (.103)	1.005	.741	.684 (.281)
4	4.257	.866 (.095)	.734 (.059)	.848	.864	.865 (.079)
5	3.655	.958 (.048)	.817 (.044)	.853	.961	.960 (.046)
6	3.110	.852 (.076)	.730 (.031)	.857	.859	.856 (.058)
7	2.620	.904 (.046)	.779 (.025)	.862	.916	.910 (.037)
8	2.189	.869 (.028)	.738 (.026)	.849	.868	.869 (.027)
9	1.808	.779 (.034)	.674 (.045)	.865	.793	.786 (.040)
10	1.478	.787 (.049)	.688 (.033)	.874	.809	.798 (.042)
11	1.195	.722 (.044)	.615 (.035)	.852	.724	.723 (.040)
12	.954	.751 (.035)	.620 (.012)	.826	.729	.740 (.026)
13	.749	.674 (.100)	.515 (.084)	.764	.606	.640 (.093)
14	.575	.671 (.086)	.569 (.082)	.848	.669	.670 (.084)
15	.428	.577 (.106)	.495 (.104)	.858	.582	.580 (.105)
16	.309	.484 (.038)	.448 (.094)	.926	.527	.506 (.074)
17	.213	.394 (.077)	.345 (.160)	.876	.406	.400 (.127)
	.137		mean[c]	.854 (0.040)		

[a]Ratio of the ^{239}Pu source ratio to that of ^{235}U.
[b]Read as mean and (fractional standard deviation of the sample = σ_{n-1}/mean).
[c]Mean of group values $E < 4.257$ MeV.

with the value reported by Akiyama and An at 40 seconds postirradiation time. Therefore, it was concluded that a systematic error must be present in the Fisher and Engle data but that it can be removed through the use of the energy-dependent correction from Dickens et al. The resulting source rate models for three representative energy groups along with supporting experimental data are shown as a function of time in Figures 1 to 3.

Figure 3 also indicates some additional empirical correction represented by the dotted lines made to the Fisher and Engle data to make their temporal behavior self-consistent and also more consistent with those of Dickens et al. The resulting source rate models are not

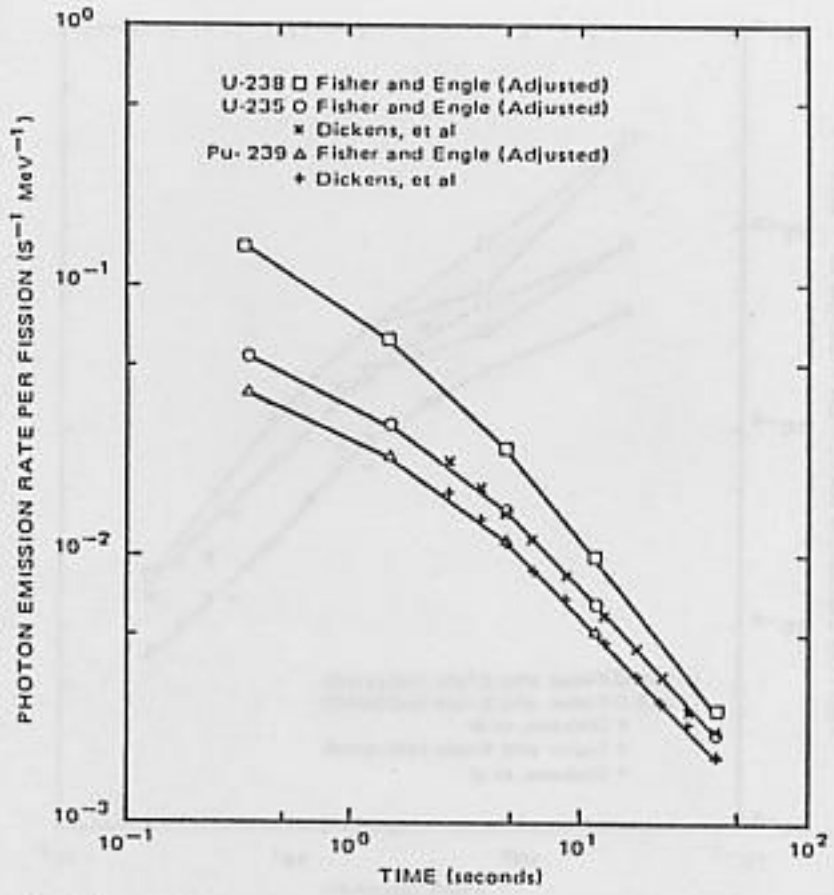

Figure 1. The emission rate versus time for gamma rays between 1.81 and 2.19 MeV from fission products of ^{235}U, ^{238}U, and ^{239}Pu

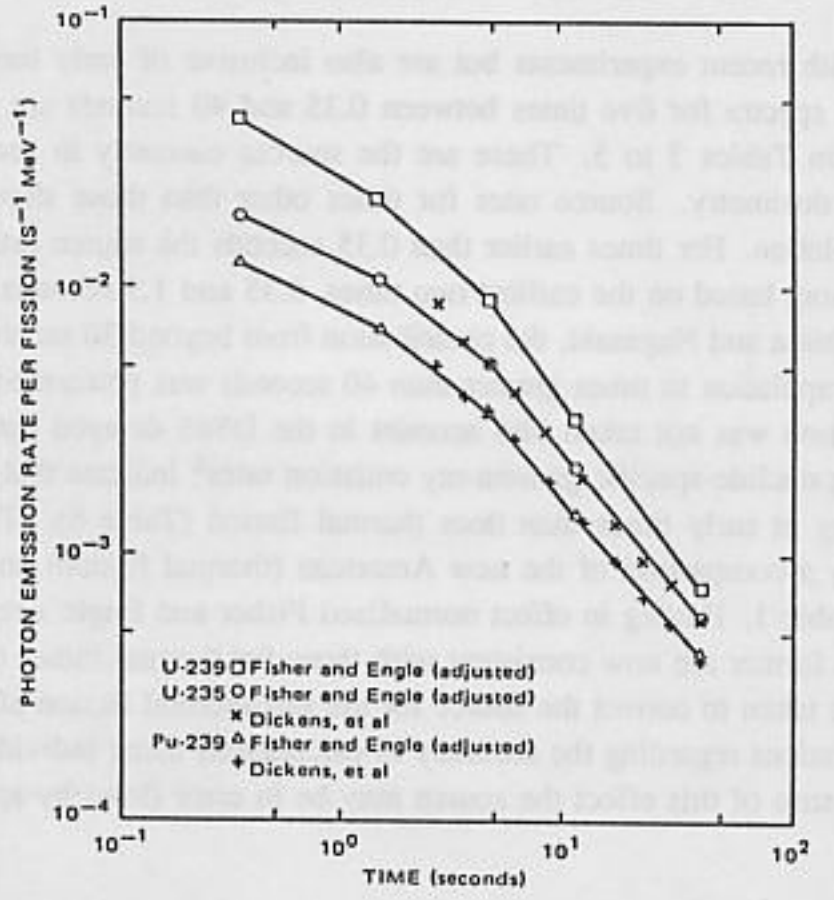

Figure 2. The emission rate versus time for gamma rays between 3.11 and 3.66 MeV from fission products of ^{235}U, ^{238}U, and ^{239}Pu

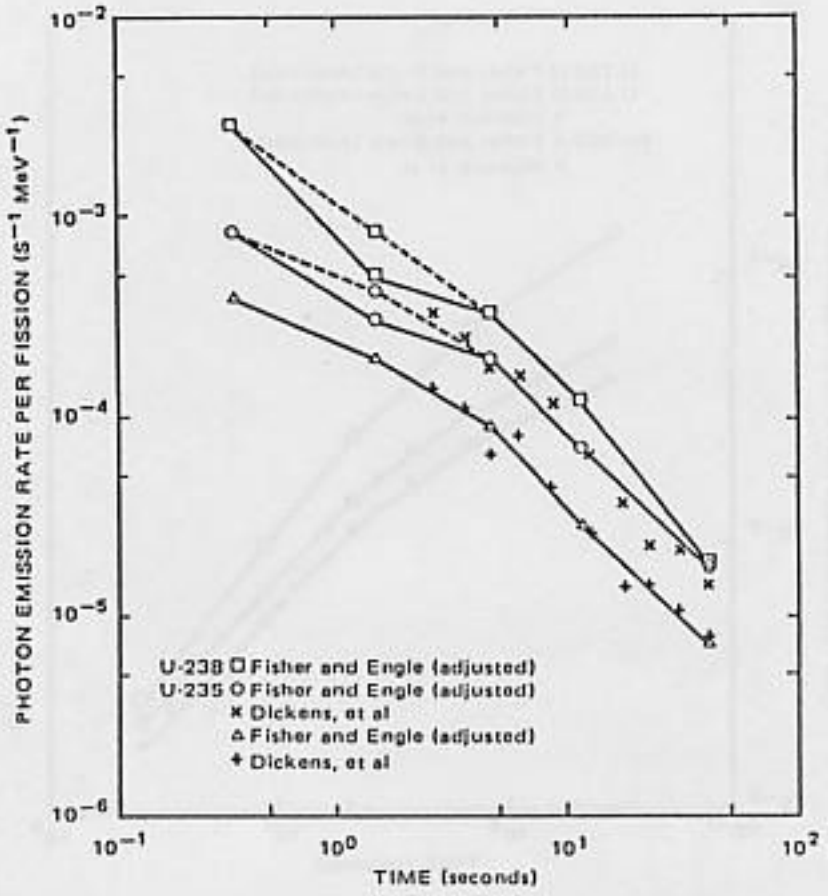

Figure 3. The emission rate versus time for gamma rays between 5.64 and 6.42 MeV from fission products of ^{235}U, ^{238}U, and ^{239}Pu

only consistent with recent experiments but are also inclusive of early times and data for ^{238}U. Source rate spectra for five times between 0.35 and 40 seconds are given for ^{235}U, ^{238}U, and ^{239}Pu in Tables 3 to 5. These are the sources currently in use for computing A-bomb survivor dosimetry. Source rates for times other than those shown are obtained by log-log interpolation. For times earlier than 0.35 seconds the source rate is obtained by log-log extrapolation, based on the earliest two times, 0.35 and 1.5 seconds. For the bombs exploded at Hiroshima and Nagasaki, the contribution from beyond 30 seconds is negligible. Therefore, no extrapolation to times greater than 40 seconds was performed.

One complication was not taken into account in the DS86 delayed gamma-ray model. Calculations using nuclide-specific gamma-ray emission rates[8] indicate that fast fission produces more energy at early times than does thermal fission (Table 6). This is supported to some extent by a comparison of the new American (thermal fission) and Japanese (fast fission) data in Table 1. Having in effect normalized Fisher and Engle's results to those of Dickens et al, the former are now consistent with those for thermal rather than fast fission.

No action was taken to correct the source for the fast-thermal fission effect at this time. This is due to questions regarding the accuracy of calculations using individual nuclide data. Nevertheless, because of this effect the source may be in error (low) by approximately 5% for all nuclides.

Gamma-ray Transport

The ability of current codes and cross sections to model gamma-ray transport in uniform

Table 3. Emission Rate Spectra for Gamma Rays from the Fission Products of ^{235}U at Mean Times after Fission of 0.35, 1.5, 4.75, 11.5, and 40 Seconds

Group	Upper Energy (MeV)	Gamma Rays/Fission-second-MeV				
		0.35	1.5	4.75	11.5	40.
1	14.0	0.0	0.0	0.0	0.0	0.0
2	10.0	0.0	0.0	0.0	0.0	0.0
3	8.0	5.50-5[a]	2.98-5	1.51-5	7.01-6	2.08-6
4	7.0	3.87-4	1.80-4	8.22-5	2.70-5	6.30-6
5	6.0	1.10-3	7.70-4	3.70-4	1.79-4	5.40-5
6	5.0	5.49-3	2.53-3	1.12-3	5.47-4	1.83-4
7	4.0	1.51-2	8.89-3	4.32-3	1.84-3	5.60-4
8	3.0	2.63-2	1.49-2	6.59-3	3.32-3	1.23-3
9	2.5	4.19-2	2.34-2	1.17-2	5.34-3	1.80-3
10	2.0	6.31-2	3.65-2	1.87-2	8.34-3	2.78-3
11	1.5	1.27-1	7.21-2	3.30-2	1.63-2	5.43-3
12	1.0	2.12-1	1.12-1	4.88-2	2.30-2	7.39-3
13	.70	2.66-1	1.61-1	8.90-2	3.91-2	9.20-3
14	.45	2.73-1	1.43-1	7.91-2	3.70-2	1.09-2
15	.30	4.08-1	1.85-1	1.08-1	5.06-2	1.35-2
16	.15	1.94-1	7.82-2	4.66-2	2.11-2	5.61-3
17	.10	0.0	0.0	0.0	0.0	0.0
18	.07	0.0	0.0	0.0	0.0	0.0
19	.045	0.0	0.0	0.0	0.0	0.0
20	.030	0.0	0.0	0.0	0.0	0.0
21	.020	0.0	0.0	0.0	0.0	0.0
	.010					

[a]Read as 5.5×10^{-5}

Table 4. Emission Rate Spectra for Gamma Rays from the Fission Products of ^{238}U at Mean Times after Fission of 0.35, 1.5, 4.75, 11.5, and 40 Seconds

Group	Upper Energy (MeV)	Gamma Rays/Fission-second-MeV				
		0.35	1.5	4.75	11.5	40.
1	14.0	0.0	0.0	0.0	0.0	0.0
2	10.0	0.0	0.0	0.0	0.0	0.0
3	8.0	1.26-4[a]	5.87-5	2.58-5	9.84-6	2.78-6
4	7.0	1.27-3	3.71-4	1.31-4	4.33-5	7.01-6
5	6.0	3.50-3	1.43-3	6.60-4	2.78-4	6.16-5
6	5.0	1.25-2	4.95-3	1.77-3	7.91-4	1.83-4
7	4.0	3.58-2	1.82-2	7.38-3	2.76-3	6.72-4
8	3.0	7.33-2	3.38-2	1.15-2	4.76-3	1.68-3
9	2.5	1.13-1	4.83-2	1.98-2	7.89-3	2.40-3
10	2.0	1.41-1	7.77-2	3.10-2	1.17-2	3.18-3
11	1.5	2.74-1	1.39-1	5.20-2	2.08-2	6.56-3
12	1.0	4.40-1	2.07-1	8.00-2	3.05-2	9.69-3
13	.70	5.61-1	2.80-1	1.44-1	5.30-2	1.35-2
14	.45	6.70-1	3.00-1	1.40-1	5.90-2	1.54-2
15	.30	9.99-1	4.01-1	2.07-1	7.38-2	2.00-2
16	.15	5.02-1	1.57-1	9.70-2	3.17-2	7.69-3
17	.10	0.0	0.0	0.0	0.0	0.0
18	.070	0.0	0.0	0.0	0.0	0.0
19	.045	0.0	0.0	0.0	0.0	0.0
20	.030	0.0	0.0	0.0	0.0	0.0
21	.020	0.0	0.0	0.0	0.0	0.0
	.010					

[a]Read as 1.26×10^{-4}

Table 5. Emission Rate Spectra for Gamma Rays from the Fission Products of ^{239}Pu at Mean Times after Fission of 0.35, 1.5, 4.75, 11.5, and 40 Seconds

Group	Upper Energy (MeV)	Gamma Rays/Fission-second-MeV				
		0.35	1.5	4.75	11.5	40.
1	14.0	0.0	0.0	0.0	0.0	0.0
2	10.0	0.0	0.0	0.0	0.0	0.0
3	8.0	4.56-5[a]	2.63-5	1.25-5	5.65-6	1.64-6
4	7.0	1.93-4	1.07-4	4.85-5	1.61-5	3.97-6
5	6.0	7.12-4	3.39-4	1.69-4	7.48-5	2.36-5
6	5.0	4.08-3	1.75-3	5.76-4	2.77-4	8.47-5
7	4.0	1.06-2	5.68-3	2.79-3	1.16-3	3.91-4
8	3.0	2.38-2	1.07-2	4.73-3	2.40-3	1.02-3
9	2.5	3.31-2	1.74-2	8.55-3	4.03-3	1.52-3
10	2.0	4.86-2	2.81-2	1.52-2	6.79-3	2.15-3
11	1.5	9.73-2	6.00-2	2.50-2	1.20-2	4.01-3
12	1.0	1.70-1	9.17-2	3.95-2	1.79-2	5.68-3
13	.70	2.43-1	1.68-1	8.06-2	3.27-2	7.58-3
14	.45	2.34-1	1.42-1	6.80-2	3.28-2	9.31-3
15	.30	3.57-1	1.82-1	9.91-2	4.63-2	1.08-2
16	.15	1.77-1	7.45-2	4.27-2	1.77-2	4.40-3
17	.10	0.0	0.0	0.0	0.0	0.0
18	.070	0.0	0.0	0.0	0.0	0.0
19	.045	0.0	0.0	0.0	0.0	0.0
20	.030	0.0	0.0	0.0	0.0	0.0
21	.020	0.0	0.0	0.0	0.0	0.0
	.010					

[a]Read as 4.56×10^{-5}

Table 6. Ratio of the Energy Emission Rates for Fission-product Gamma Rays for Fast- and Thermal-neutron Fission using ENDF/B-V

Time (seconds)	Nuclide	
	^{235}U	^{239}Pu
0.1	1.049	1.072
1.0	1.062	1.062
5.0	1.025	1.037
10.0	1.004	1.029
20.0	.993	1.020

air was tested using ^{60}Co measurements made at the BREN experiment (Figure 4).[9] The calculations were made for a source 343 m above ground using the two-dimensional discrete ordinates code (DOT)[10] with the 36 energy group Vitamin-C cross-section set.[11] Ideally, it would be desirable to use the DOT code to calculate the delayed radiation transport. However, because the debris-fireball-ground geometry is dynamic, it would require 30 or more separate calculations to adequately represent the propagation of delayed radiation from either the Hiroshima or Nagasaki weapons. Therefore, an alternative method was found that provides a more practical approach to the problem. According to this approach the gamma-

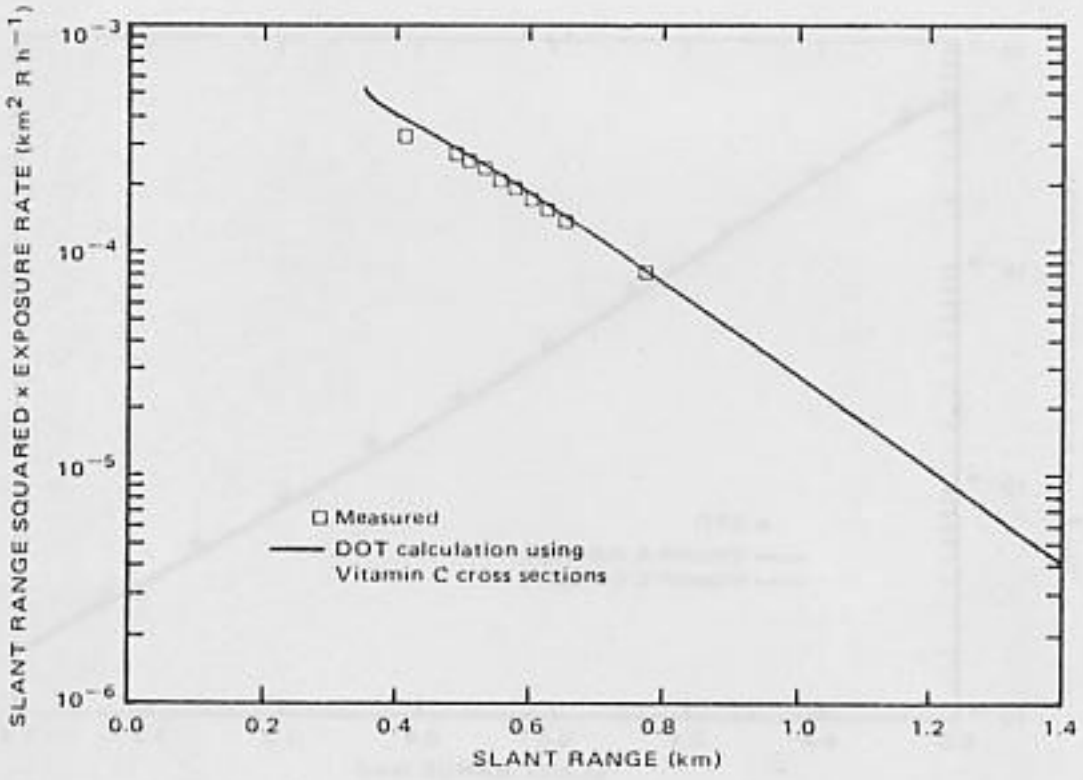

Figure 4. The dose (at 1 m above the ground) due to ^{60}Co gamma rays at the BREN experiment

ray transport is modeled in a one-dimensional system of uniform air. The amount of air along a line from the debris (the gamma-ray source) to the target at a specific time is determined using a hydrodynamic model, which will be discussed later in this section. The energy- and angle-differential fluence rate at the target is determined for the time-specific source rate spectrum transported through an identical thickness of air, using the data base for transport through uniform air. This substitution of uniform for perturbed air is a good approximation for gamma rays, the transport of which is dominated by absorption and forward scattering.

An early version of the data base for uniform air was produced with the Air Transport of Radiation (ATR) code.[12] These data were shown to be in error when compared with those generated using the more recent Vitamin-C cross sections,[11] as shown in Figure 5. The current data base was developed using the latest cross-section set, Vitamin-E,[13] the results of which agree well with those calculated using Vitamin-C, as shown in Figure 5.

A single data base for the one-dimensional transport of gamma rays in uniform air was developed to serve for both Japanese cities, because they have the same ratio of densities of water vapor to moist air (0.016). Calculations of energy- and angle-differential fluence of gamma rays as a function of distance through 342 g cm^{-2} (approximately 3000 m) were performed for sources in each of the 38 Vitamin-E energy groups, as shown in Table 7. The calculations were made using an S_{40} quadrature and a P_3 Legendre scattering representation. The results of the calculations were collapsed into the 21 gamma-ray energy groups of the DLC-31 energy structure common to the remainder of the dosimetry system.[14] That structure is also shown in Table 7. The collapsing procedure was performed using the energy rate spectrum of the gamma rays one second after fission of ^{235}U as a source weighting function. Approximately one third of the delayed radiation component is received at a target in that amount of time.

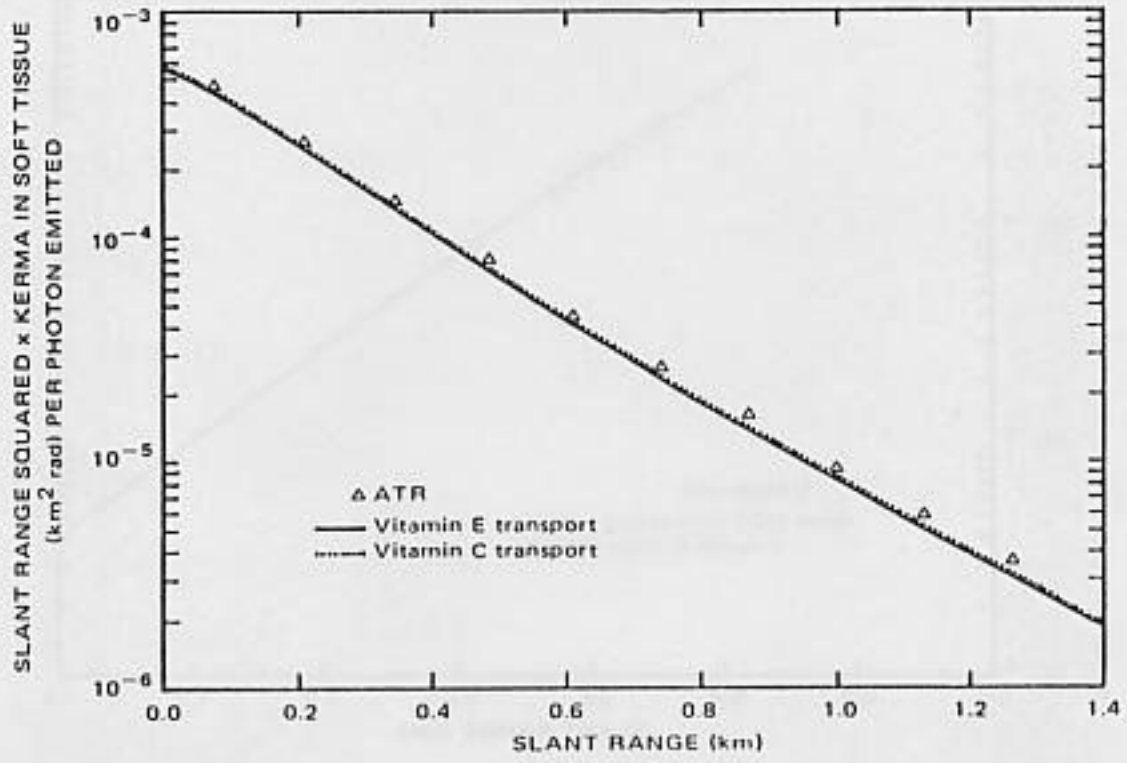

Figure 5. Comparison of calculations of gamma-ray kermas made with different cross-section libraries - uniform-air geometry, Fisher and Engle ^{235}U fission product source at one second

Table 7. The Energy-group Structures of the Vitamin E and DLC-31 Gamma-ray Cross-section Libraries

Upper Energy (MeV)	Vitamin E Group	DLC-31 Group
2.00 + 1[a]	1	
1.40 + 1	2	1
1.20 + 1	3	
1.00 + 1	4	2
8.00 + 0	5	3
7.50 + 0	6	
7.00 + 0	7	4
6.50 + 0	8	
6.00 + 0	9	5
5.50 + 0	10	
5.00 + 0	11	6
4.50 + 0	12	
4.00 + 0	13	7
3.50 + 0	14	
3.00 + 0	15	8
2.50 + 0	16	9
2.00 + 0	17	10
1.66 + 0	18	
1.50 + 0	19	11
1.33 + 0	20	
1.00 + 0	21	12
8.00 – 1	22	
7.00 – 1	23	13
6.00 – 1	24	
5.12 – 1	25	
5.10 – 1	26	
4.50 – 1	27	14
4.00 – 1	28	
3.00 – 1	29	15
2.00 – 1	30	
1.50 – 1	31	16
1.00 – 1	32	17
7.50 – 2	33	
7.00 – 2	34	18
6.00 – 2	35	
4.50 – 2	36	19
3.00 – 2	37	20
2.00 – 2	38	21
Lower Bound 1.00–2	28	21

[a]Read as 2.0×10^1

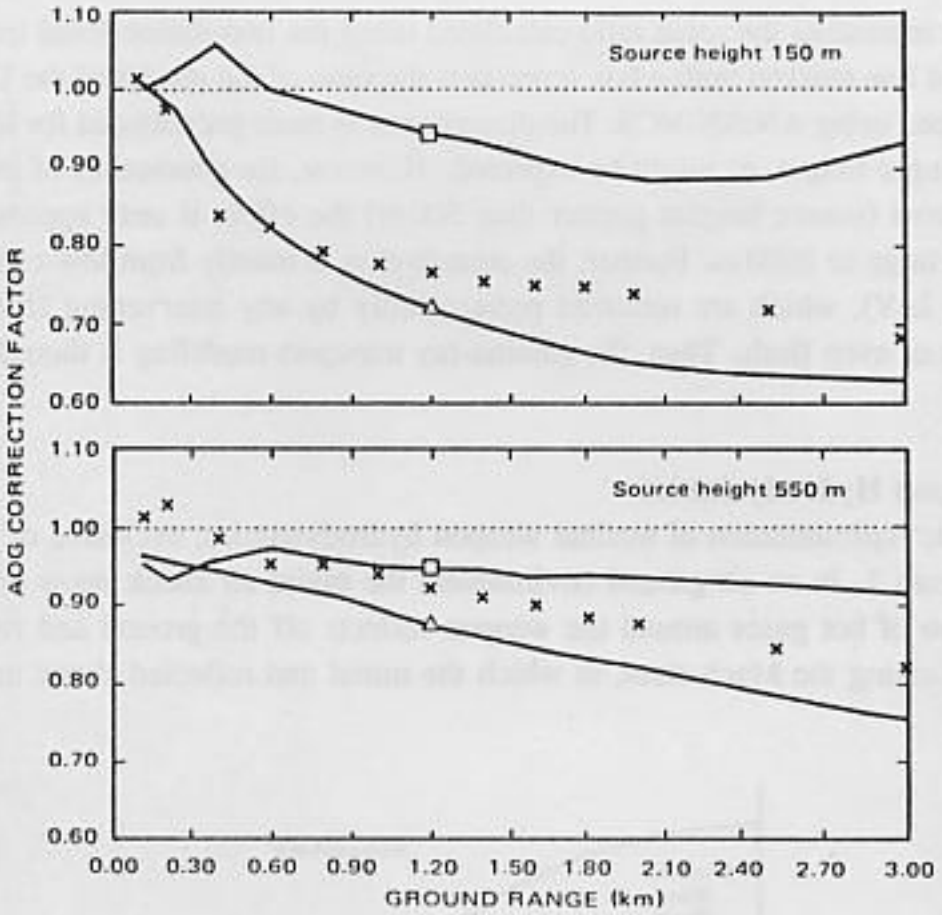

Figure 6. Ratio of the kerma produced by gamma rays from fission products in an air-over-ground (AOG) geometry to that in a uniform-air geometry (the AOG correction factor) as calculated with a two-dimensional code (△) and by modified one-dimensional methods (×). Ratio of the 2-D to 1-D results(○). Two source heights, 150 m and 500 m

The effect of the ground on gamma-ray transport was taken into account using the armored vehicles code system (VCS),[15] inserting ground into the 1-D field as if it were a shielding medium. Such perturbation is necessary to produce energy- and angle-differential fluences next to the air/ground interface equivalent to those produced for the prompt and secondary radiation components using the DOT code. The VCS code sytem[15] was used to create the perturbed fluence, based on the uniform air transport data generated with anisotropic scattering (ANISN)[16] and the adjoint fluence leaking from the air volume above the ground surface, as computed using MORSE.[17]

The ANISN-VCS approach was chosen because it represents a considerable computational timesaving over the alternative of performing a DOT calculation at every time step in the development of the fireball-debris cloud geometry. However, because the ground, so modeled, must of necessity be of rather small extent, several tens of meters at most, the method is not able to eliminate photons that scatter below the effective ground plane and return to contribute to the fluence above the ground. This has the effect of allowing the method to overestimate the total fluence. This effect is illustrated in Figure 6 for source heights of 150 and 500 m. The stars represent the ratio of the kerma calculated with the ground present to that calculated without the ground using the ANISN-VCS method. The solid line marked

by the triangle represents the same ratio calculated using the two-dimensional transport code DOT. The solid line marked with a box represents the ratio of the results of the DOT method to those produced using ANISN-VCS. The discrepancy is more pronounced for lower heights of burst and longer ranges, as might be expected. However, for geometries of interest to the A-bomb survivors (source heights greater than 500 m) the effect is only approximately 6% at distances as large as 2000 m. Further, the contribution is mainly from low-energy photons (less than 500 keV), which are removed preferentially by any intervening shield material, such as houses or even flesh. Thus, the gamma-ray transport modeling is thought to be well in hand.

Nuclear Weapon Hydrodynamics

A schematic representation of nuclear weapon hydrodynamics, exclusive of fireball rise, is given in Figure 7. In an air-ground environment the initial air shock wave created by the rapid expansion of hot gases around the weapon reflects off the ground and rises after the initial wave, forming the Mach stem, in which the initial and reflected shock unite.

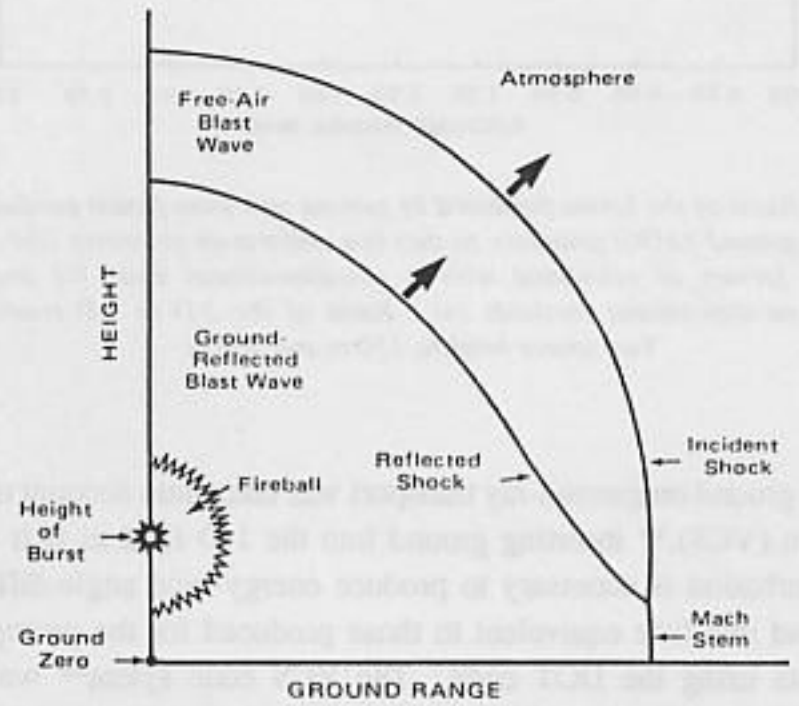

Figure 7. Principal physical features of a nuclear blast wave reflected from a plane ground surface

Observations of field tests and small scale high explosive experiments have been used to develop large empirical and semiempirical models of weapon hydrodynamics. These are embodied in computer codes which are by and large too cumbersome for use in conjunction with transport data for delayed gamma-ray modeling. However, small codes that scale data generated by more complex models have been developed. STLAMB, a more recent variant[18] of the Low Altitude Multiple Burst (LAMB) model developed by Needham and Wittwer[19] is one of these. This code interpolates between and extrapolates from hydrodynamic data obtained from model calculations for 1 kt and 1 Mt yields in uniform air. It accounts for the

presence of the ground and, hence, the reflected shock by means of an image burst below the ground plane. This method does not produce results that are entirely correct. For instance no Mach stem is formed. However, in the case of the Hiroshima and Nagasaki devices the burst heights were sufficiently high relative to the yields that the effects of the ground are small. STLAMB is used as the hydrodynamic model in the delayed gamma radiation system used to calculate survivor doses. As such, it computes air density profiles as a function of time and computes the amount of air between the source and detector. It also calculates cloud rise.

Figures 8 to 14 show the development of the system of hydrodynamically perturbed air surrounding the Plumbbob Shot Hood, a 71 kt burst at 457 m, as modeled using STLAMB. Time-dependent gamma-ray kerma measurements were made on this test[20] that can be used to help validate the delayed gamma-ray model. The development of the weapon hydrodynamic process includes a spherical density well, which is later perturbed by the reflected shock front. By one second the reflected shock is shown to be passing through the approximate center of the original fireball region. Thereafter, the shock moves rapidly above the now rising fireball, which eventually forms a toroidal system and moves well above its starting point.

Figures 15 to 22 show a similar progression for Shot Owens, a 9.7 kt burst at 155 m, also a subject of gamma-ray kerma-rate measurements along with a very similar Shot Wilson (10.3 kt, 155 m). In this case the reflected shock is moving back through the fireball less

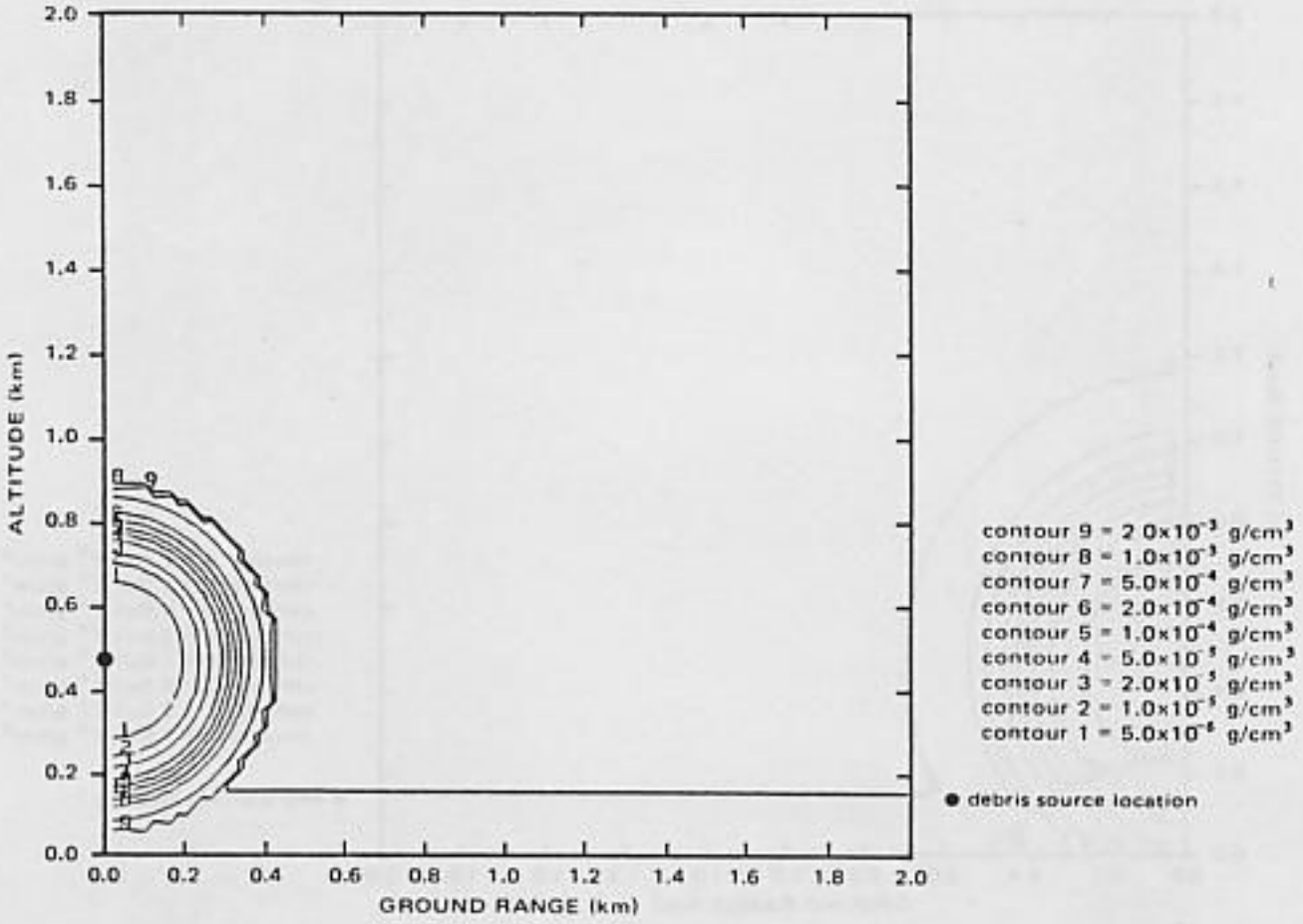

Figure 8. Iso-contours of air density at Shot Hood 0.221 seconds after the explosion

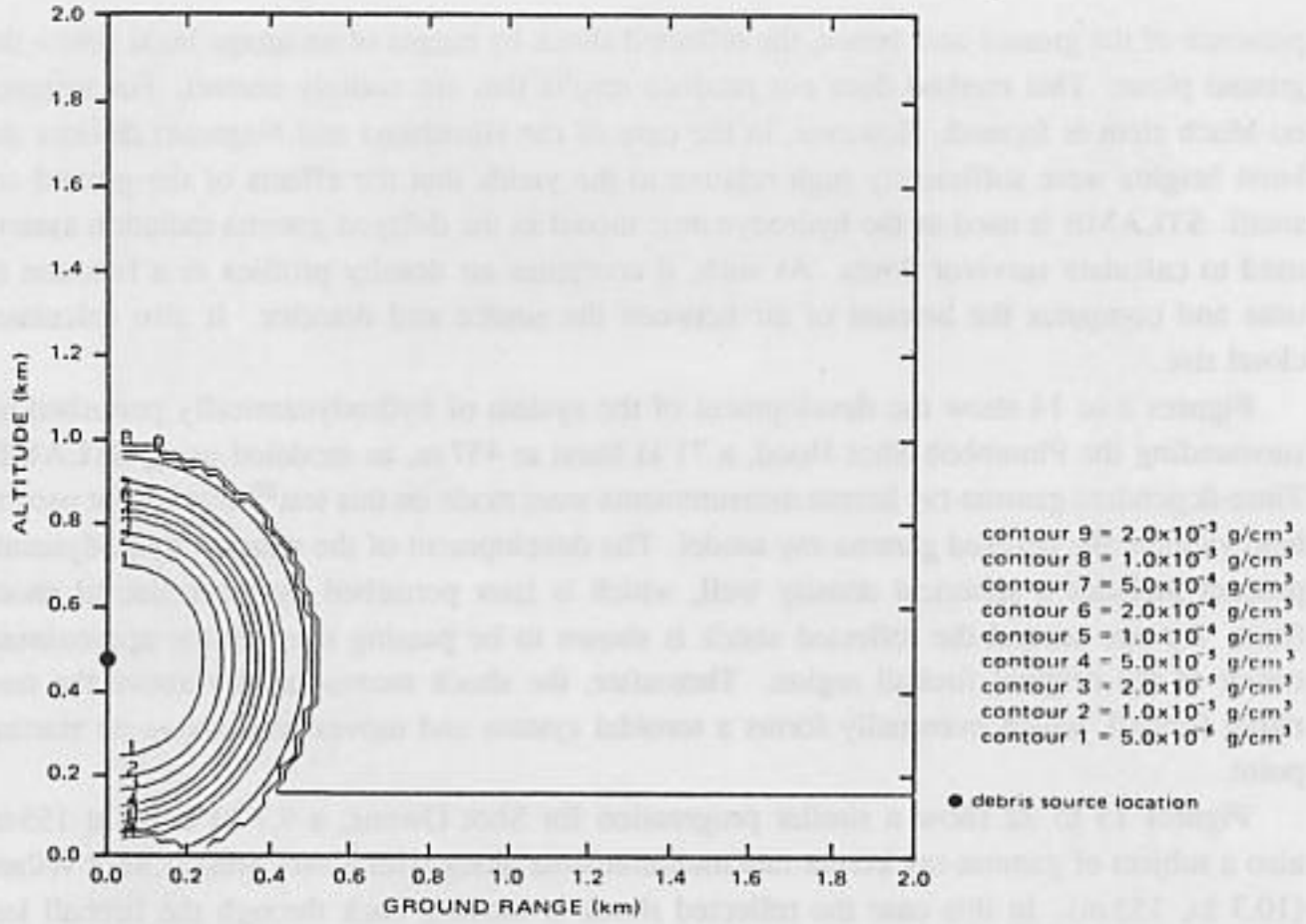

Figure 9. Iso-contours of air density at Shot Hood 0.354 seconds after the explosion

Figure 10. Iso-contours of air density at Shot Hood 0.662 seconds after the explosion

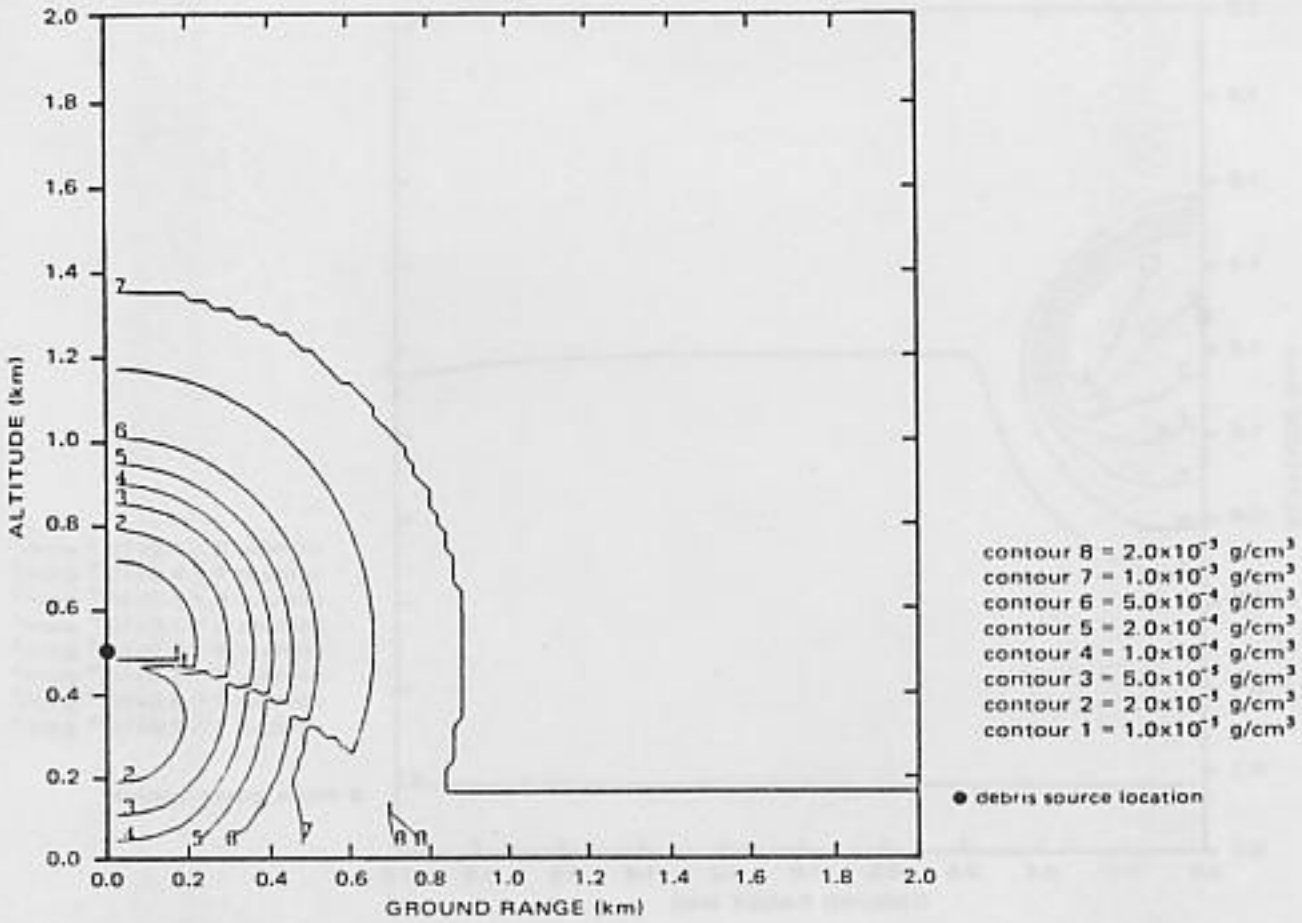

Figure 11. Iso-contours of air density at Shot Hood 1.034 seconds after the explosion

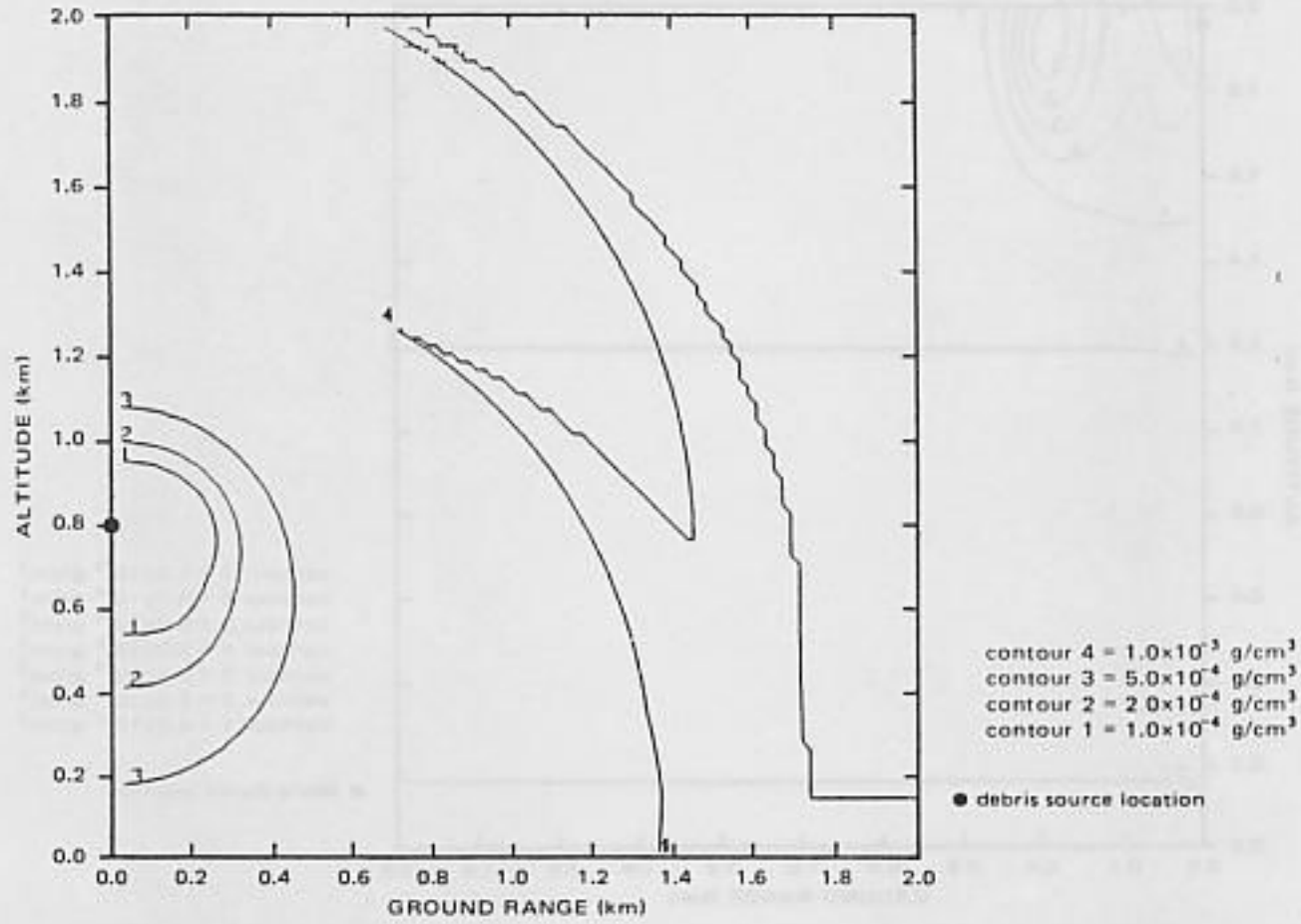

Figure 12. Iso-contours of air density at Shot Hood 3.067 seconds after the explosion

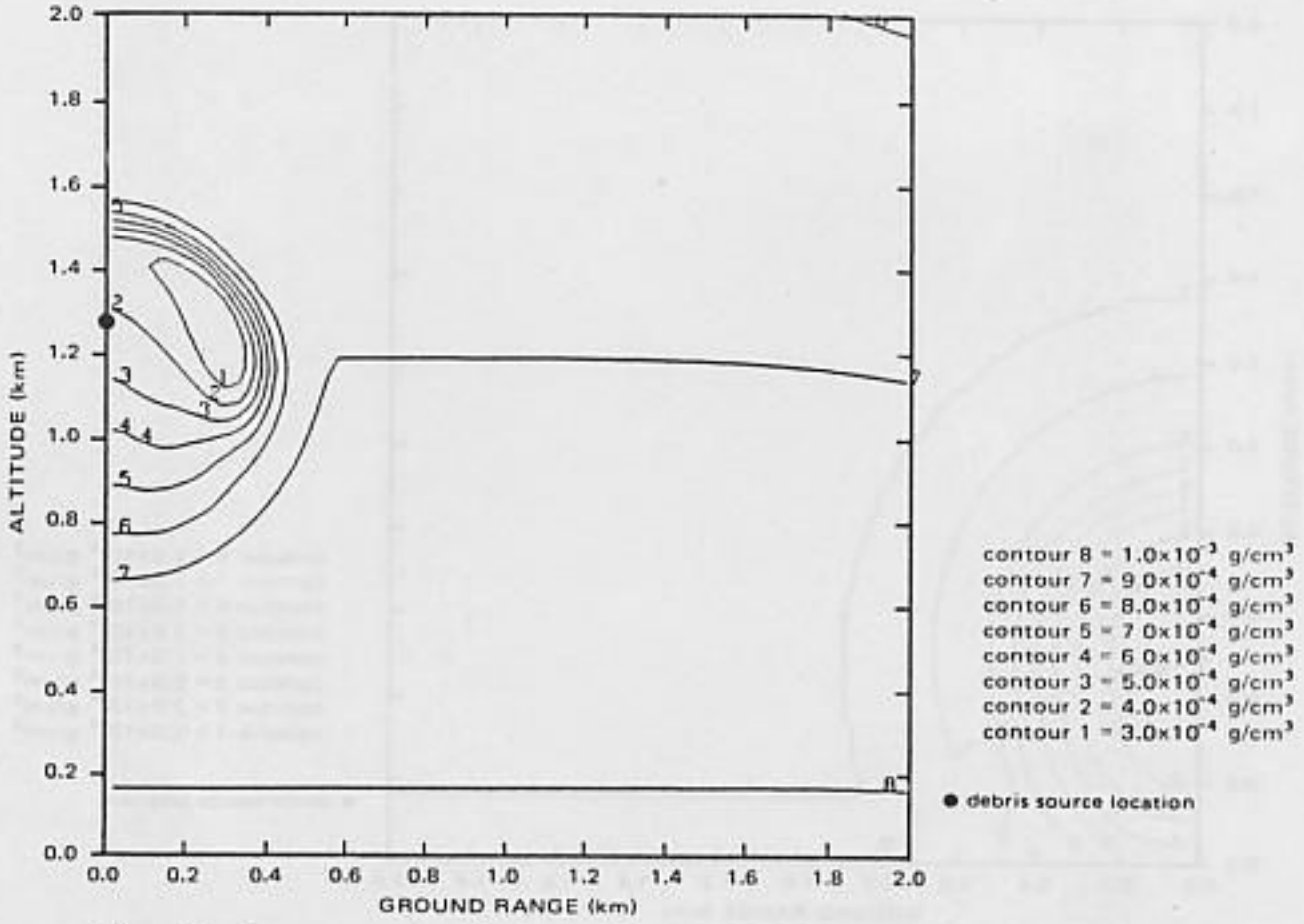

Figure 13. Iso-contours of air density at Shot Hood 9.725 seconds after the explosion

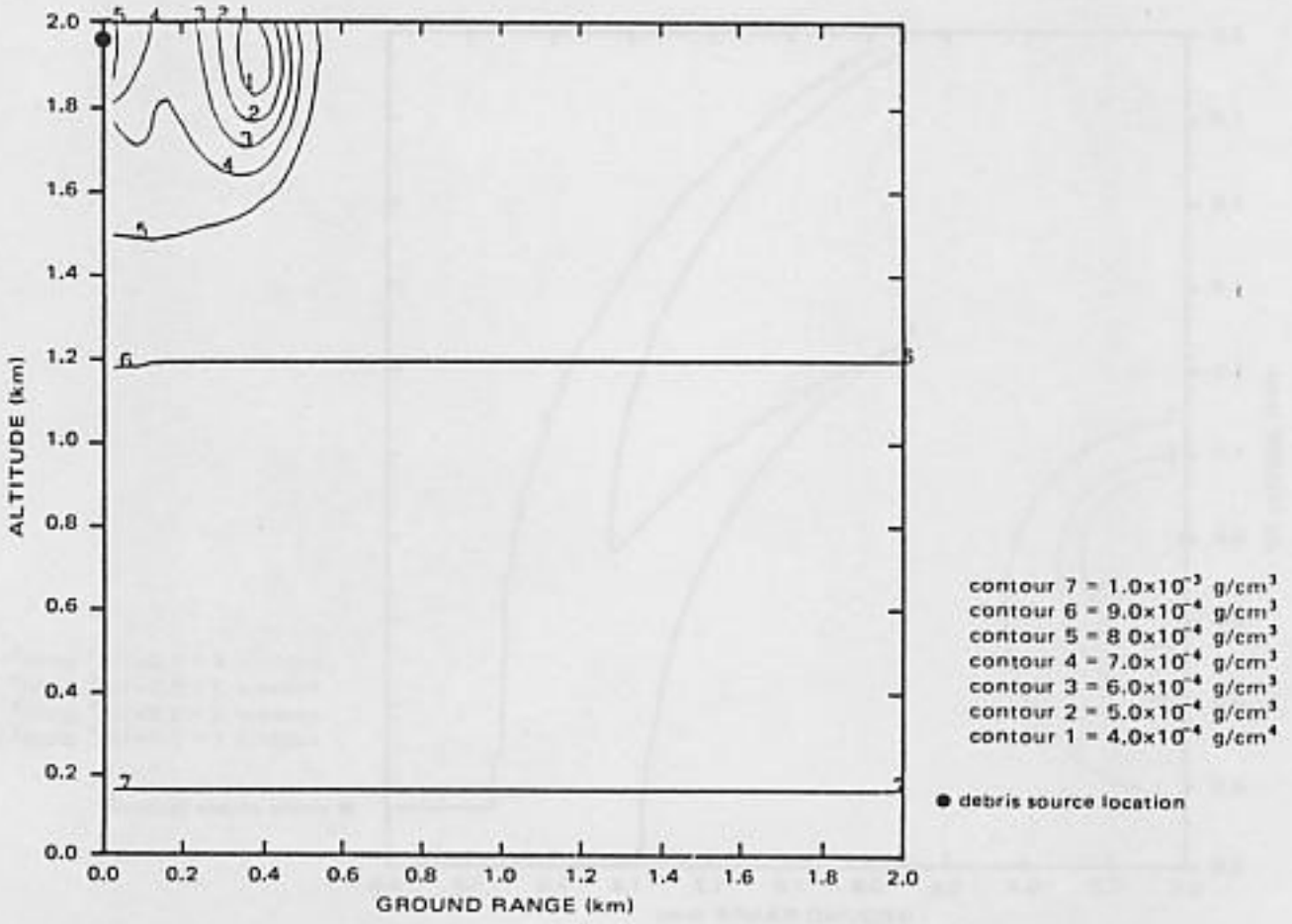

Figure 14. Iso-contours of air density at Shot Hood 20.004 seconds after the explosion

than a tenth of a second after its initiation. By one second it has passed entirely through the fireball. It is shown to proceed to form a torus similar to that of Hood.

The depictions of density profiles have been created with data from STLAMB and, thus, are the basis for determining the thickness and length of the transport path from source to detector. STLAMB also computes the location of the highest temperature in the system, which may be associated with the debris. However, the debris is probably distributed over a larger volume within the fireball. In fact, observations of field tests suggest that the debris actually flows within the fireball, at first to the top, later down the sides, and finally into the torus and skirt. Unfortunately, there are not sufficient data to construct a model of this cloud geometry-debris location system applicable to the Hiroshima and Nagasaki detonations on the basis of actual observations. Thus, the present delayed radiation model was developed under the assumption that the debris resides at the altitude of the hot spot but at a point on the centerline of the system rather than distributed as a sphere or torus. This assumption was made to simplify the calculation process and to keep the running time of the computer model to a reasonable level. However, the effect of moving the source to other locations was examined. Calculations were made for debris locations on the centerline but high, 0.8 of the fireball radius above the center of the fireball, and low, 0.8 of the fireball radius below the center of the fireball. Calculations using these alternative, though not necessarily realistic, debris locations were made for comparison with experimental measurements and to determine the sensitivity of the delayed gamma-ray fields to such perturbations.

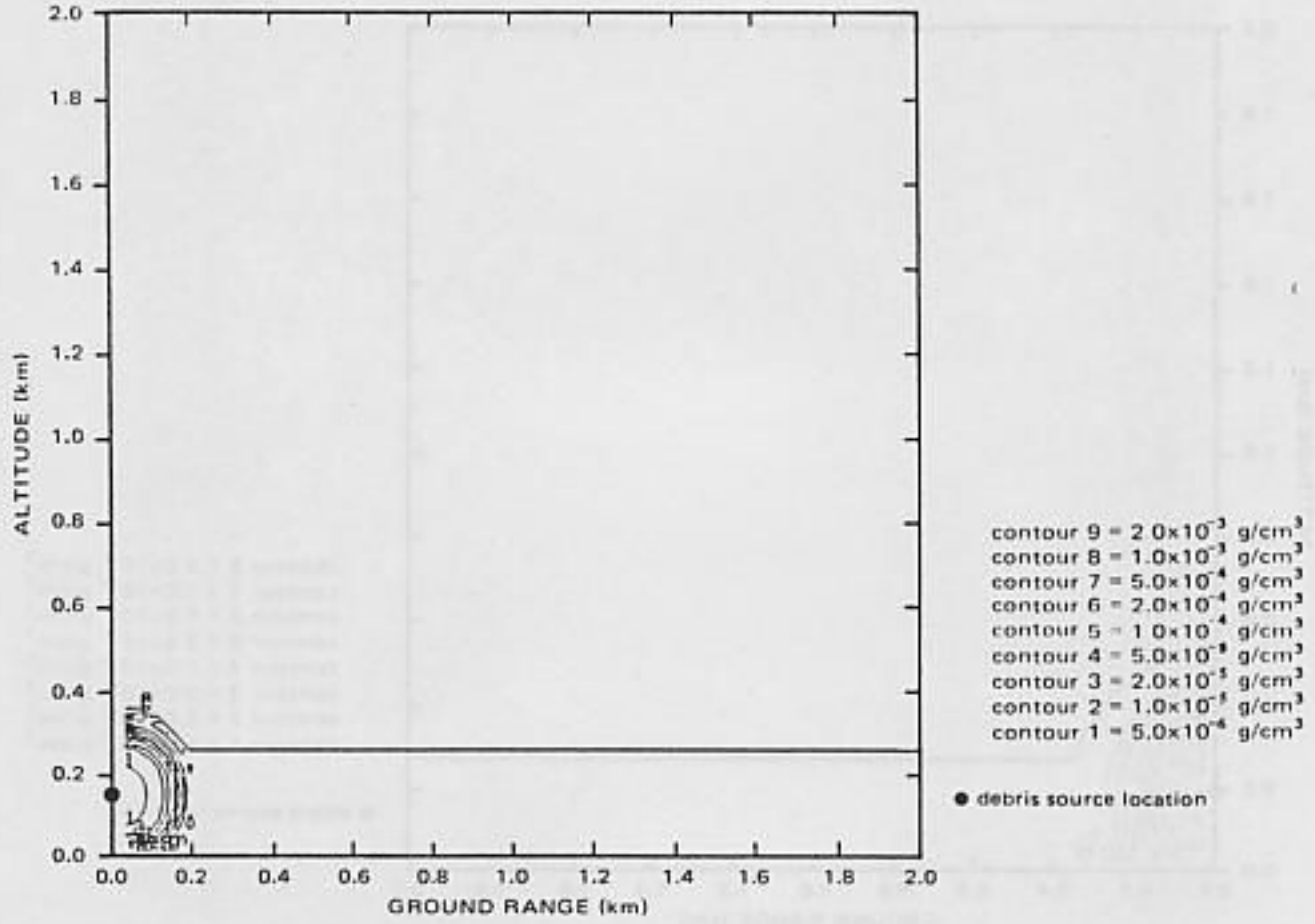

Figure 15. Iso-contours of air density at Shot Owens 0.100 seconds after the explosion

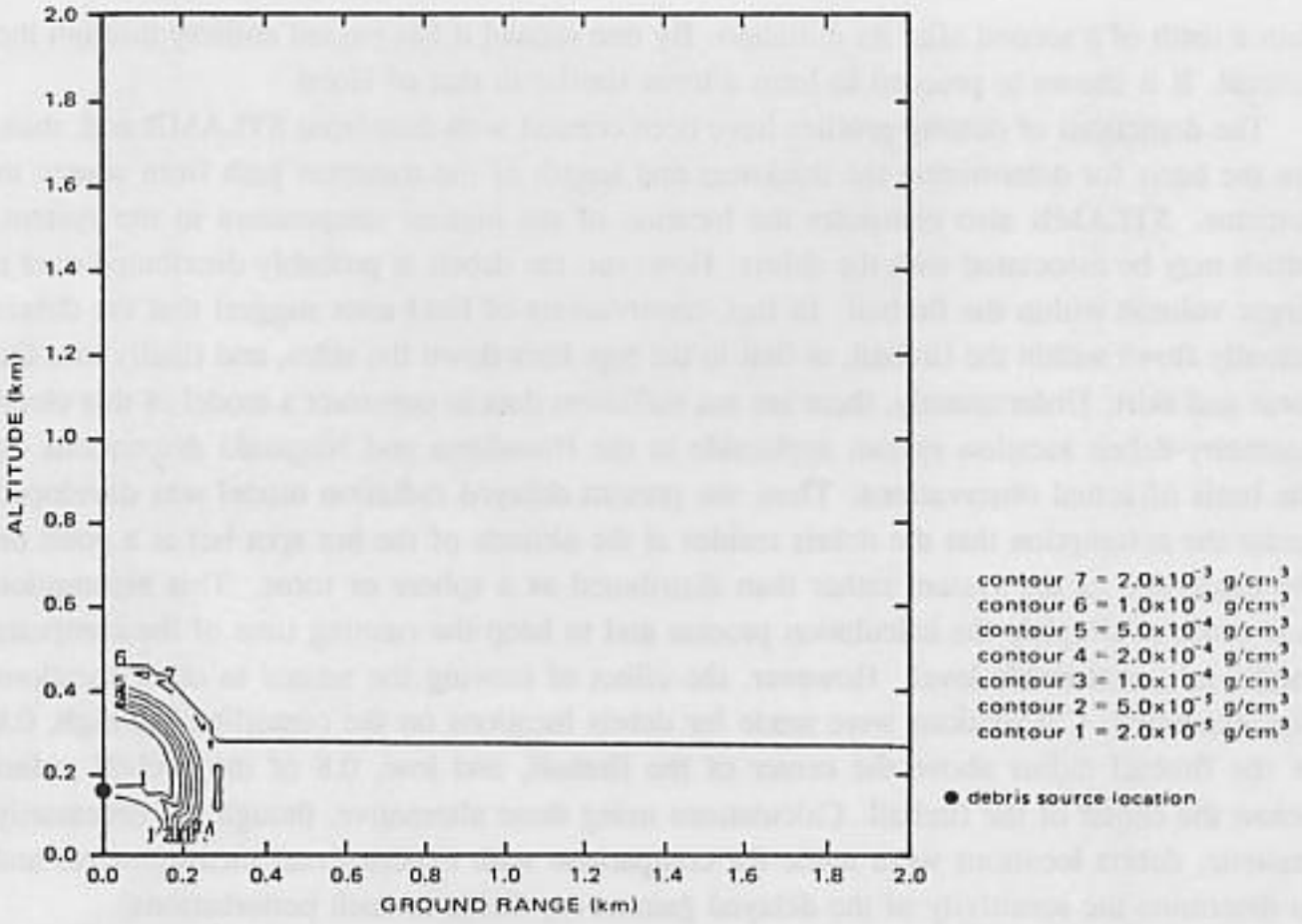

Figure 16. Iso-contours of air density at Shot Owens 0.221 seconds after the explosion

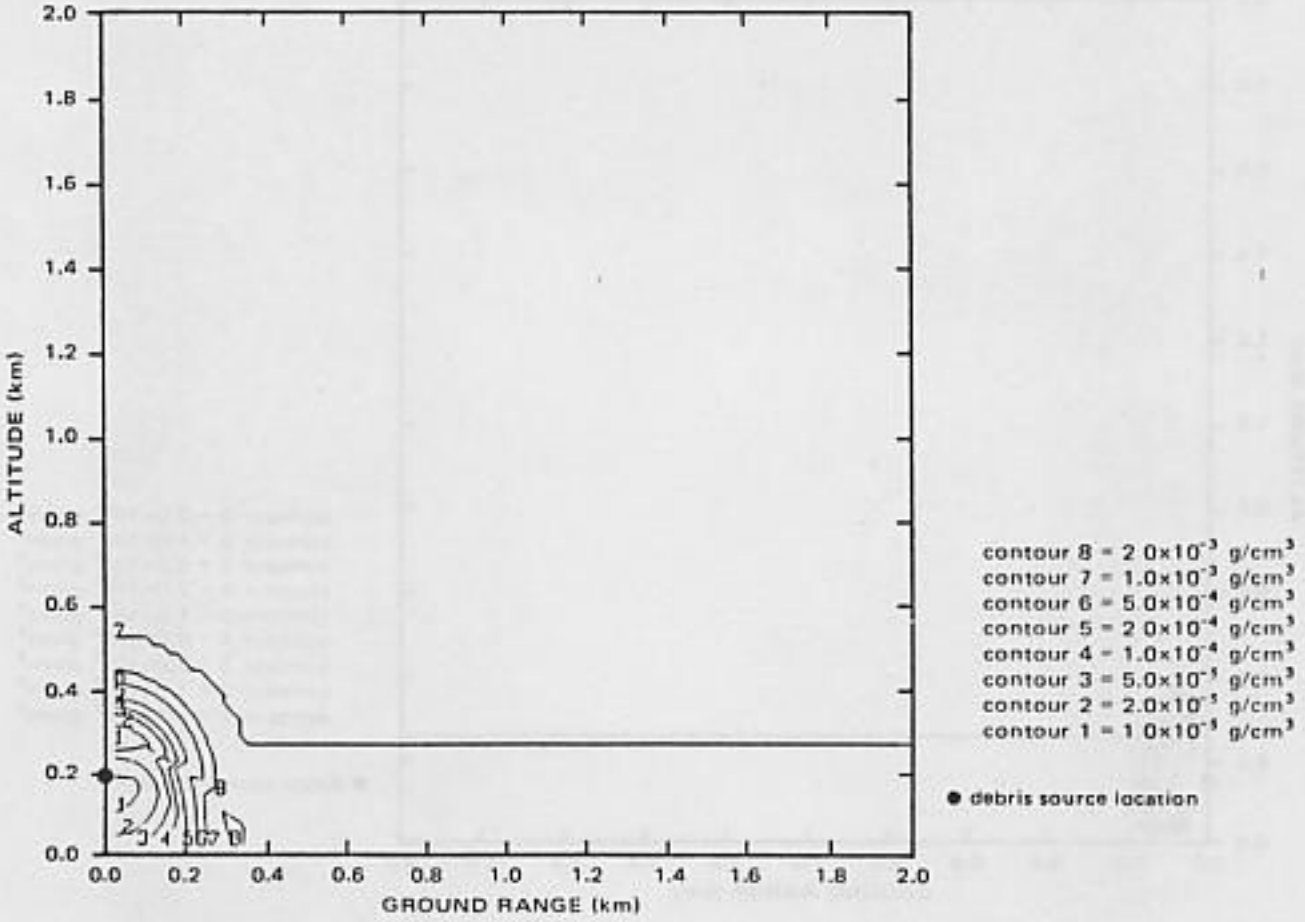

Figure 17. Iso-contours of air density at Shot Owens 0.354 seconds after the explosion

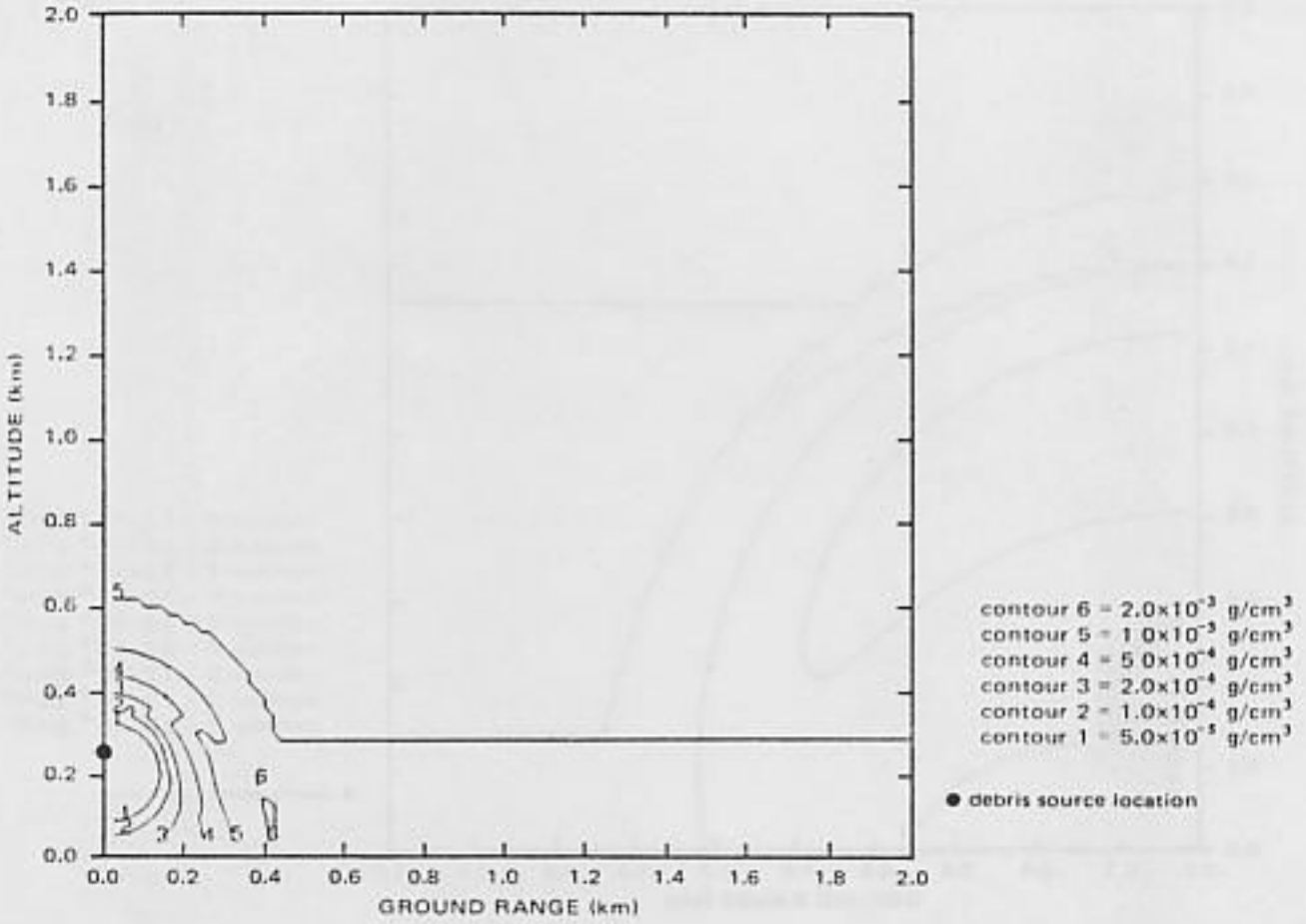

Figure 18. Iso-contours of air density at Shot Owens 0.501 seconds after the explosion

Figure 19. Iso-contours of air density at Shot Owens 1.034 seconds after the explosion

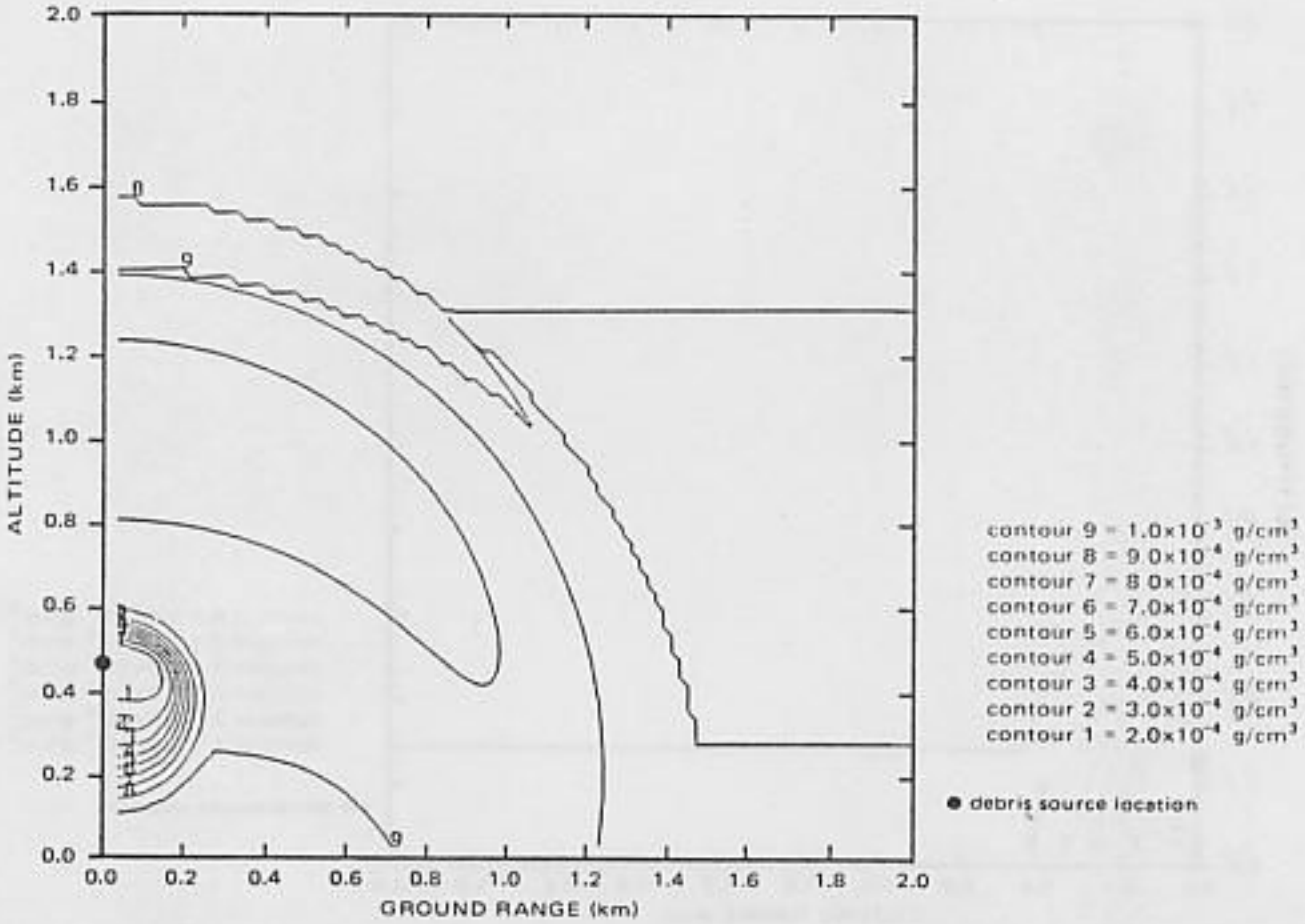

Figure 20. Iso-contours of air density at Shot Owens 3.067 seconds after the explosion

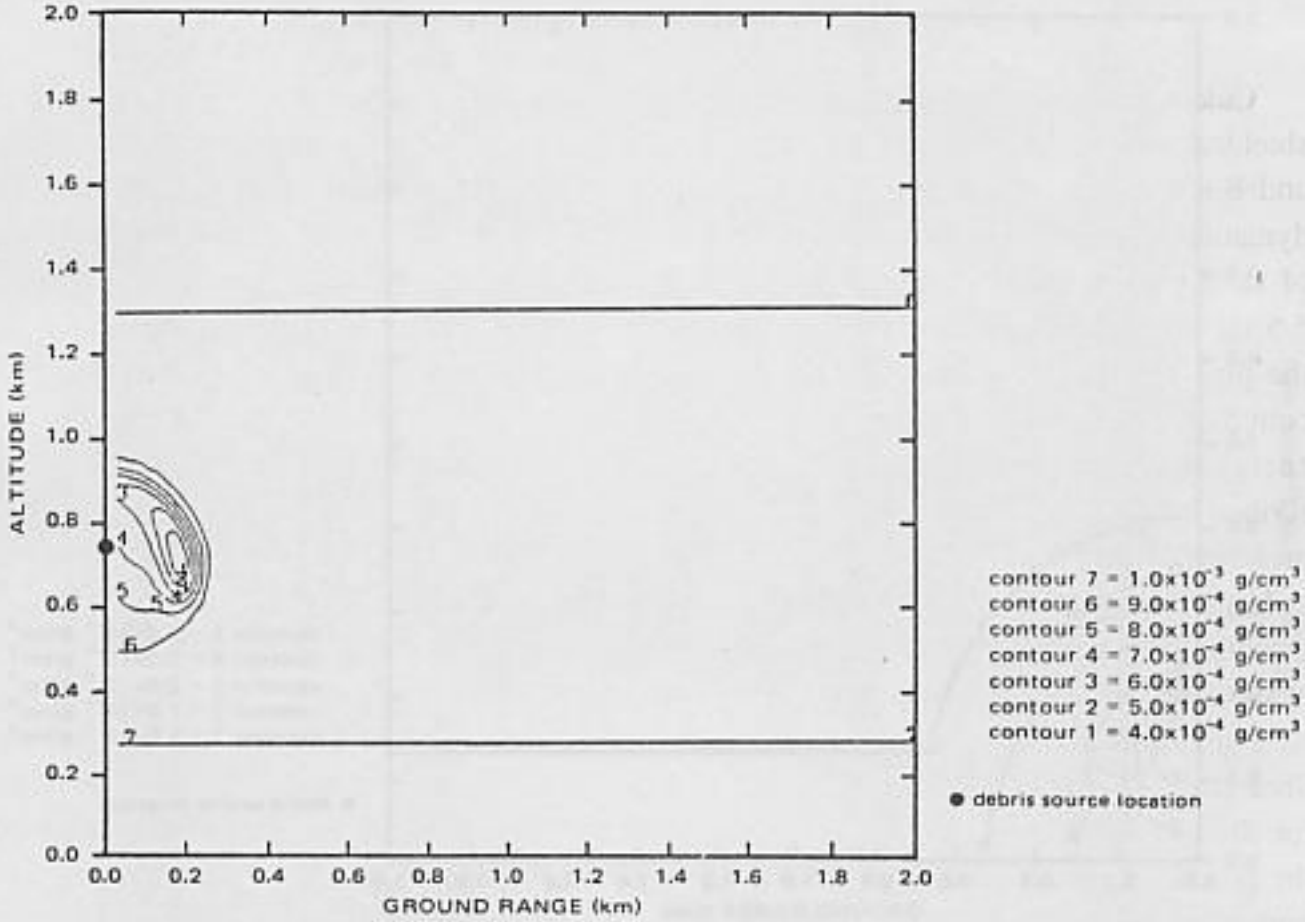

Figure 21. Iso-contours of air density at Shot Owens 9.725 seconds after the explosion

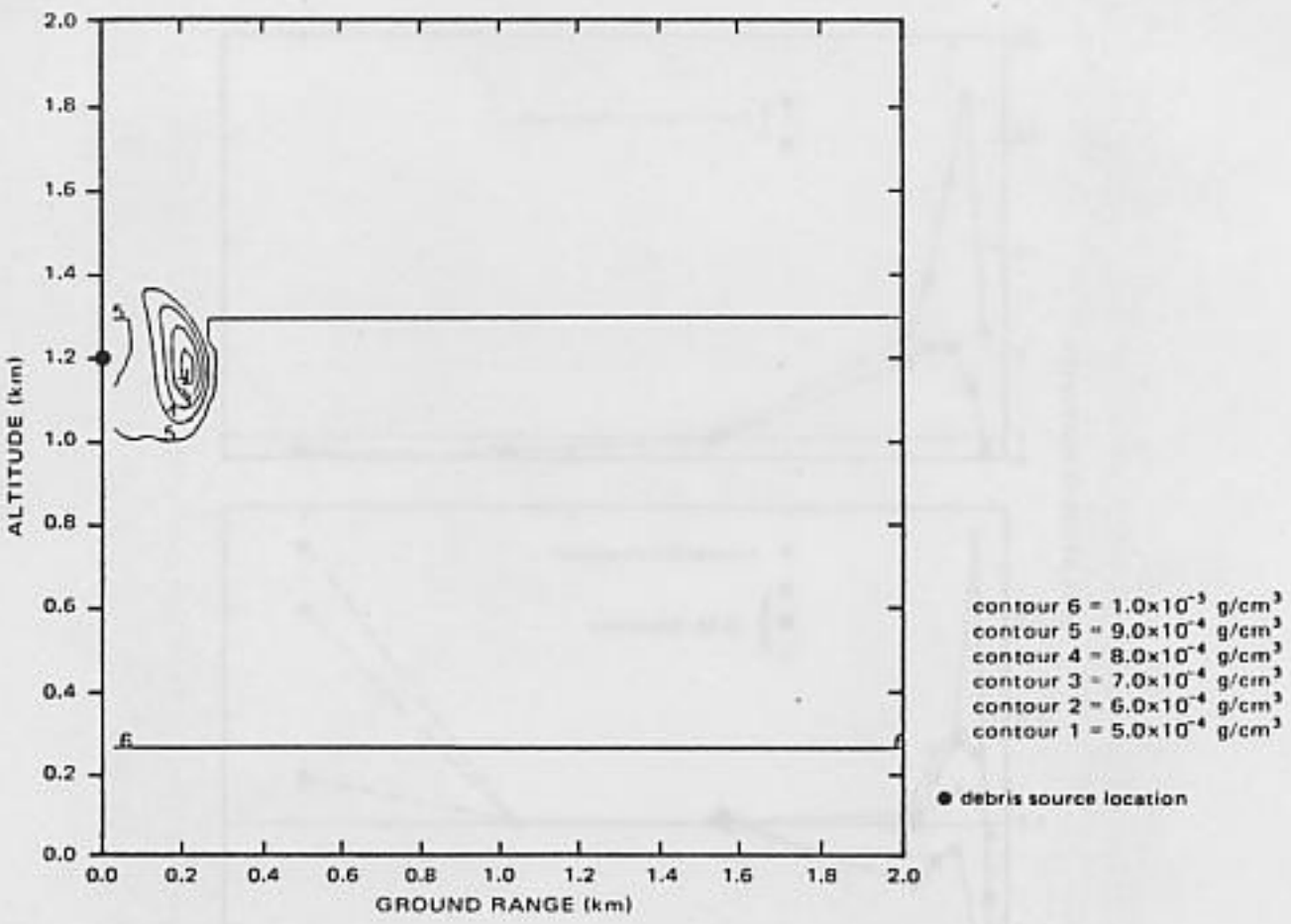

Figure 22. Iso-contours of air density at Shot Owens 20.004 seconds after the explosion

Calculations of time-varying exposure rates (roentgens per second) as measured by shielded ionization chambers (Conrad devices) were performed using the revised Fisher and Engle source values, transport methods as previously described, and STLAMB hydrodynamic modeling. The ionization chambers were located near the center of 25-inch lengths of steel pipe oriented vertically above the ground. The outside diameter of the pipe was 5.5 inches and the sides were 3/16-inch thick. Monte Carlo calculations were made using the pipe-ground geometry to obtain the adjoint leakage from the detector, which was then convoluted with the free-field fluence to obtain the fluence at the ionization chamber. The energy-dependent response per roentgen of the ionization chamber was taken to be that described by Ehrlich[21] and depicted along with those for other detector types in Figure 23. The preferential shielding of low-energy photons, along with the rapid drop of detector response at low photon energies, tends to reduce the relative effect of the many low-energy photons present in the free field as described previously. Results were obtained for the source located at the altitude of the hot spot and for the two variant positions described previously.

Figures 24 through 30 present exposure rate measurements and calculation results for Shot Hood for ground ranges from 457 to 3261 m. Figures 31 through 36 present results for Shot Owens for ground ranges from 457 to 2780 m. Results are presented in terms of the product of exposure rate and time versus time. This was done to reduce the range of numerical values for plotting. Data corresponding to the nominal, or hot spot, location are depicted using a heavy solid line. That corresponding to the low source location is depicted

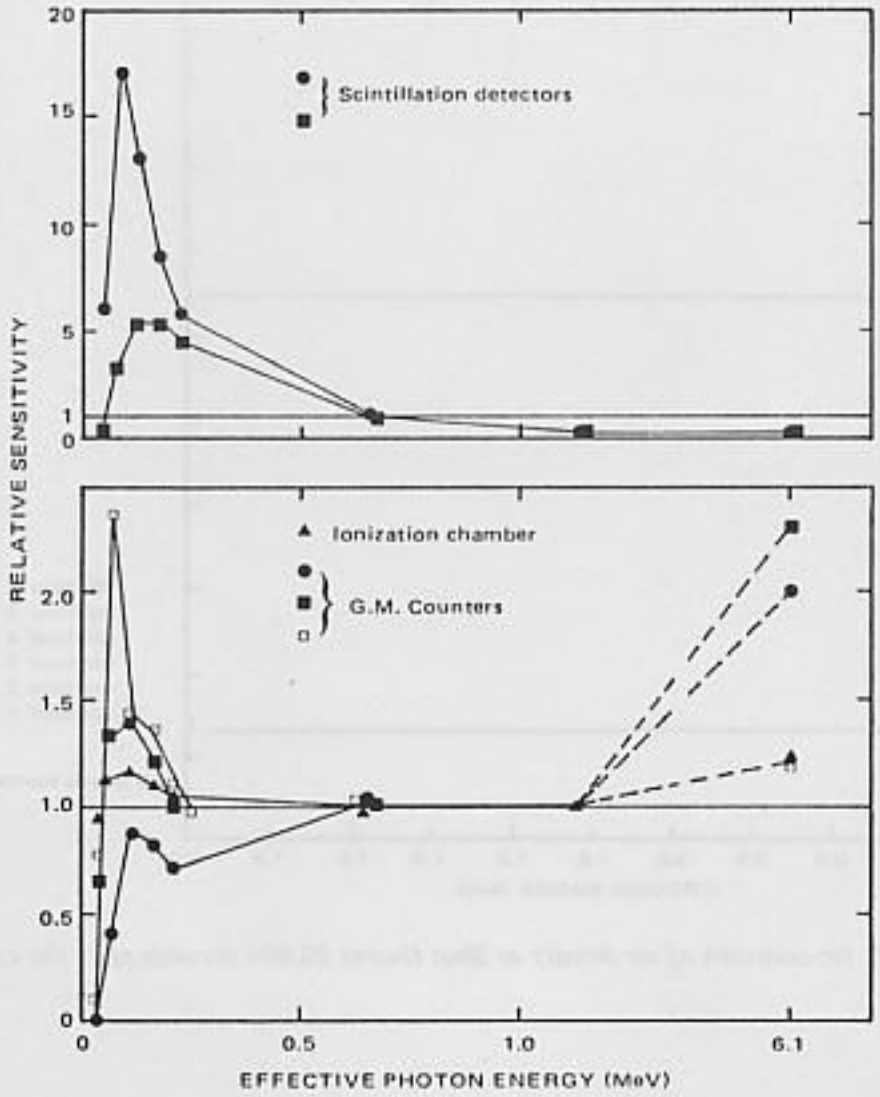

Figure 23. Highlights of energy dependence of instrument sensitivity

using the dotted line, that for the high using the dashed line. The light solid line depicts a case in which the effect of the ground reflection of the shock is removed, which will be discussed later.

The calculations follow the general shape of the measured data for times beyond a few tenths of a second. At earlier times gamma rays from air and ground capture of prompt neutrons dominate the exposure rate. They are not part of the delayed radiation model. At times between a few tenths of a second and a few seconds the calculations display the effect of the reflected shock wave passing through the fireball. The Hood measurements also show this, while the effect is hidden by the dominant secondary gamma rays for the other two shots. Beyond a few seconds the calculations are lower than the measurements, quite a bit lower in the case of Shot Hood.

Before examining the potential effect of source movement within the fireball and other factors that may affect the comparison of calculations with measurements, it is useful to examine the calculated and measured exposure rate data in time intervals that allow identification of data trends in time and space. The exposure values calculated in four intervals using the nominal (hot spot) source locations are presented as ratios to the equivalent mea-

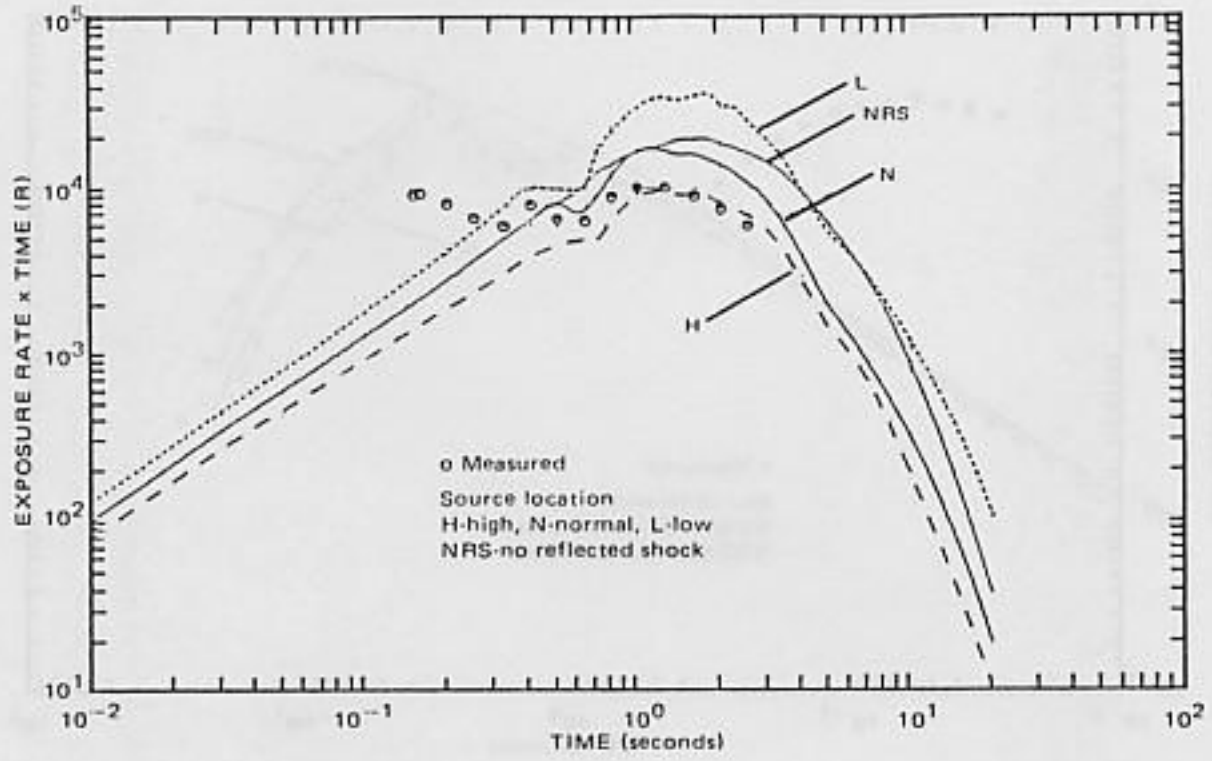

Figure 24. Measured and calculated exposure rates at Shot Hood, 457 m ground range

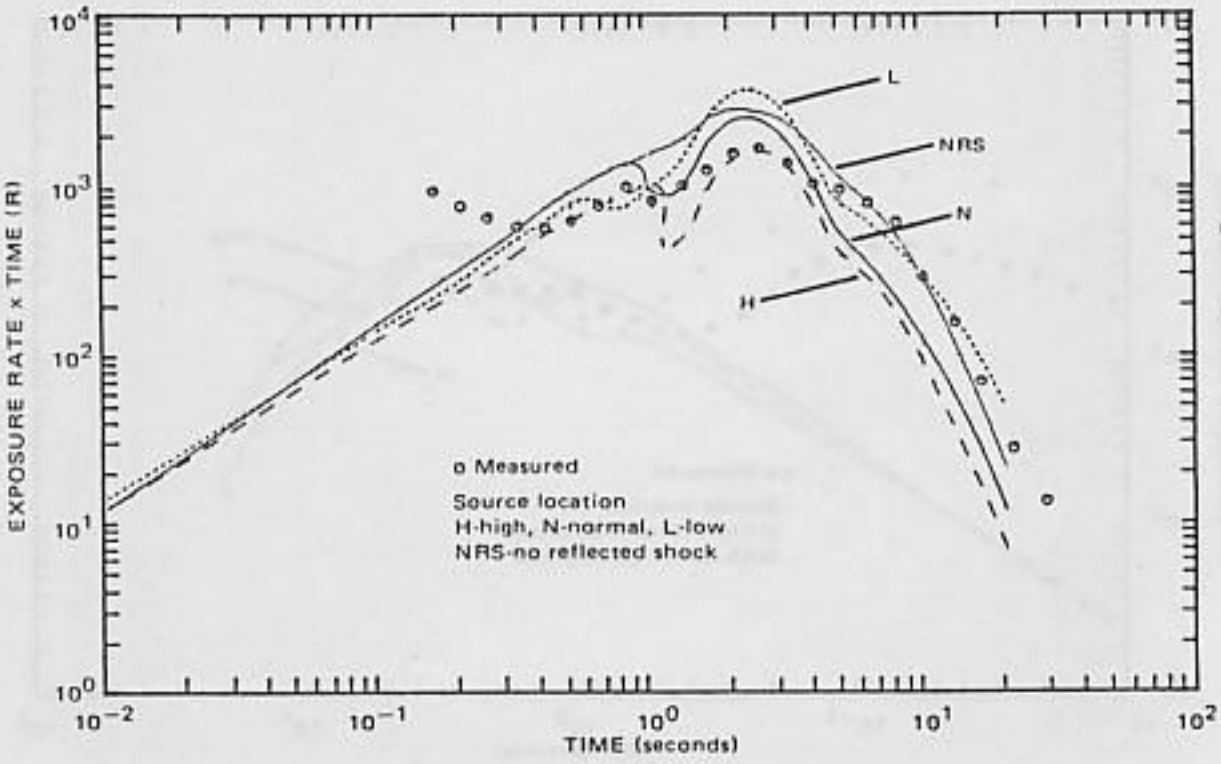

Figure 25. Measured and calculated exposure rates at Shot Hood, 914 m ground range

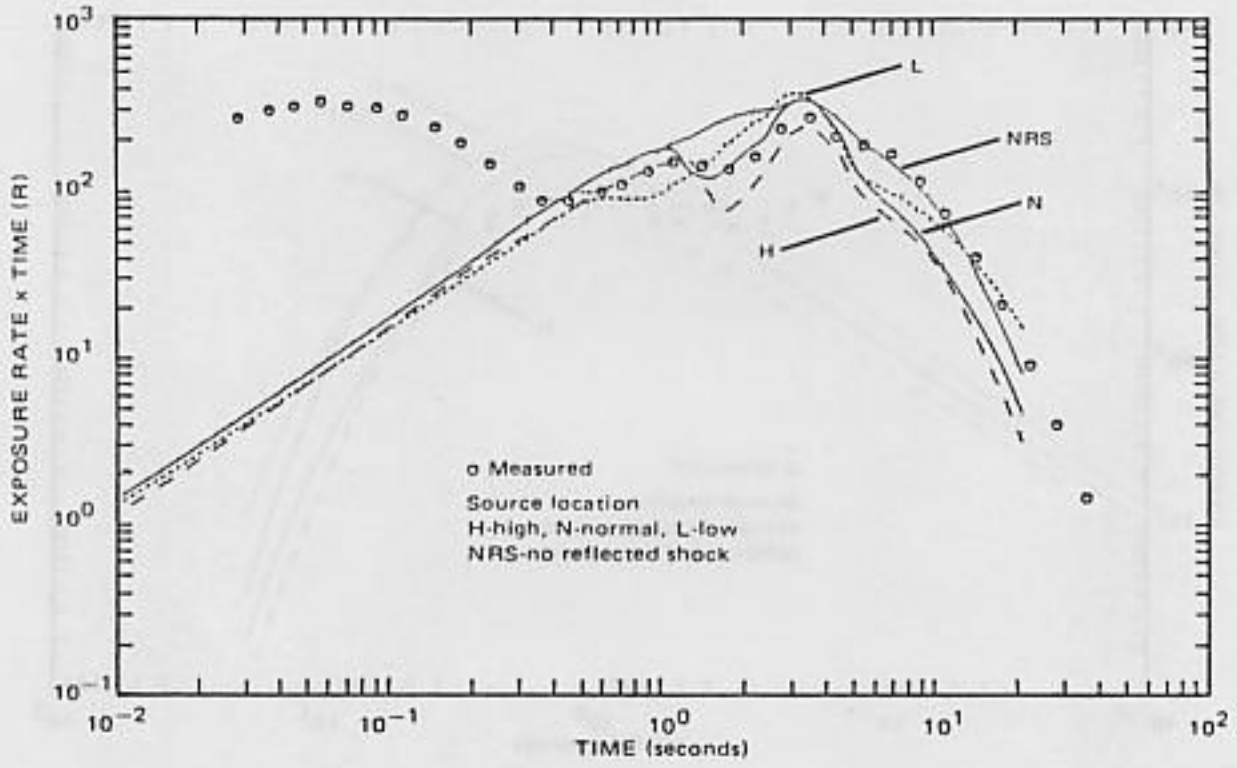

Figure 26. Measured and calculated exposure rates at Shot Hood, 1371 m ground range

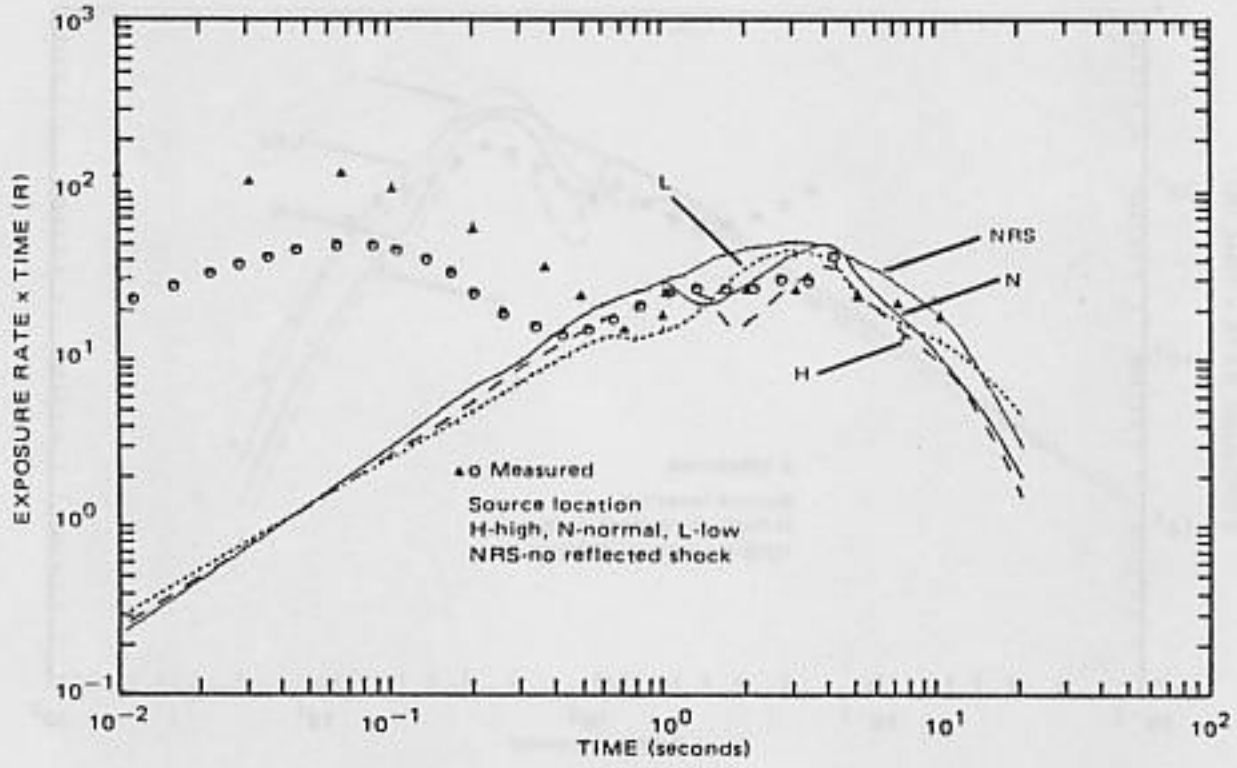

Figure 27. Measured and calculated exposure rates at Shot Hood, 1828 m ground range

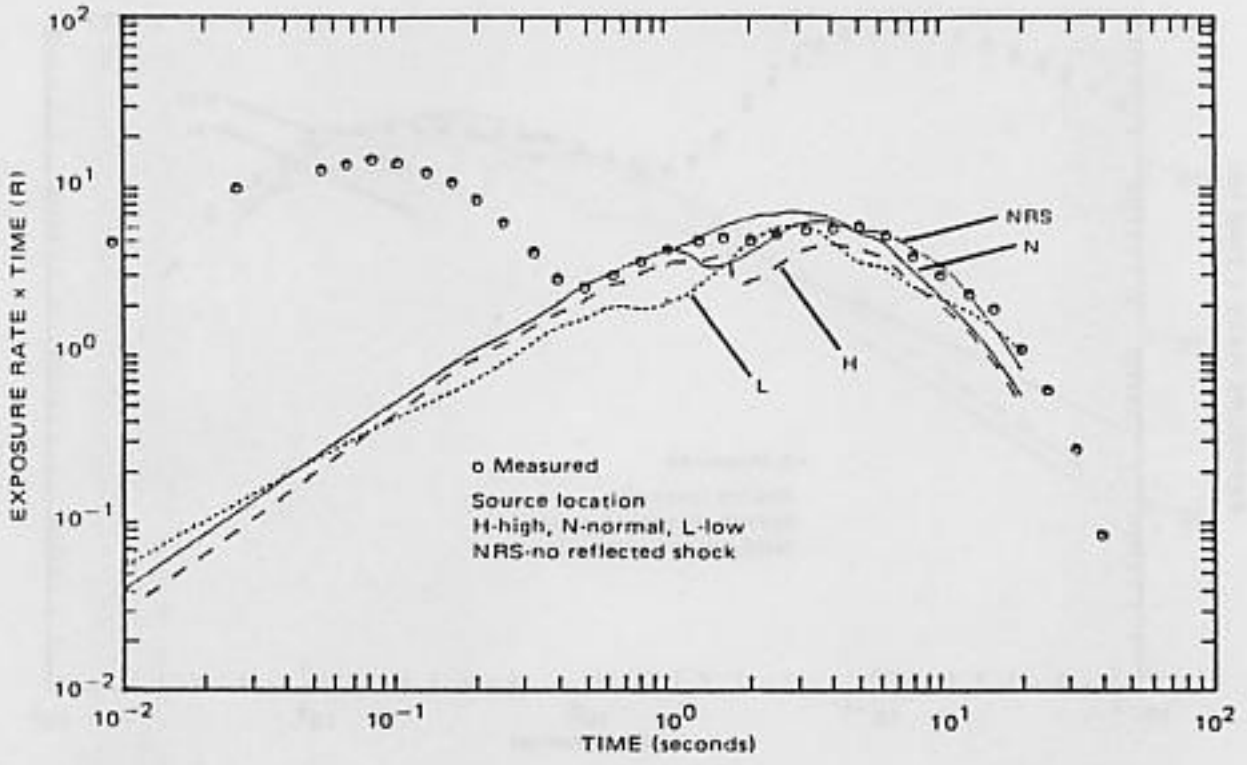

Figure 28. Measured and calculated exposure rates at Shot Hood, 2286 m ground range

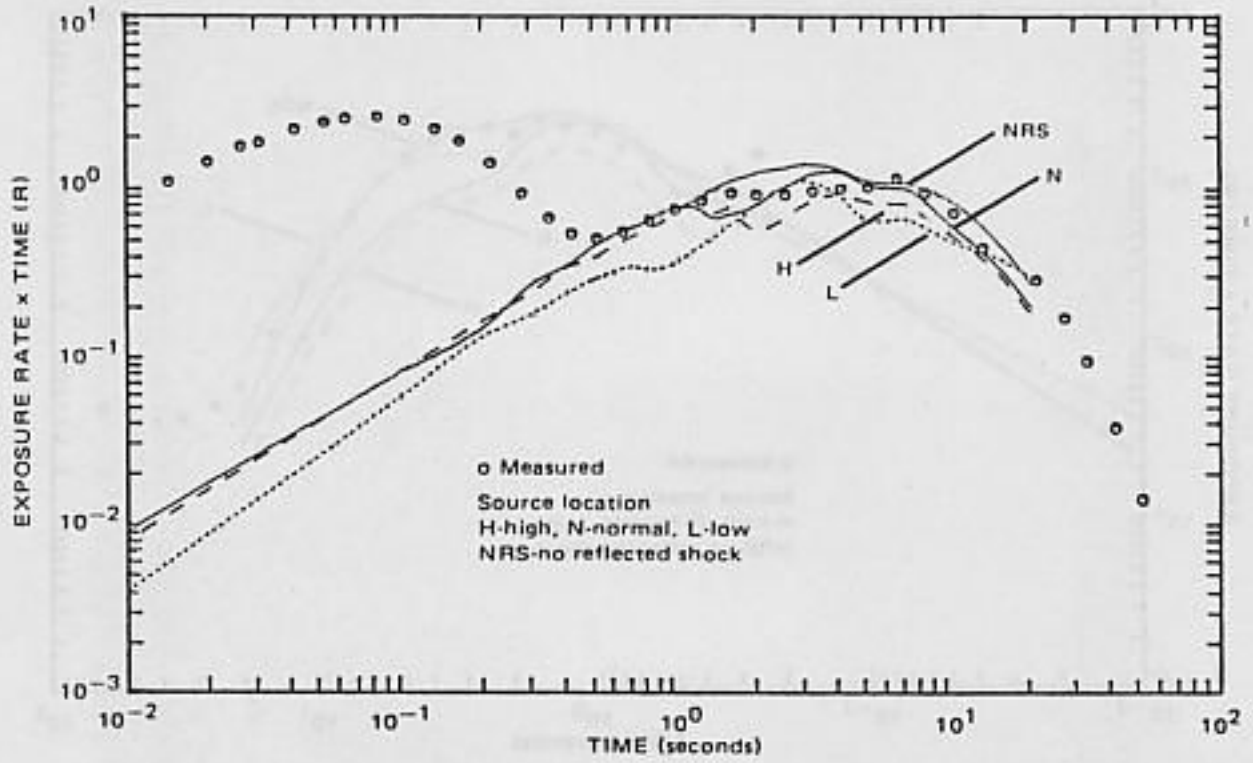

Figure 29. Measured and calculated exposure rates at Shot Hood, 2779 m ground range

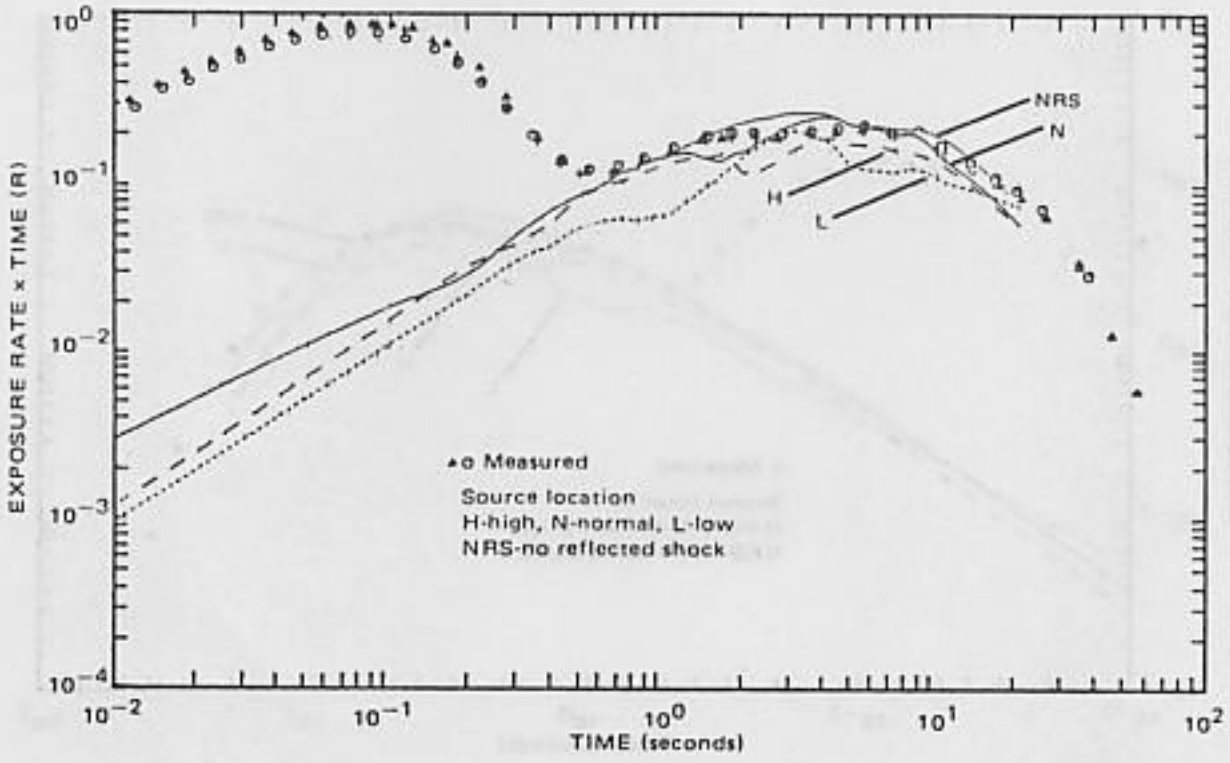

Figure 30. Measured and calculated exposure rates at Shot Hood, 3261 m ground range

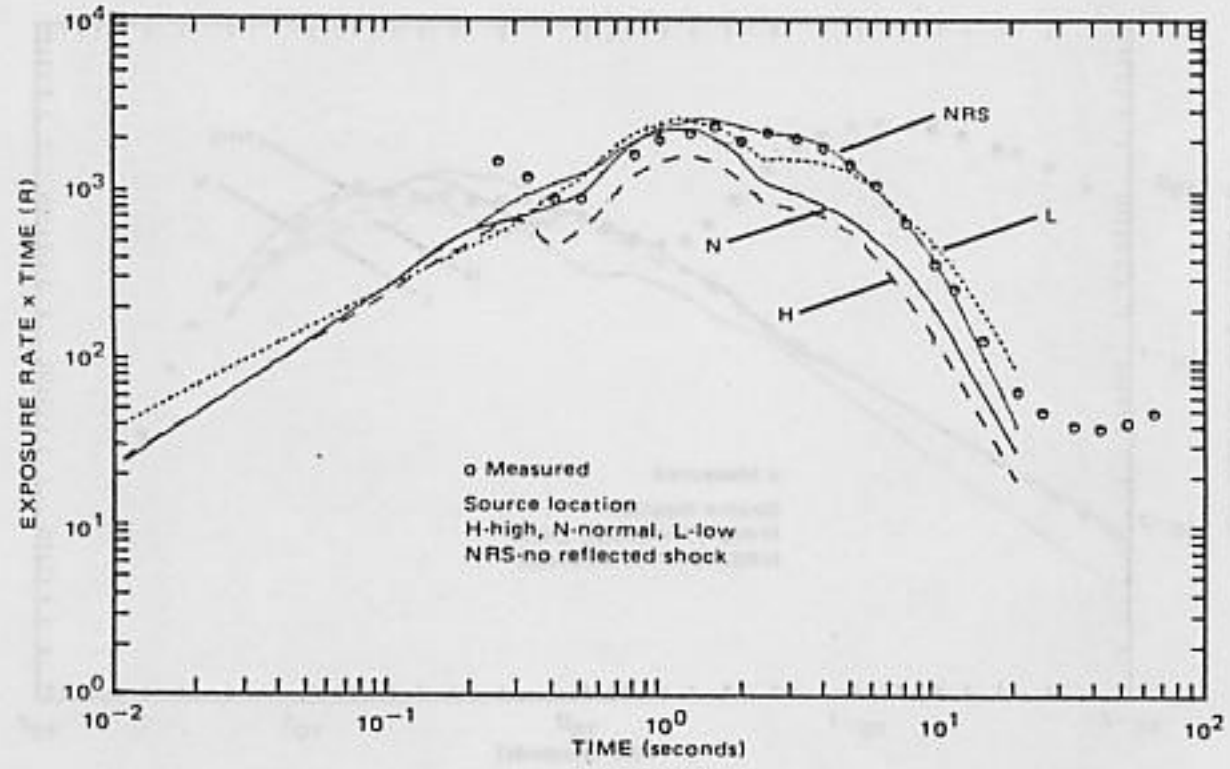

Figure 31. Measured and calculated exposure rates at Shot Owens, 457 m ground range

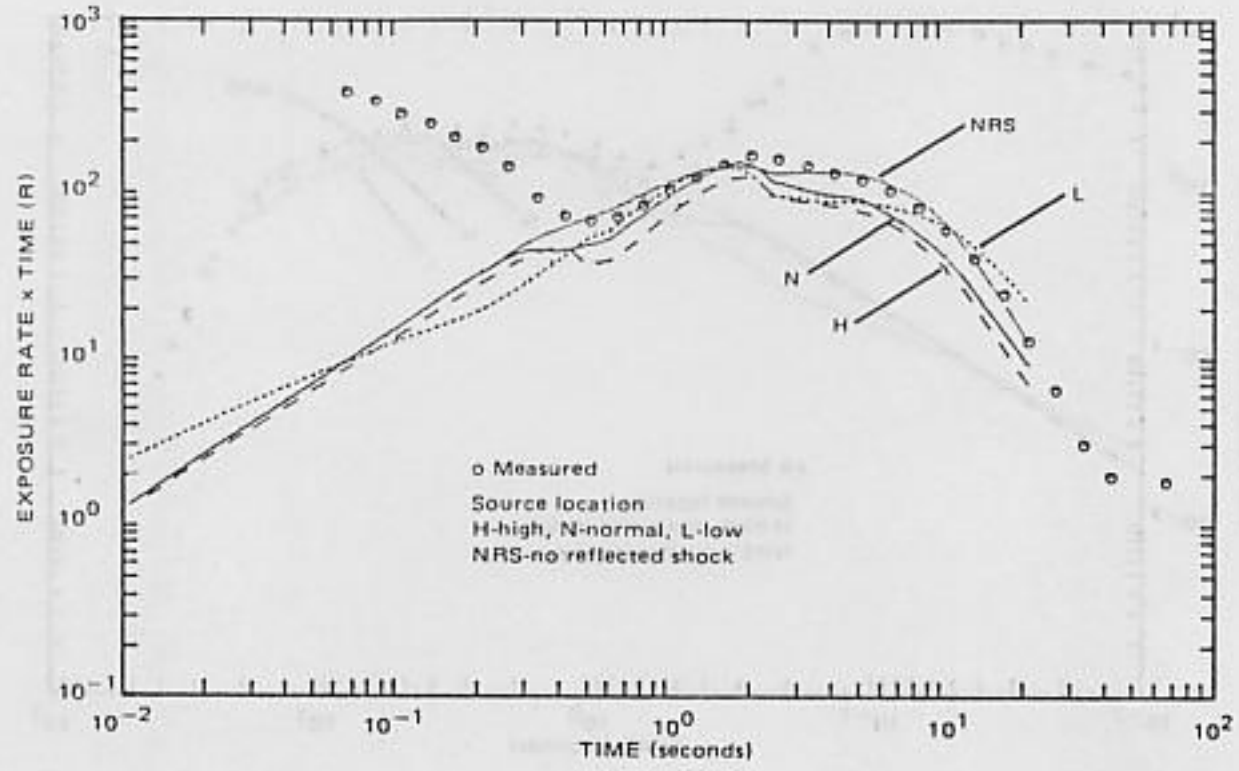

Figure 32. Measured and calculated exposure rates at Shot Owens, 914 m ground range

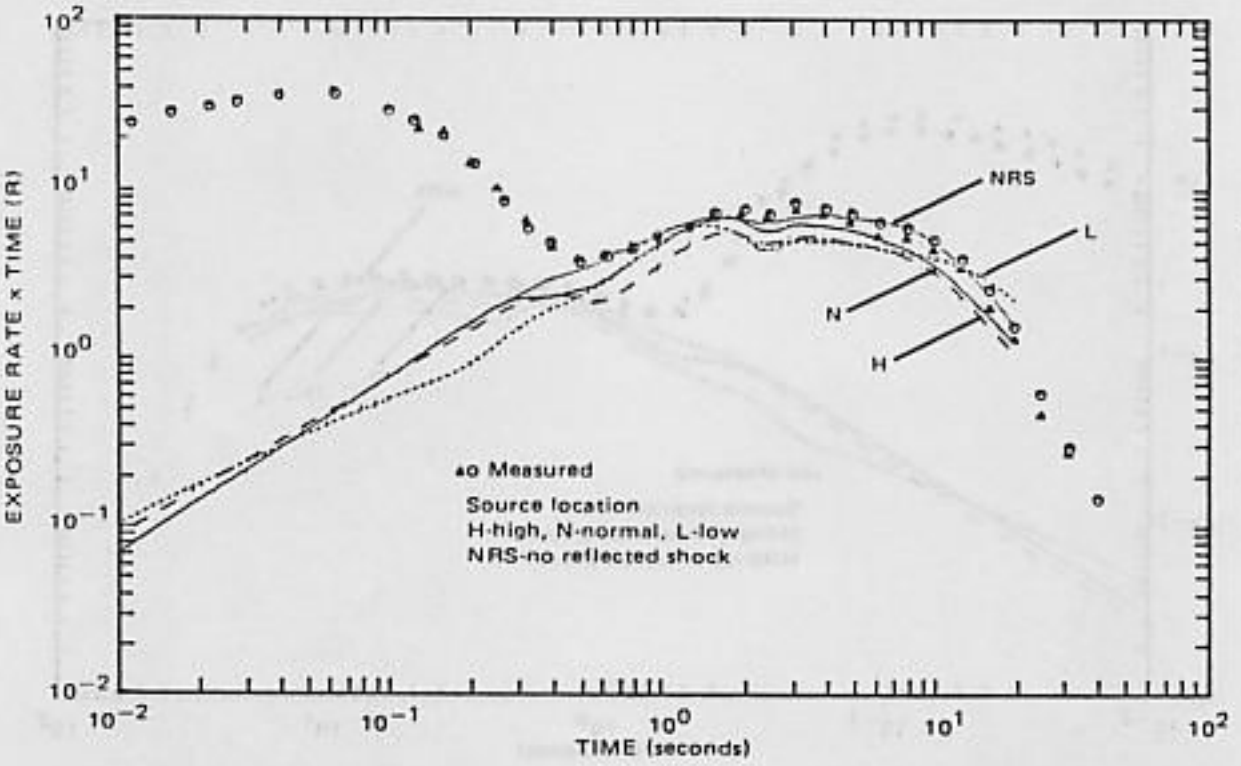

Figure 33. Measured and calculated exposure rates at Shot Owens, 1372 m ground range

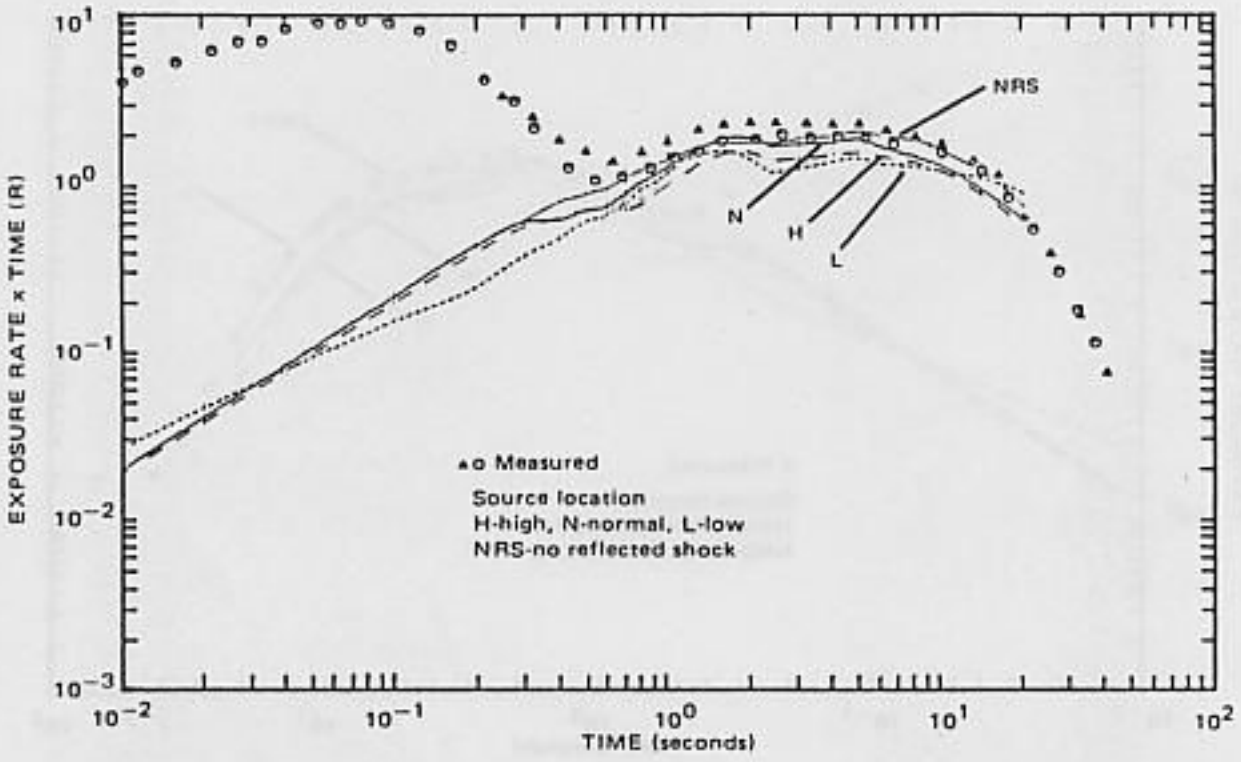

Figure 34. Measured and calculated exposure rates at Shot Owens, 1829 m ground range

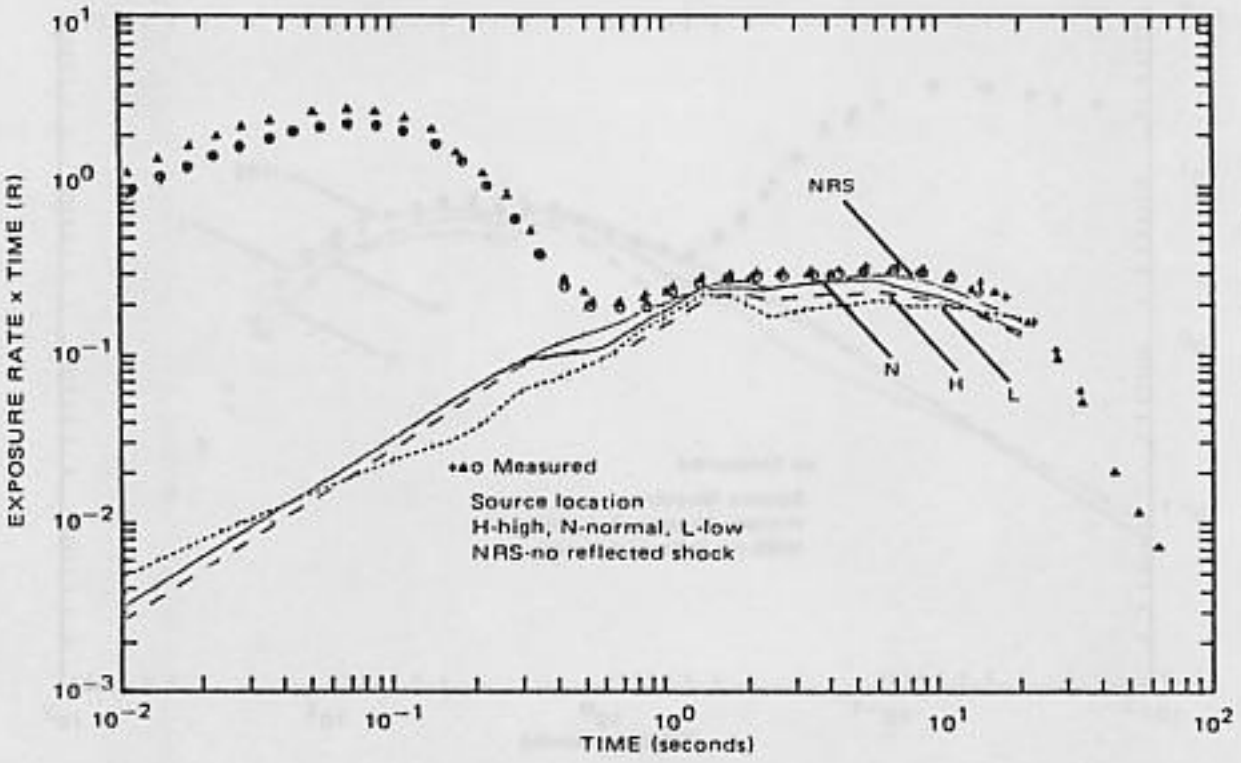

Figure 35. Measured and calculated exposure rates at Shot Owens, 2286 m ground range

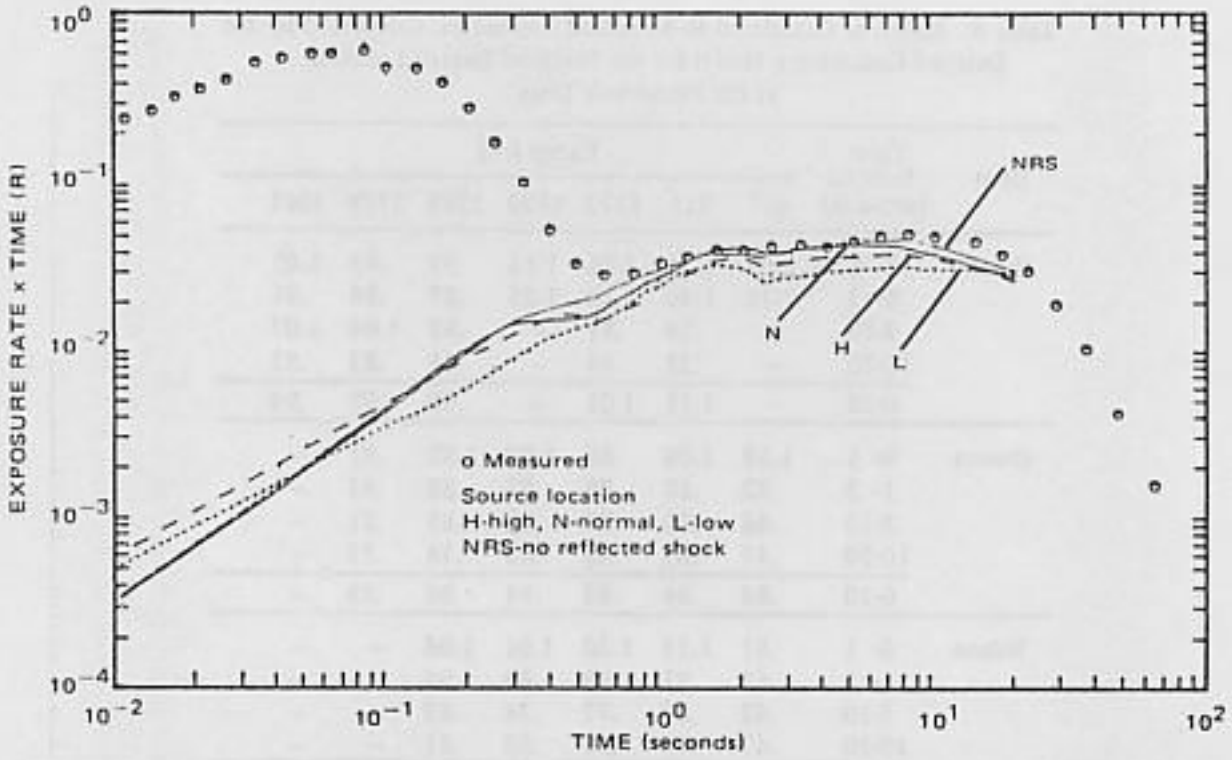

Figure 36. Measured and calculated exposure rates at Shot Owens, 2780 m ground range

sured values in Table 8. There are several types of errors to look for from the evidence in these ratios. An error in the magnitude of the source would cause a discrepancy by a uniform factor at all ranges, as would an error in calculating the size of the density well. An error in fireball rise would cause a discrepancy that is range dependent, as would an error in the source location relative to the fireball.

During the earliest period the calculation-measurement ratios for Shot Hood exhibit a range dependence. Either a faster fireball rise or a rise of the debris within the fireball would reduce the discrepancy. However, photographic evidence[22] indicates that for Upshot-Knothole Climax, a shot similar to Hood, the debris remained in the fireball center through approximately one second. This leaves the fireball rise as suspect, particularly for large yields, a suspicion that is supported by the same photographic evidence. During the period from one to three seconds, the calculation-measurement ratios for Shot Hood still exhibit a discrepancy at close range though to a lesser extent than during the prior periods. The higher fireball caused by an increased rise rate during the period to one second would probably account for most of the discrepancy. In addition, photographic evidence suggests that the source is rising relative to the center of the Hood fireball.

In the case of Shots Owens and Wilson, the calculation-measurement ratios during the first two periods show good agreement, the mean ratio for the first period being 1.02 ± 0.12 and that for the second being 0.88 ± 0.10, where the means are based on the ratios for both shots and the uncertainty is the standard error of the distribution.

During the periods beyond three seconds, the calculation-measurement ratios for all three shots exhibit systematic variations with distance, being low close in and high far-out. According to Figures 24 to 36, these discrepancies could be eliminated by removing the provision for ground-shock reflection from the model. The results of such a modification

Table 8. Ratios of Calculated to Measured Exposures, Calculated by the Delayed Gamma-ray Model for the Nominal Source Location at the Plumbbob Tests

Shot	Time Interval (seconds)	Range (m)						
		457	915	1372	1829	2286	2779	3261
Hood	0- 1	1.08	1.34	1.26	1.16	.97	.93	1.05
	1- 3	1.76	1.40	1.12	1.05	.87	.94	.91
	3-10	–	.74	.81	–	.95	1.04	1.07
	10-20	–	.38	.44	–	.61	.83	.83
	0-20	–	1.18	1.01	–	.90	.95	.99
Owens	0- 1	1.18	1.06	.89	1.00	1.02	.91	–
	1- 3	.82	.88	.88	.97	.88	.95	–
	3-10	.46	.72	.77	.91	.85	.91	–
	10-20	.47	.63	.68	.83	.74	.73	–
	0-20	.84	.86	.83	.94	.88	.89	–
Wilson	0- 1	.81	1.11	1.20	1.01	1.06	–	–
	1- 3	.62	.91	.99	.88	.94	–	–
	3-10	.42	.63	.77	.74	.83	–	–
	10-20	.47	.40	.50	.58	.61	–	–
	0-20	.65	.82	.88	.81	.86	–	–

are depicted as a light solid line in the figures. However, the early time structure observed in the measurements is no longer observed in the calculations after eliminating the reflected shock. Also, the resulting fireball rise rate is unrealistically slow, as compared to the rate from test shot photographs. Thus, this model variant must be viewed as an extreme case, of academic interest only, but one that points toward late-time hydrodynamic or source-location problems.

The comparison between calculated and measured exposures in the 3 to 20 second time periods can be improved by lowering the source relative to the fireball center. Photographic evidence suggests that such a phenomenon does occur after the debris rises to the top of the fireball, which takes place at approximately three seconds. Table 9 provides an estimate of the effect of lowering the source (but not the fireball). The data are based on those presented in Figures 24 to 36. In the table, H stands for high source, N for nominal, and L for low. Intermediate locations are given as NH and NL and are simple averages, representing a midpoint between the two cases for which calculations were made. Note that raising the source for Shot Hood between one and three seconds reduces, but does not eliminate, the discrepancy, indicating that a change in cloud location is probably necessary also.

Lowering the sources at late times improves the agreement between measurement and calculation, but, just as importantly, it reverses how the discrepancy varies with range. The remaining discrepancy can be accounted for to a large extent on the basis of the radial displacement of the source as it moves down the outside of the fireball and eventually becomes incorporated in the torus.

At times between 5 and 10 seconds, the outer surface of the rising fireball begins to cool; the vapors are subject to drag from the surrounding atmosphere. The resulting downward flow around the outside of the fireball is matched by an upward flow at its center. This flow

Table 9. Ratios of Calculated to Measured Exposures, Calculated by the Delayed Gamma-ray Model for the Moving Source Location at the Plumbbob Tests

Shot	Time Interval (seconds)	Source Location	Range (m)						
			457	914	1372	1289	2286	2779	3261
Hood	0- 1	N	1.08	1.34	1.26	1.16	0.97	0.93	1.05
	1- 3	NH	1.40	1.13	0.95	0.93	0.78	0.84	0.84
	3-10	NL	–	0.95	0.84	–	0.85	0.89	0.89
	10-20	L	–	1.10	0.90	–	0.76	0.85	0.75
	0-20		–	1.15	0.99	–	0.85	0.88	0.90
Owens	0- 1	N	1.18	1.06	0.89	1.00	1.02	0.91	–
	1- 3	N	0.82	0.88	0.88	0.97	0.88	0.95	–
	3-10	NL	0.67	0.74	0.72	0.82	0.75	0.79	–
	10-20	L	1.30	1.18	0.95	0.95	0.75	0.68	–
	0-20		0.91	0.90	0.84	0.92	0.84	0.84	–
Wilson	0- 1	N	0.81	1.11	1.20	1.01	1.06	–	–
	1- 3	N	0.62	0.91	0.99	0.88	0.94	–	–
	3-10	NL	0.62	0.65	0.72	0.67	0.73	–	–
	10-20	L	1.31	0.76	0.71	0.67	0.63	–	–
	0-20		0.70	0.85	0.89	0.80	0.83	–	–

pattern produces a torus, within which resides the debris. The radius of the torus depends on yield. Thus, the torus for Shot Hood attains a radius of approximately 325 m by 10 seconds, while those for Owens and Wilson are approximately 200 m. The flow about the torus causes rapid mixing, cooling, and return to near ambient density. Under such conditions the radial displacement of the debris causes an increase in exposure that increases with range. In the case of Shot Hood that increase, in terms of multiplicative factors, was estimated using simple point-kernel techniques, as follows:

Correction Factor for Radial Displacement for Shot Hood

Period (second)	Range (m)				
	914	1372	2286	2779	3261
3-10	1.04	1.07	1.15	1.19	1.23
10-20	1.13	1.17	1.25	1.30	1.35

These factors were applied to the calculation-measurement ratio for Hood as adjusted for source height; the results are given in Table 10. The data in Table 10 represent a definite improvement over the original calculation-measurement ratios found in Table 8.

In summary, comparisons of results of the model used to produce the delayed gamma-ray component of DS86 with results of gamma-ray exposure rate measurements made in the Plumbbob tests indicate that the model has shortcomings that are mainly due to incorrect hydrodynamic data or inadequate modeling detail based on existing data. The effect of previously mentioned transport and source uncertainties do not play a part in reaching this

Table 10. Ratios of Calculated to Measured Exposures, Calculated by the Delayed Gamma-ray Model for Shot Hood and the Moving Source with Adjustment for Torus Formation

Time Interval (seconds)	Source Location	Range (m)						
		457	914	1372	1829	2286	2779	3261
0- 1	N	1.08	1.34	1.26	1.16	0.97	0.93	1.05
1- 3	NH	1.40	1.13	0.95	0.93	0.78	0.84	0.84
3-10	NL	–	0.99	0.90	–	0.98	1.06	1.09
10-20	L	–	1.24	1.05	–	0.95	1.11	1.01
0-20		–	1.16	1.02	–	0.91	0.97	1.00

conclusion because the detector is shielded from the overestimated low-energy photons and there are sufficient numbers of fissions produced by 14 MeV neutrons in the tests to offset the extra gamma rays produced by fast fission. (14 MeV fission produces substantially less energy per fission as fission product gamma rays than does fast or thermal fission.[8] The implications of this conclusion for DS86 are described later in this report.

Other Model Comparisons with Weapon Tests

There are other comparisons that can be made with data from weapon tests in addition to those from Hood, Owens, and Wilson. However, most involve total exposure rather than exposure rate.

Two such tests are Ranger Shot Fox and Buster Shot Dog. Ranger-Fox was a device of 22 kt yield, air dropped and exploded at a height of 437 m. Buster-Dog was a device of 21 kt yield, air dropped and exploded at a height of 432 m. Both devices were similar to the Nagasaki bomb in design and high explosive thickness.

Calculated and measured[23,24] gamma-ray exposures are provided for Fox in Figures 37 and 38 and for Dog in Figures 39 and 40. Each shot had two orthogonal lines of film dosimeters, one running west from the intended ground zero and one running south. The measured values have been revised as recommended by Storm.[25] The revisions include corrections for betatron calibration energy (measured values were multiplied by 0.885) and for energy-dependence of the film sensitivity (for the sensitive films, exposures less than 10 R, the measured values were multiplied by 0.909; for the insensitive films, at exposures more than 10 R, they were multiplied by 0.840).

The calculated exposure values are generally 10 to 20% below the revised measured values. However, agreement is somewhat better in the first 2000 m than at greater ranges. Taking the source location into account is likely to improve the agreement, particularly at long ranges. However, for shorter ranges the effect is likely to be minimal given the high burst height.

Predicting Delayed Gamma-ray Exposure at Hiroshima and Nagasaki

The hydrodynamic behavior of the Hiroshima (15 kt) and Nagasaki (21 kt) explosions are depicted in Figures 41 to 46 and 47 to 52, respectively. These were computed using the STLAMB code. Because of the low yield and high burst heights, all events previously described for the Plumbbob Shot occur at much later times. At one second, the shockwave

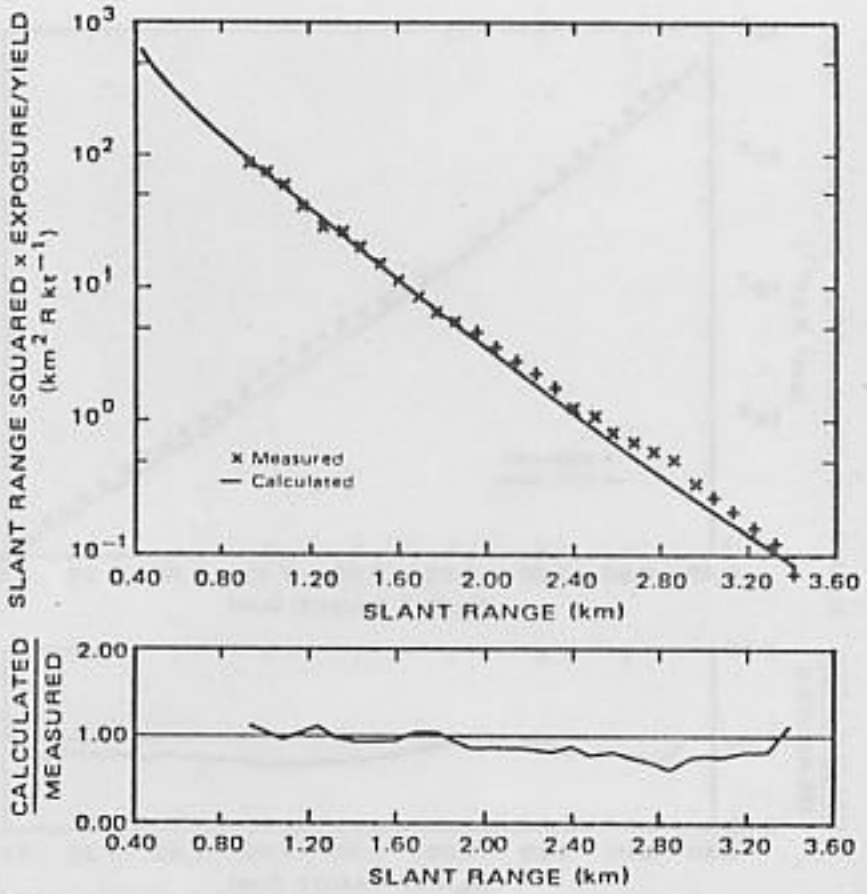

Figure 37. Total gamma-ray exposure per kiloton along the west sample line at Shot Ranger-Fox

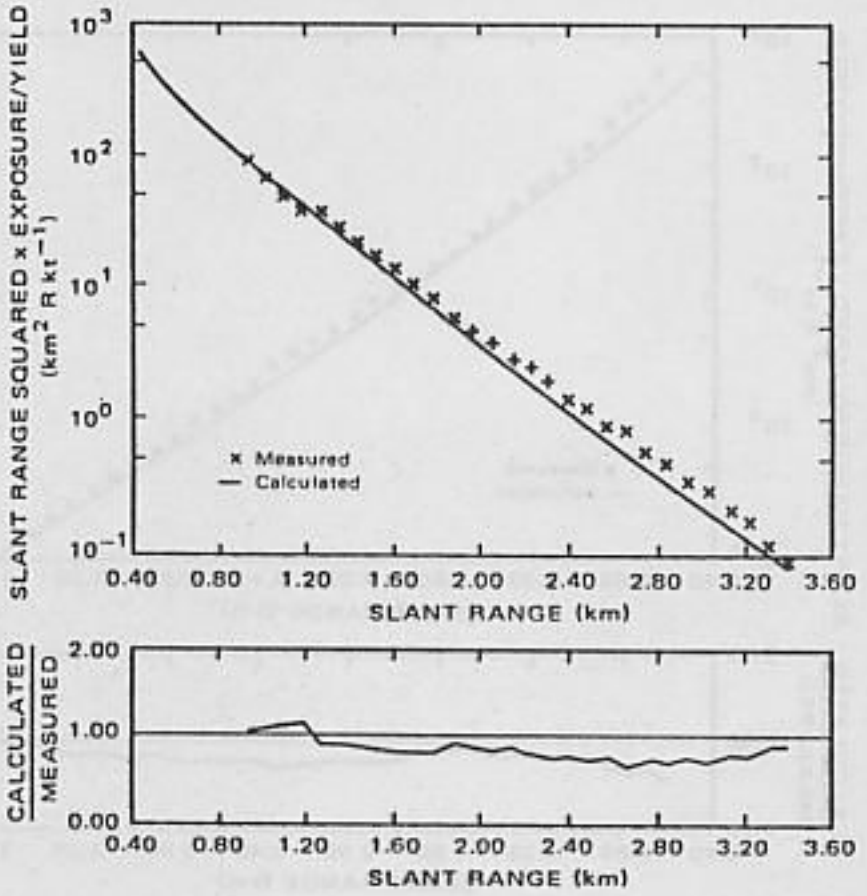

Figure 38. Total gamma-ray exposure per kiloton along the south sample line at Shot Ranger-Fox

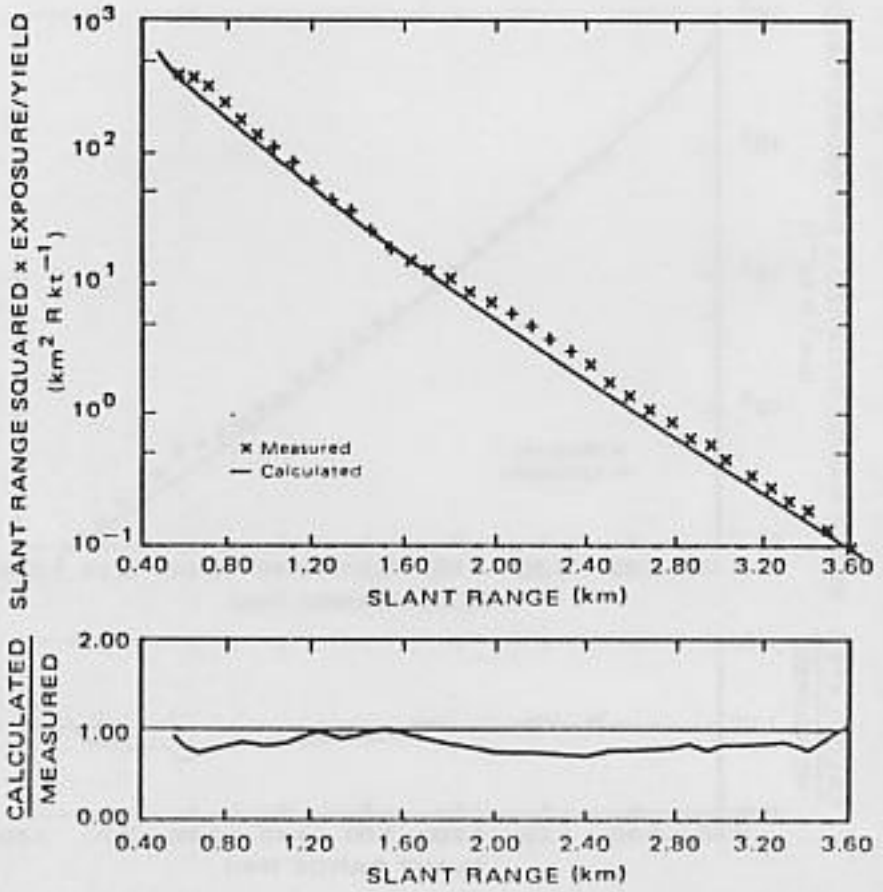

Figure 39. Total gamma-ray exposure per kiloton along the west sample line at Shot Buster-Jangle Dog

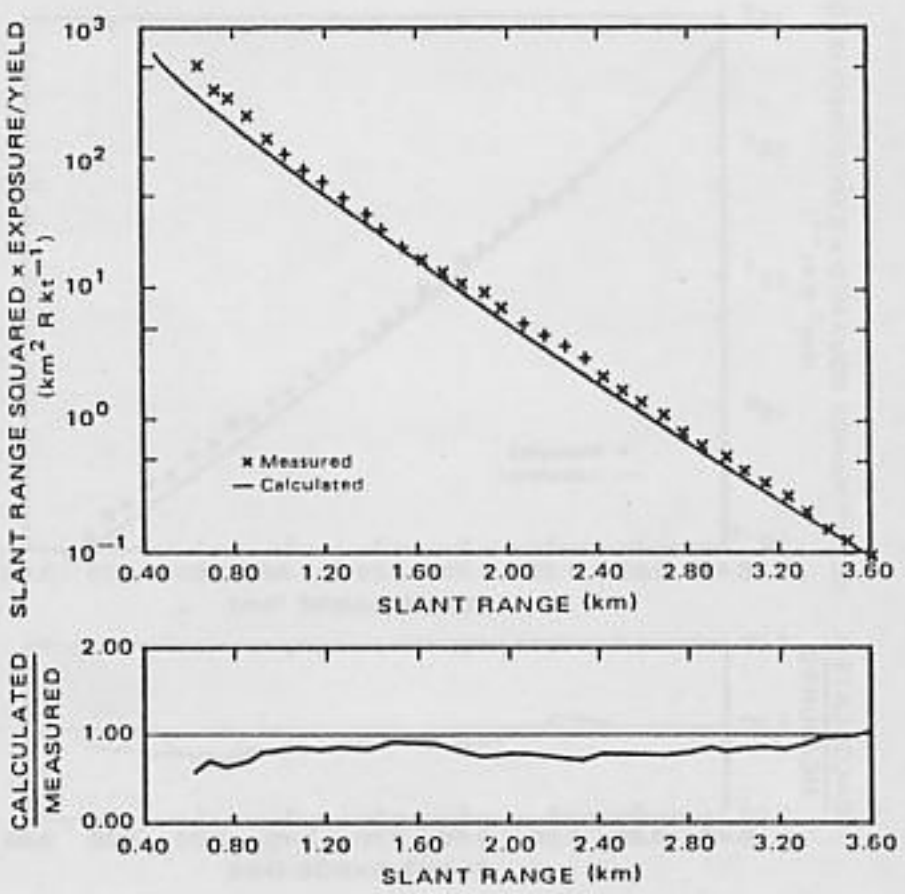

Figure 40. Total gamma-ray exposure per kiloton along the south sample line at Shot Buster-Jangle Dog

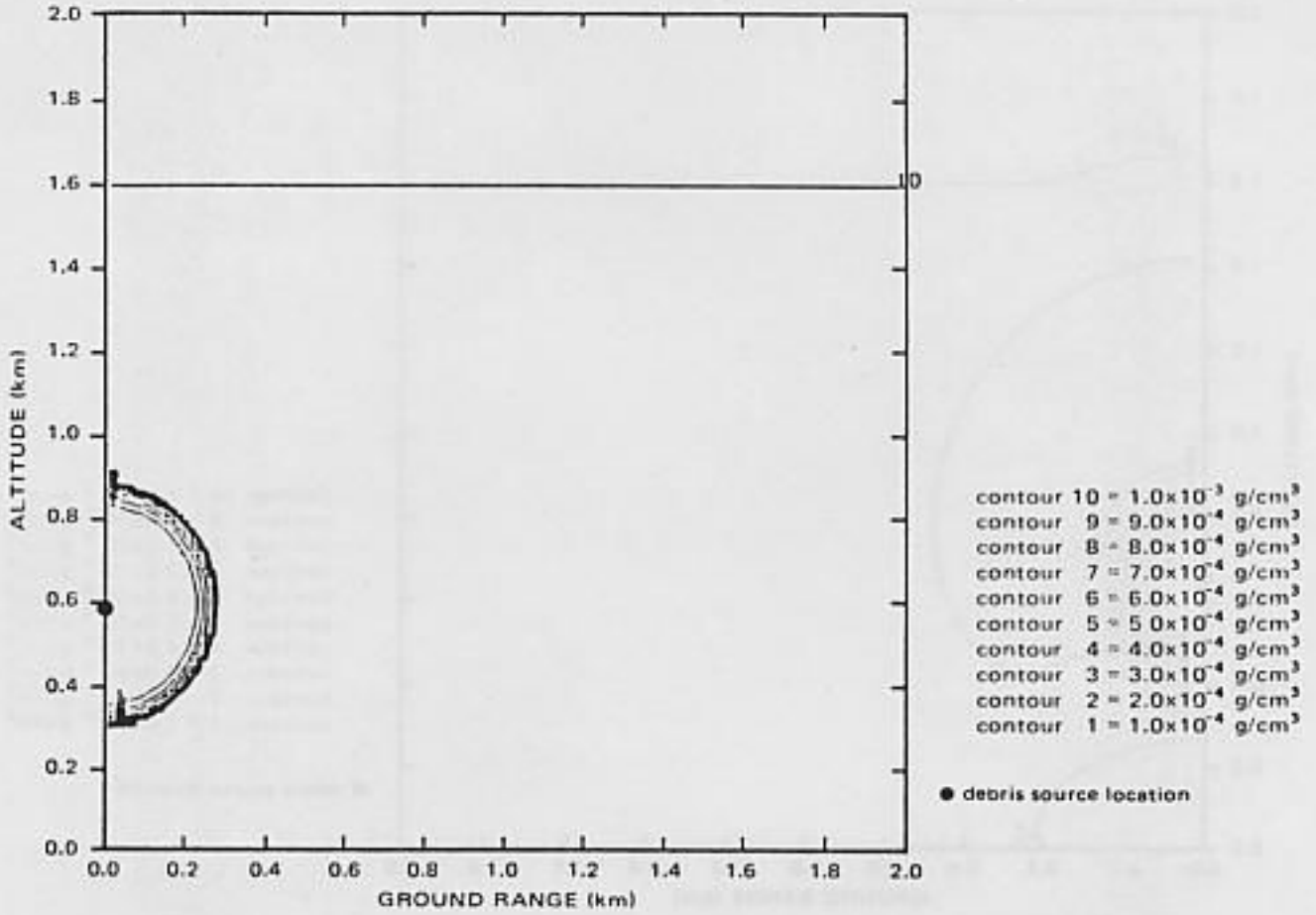

Figure 41. Iso-contours of air density at Hiroshima 0.354 seconds after the explosion

Figure 42. Iso-contours of air density at Hiroshima 1.034 seconds after the explosion

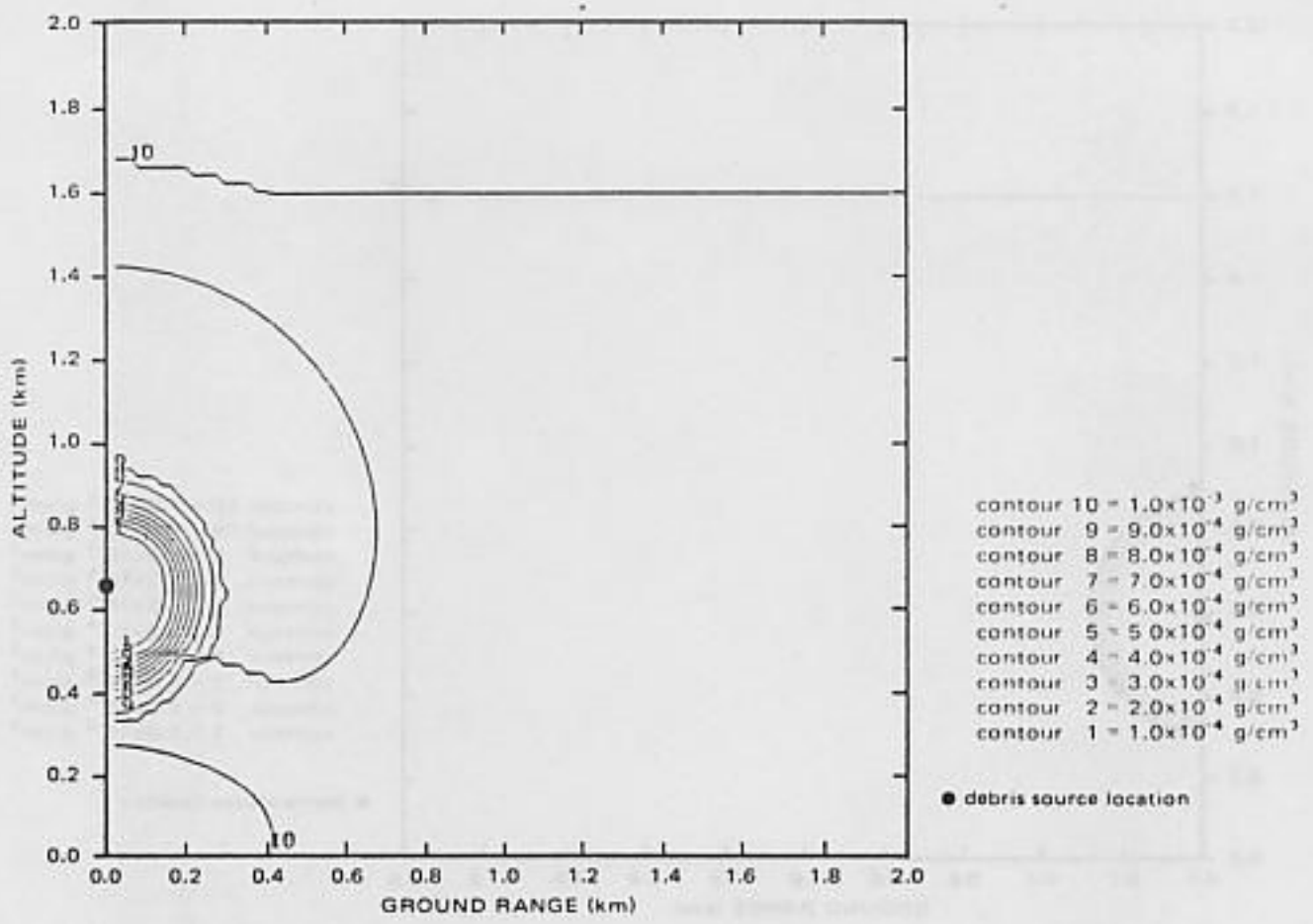

Figure 43. Iso-contours of air density at Hiroshima 2.028 seconds after the explosion

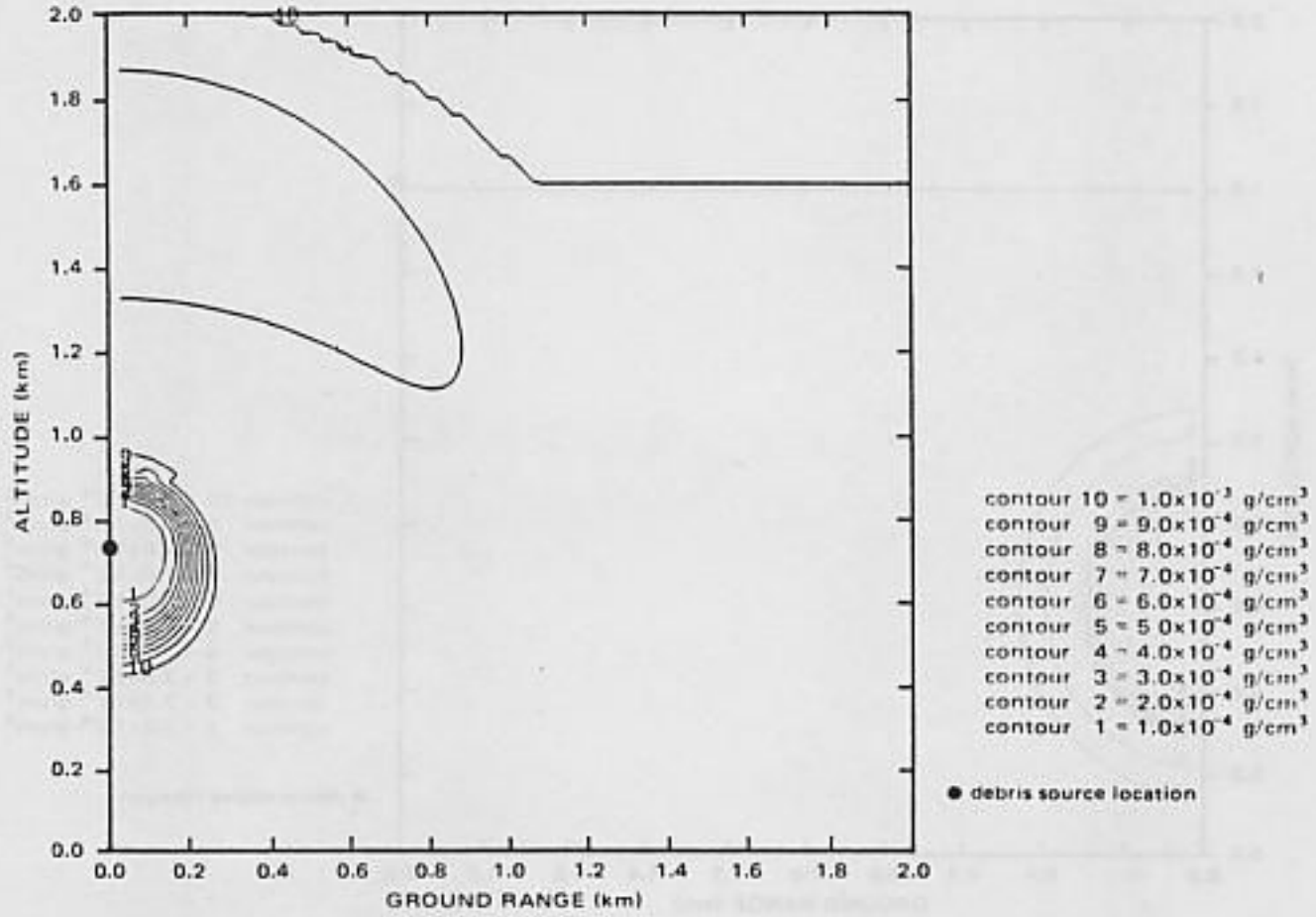

Figure 44. Iso-contours of air density at Hiroshima 3.067 seconds after the explosion

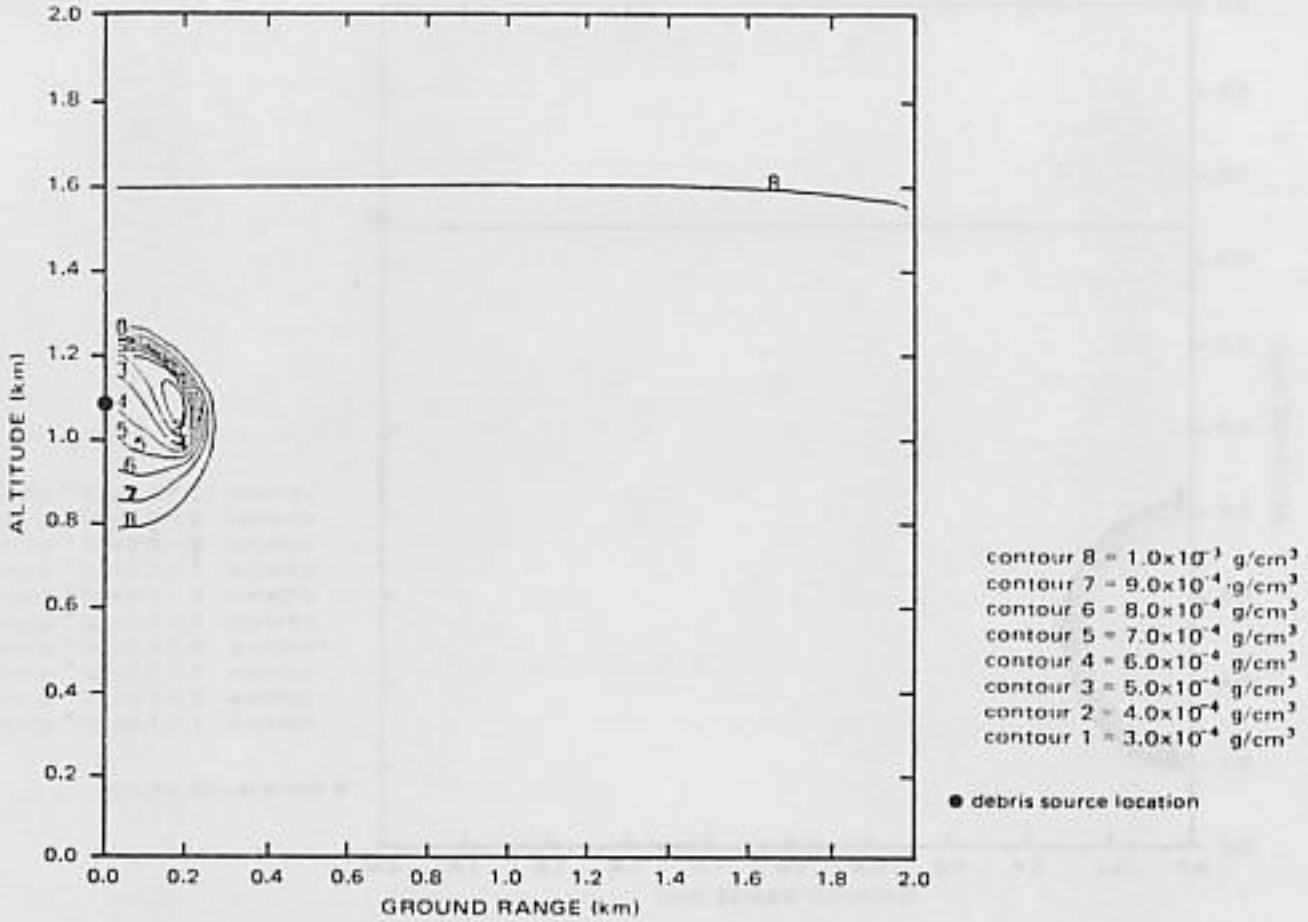

Figure 45. Iso-contours of air density at Hiroshima 9.725 seconds after the explosion

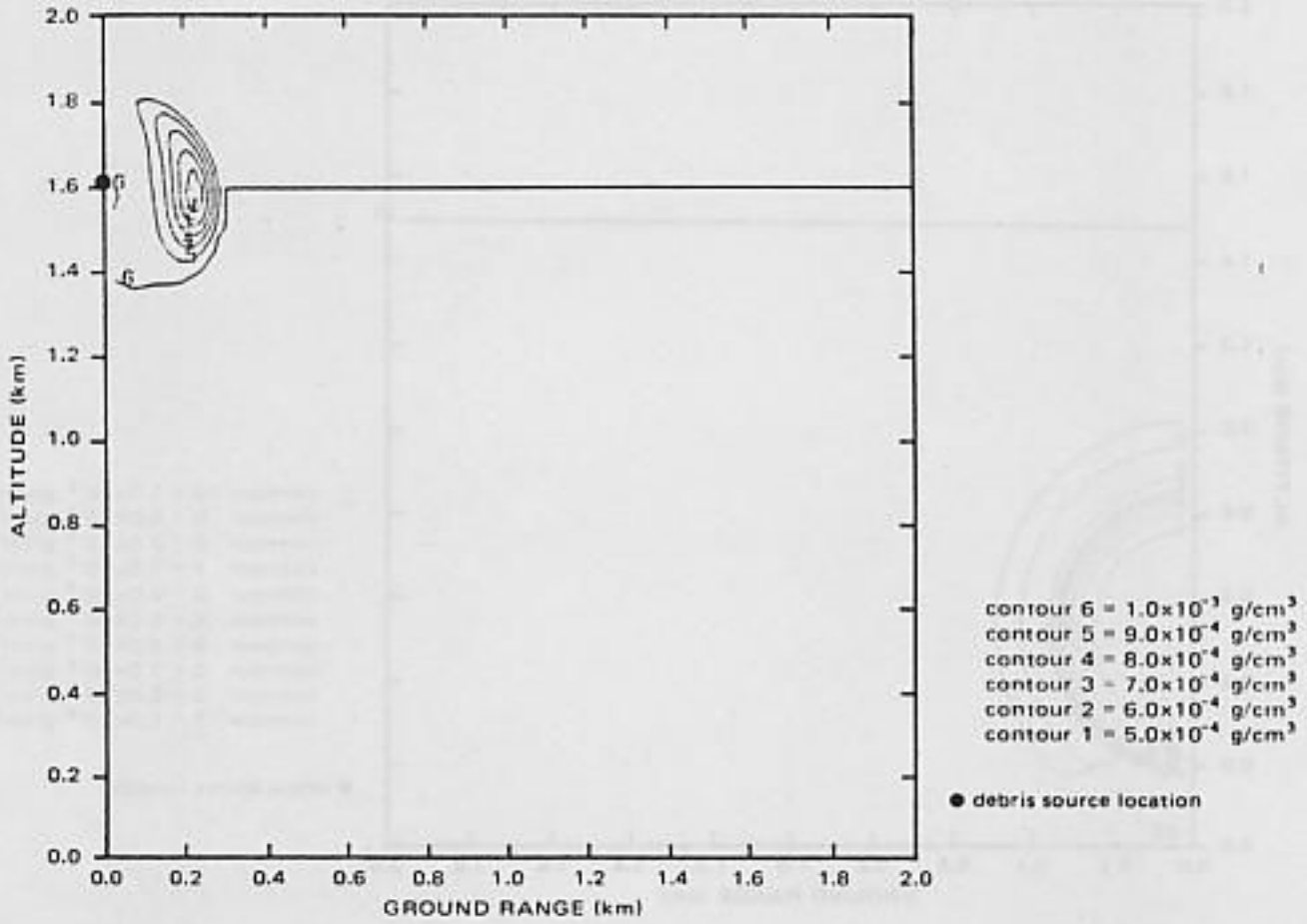

Figure 46. Iso-contours of air density at Hiroshima 20.004 seconds after the explosion

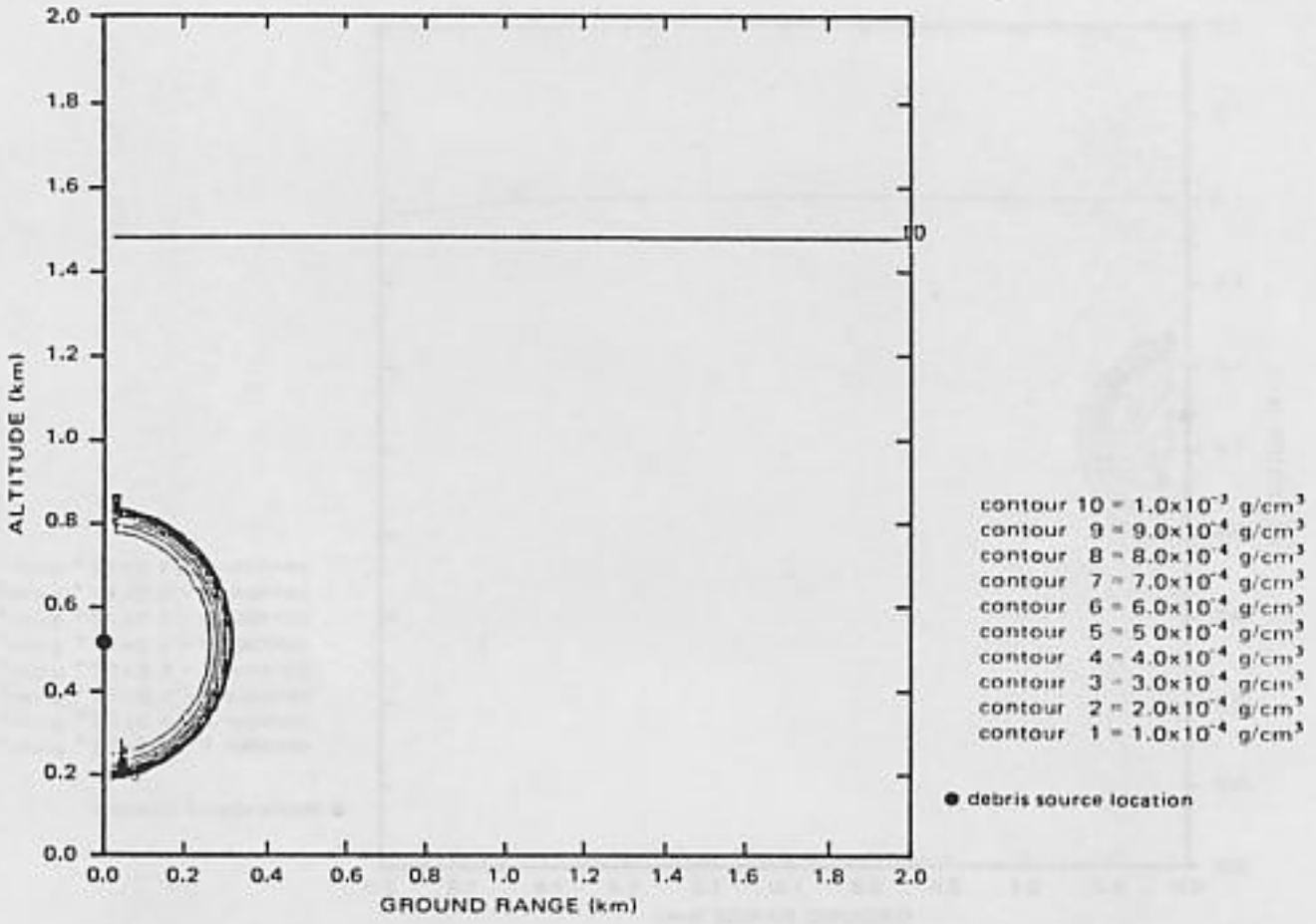

Figure 47. Iso-contours of air density at Nagasaki 0.354 seconds after the explosion

Figure 48. Iso-contours of air density at Nagasaki 1.034 seconds after the explosion

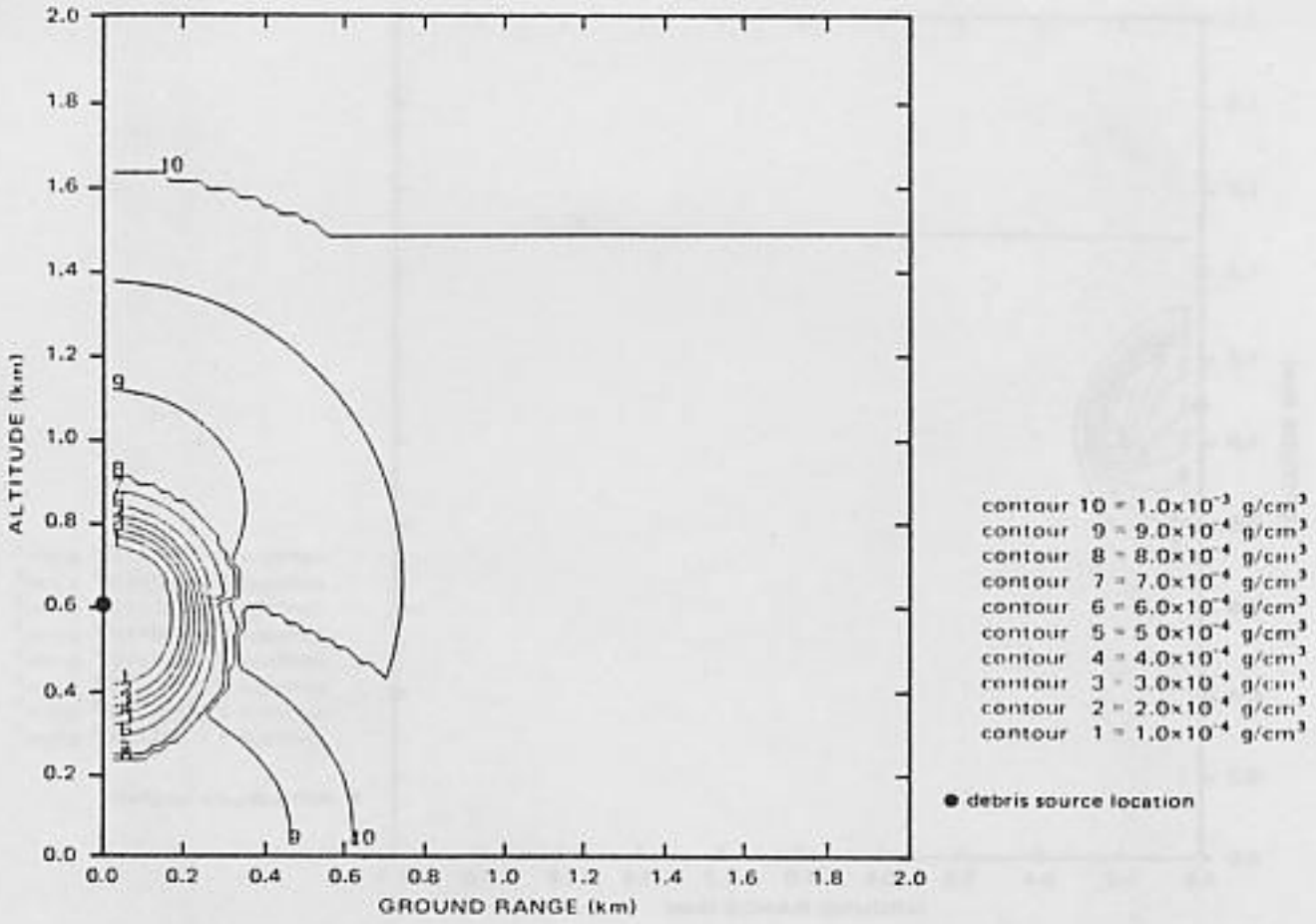

Figure 49. Iso-contours of air density at Nagasaki 2.028 seconds after the explosion

Figure 50. Iso-contours of air density at Nagasaki 3.067 seconds after the explosion

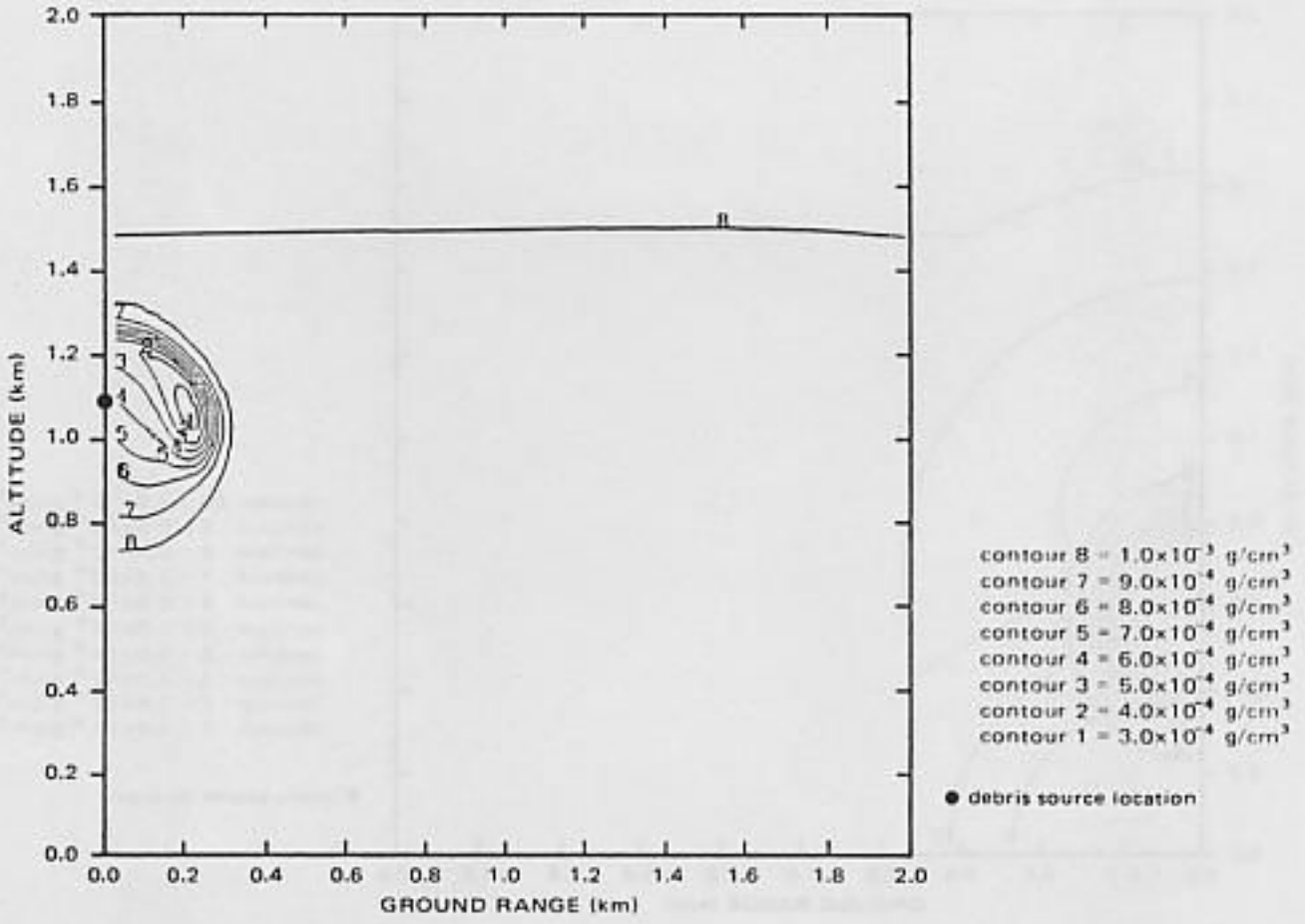

Figure 51. Iso-contours of air density at Nagasaki 9.725 seconds after the explosion

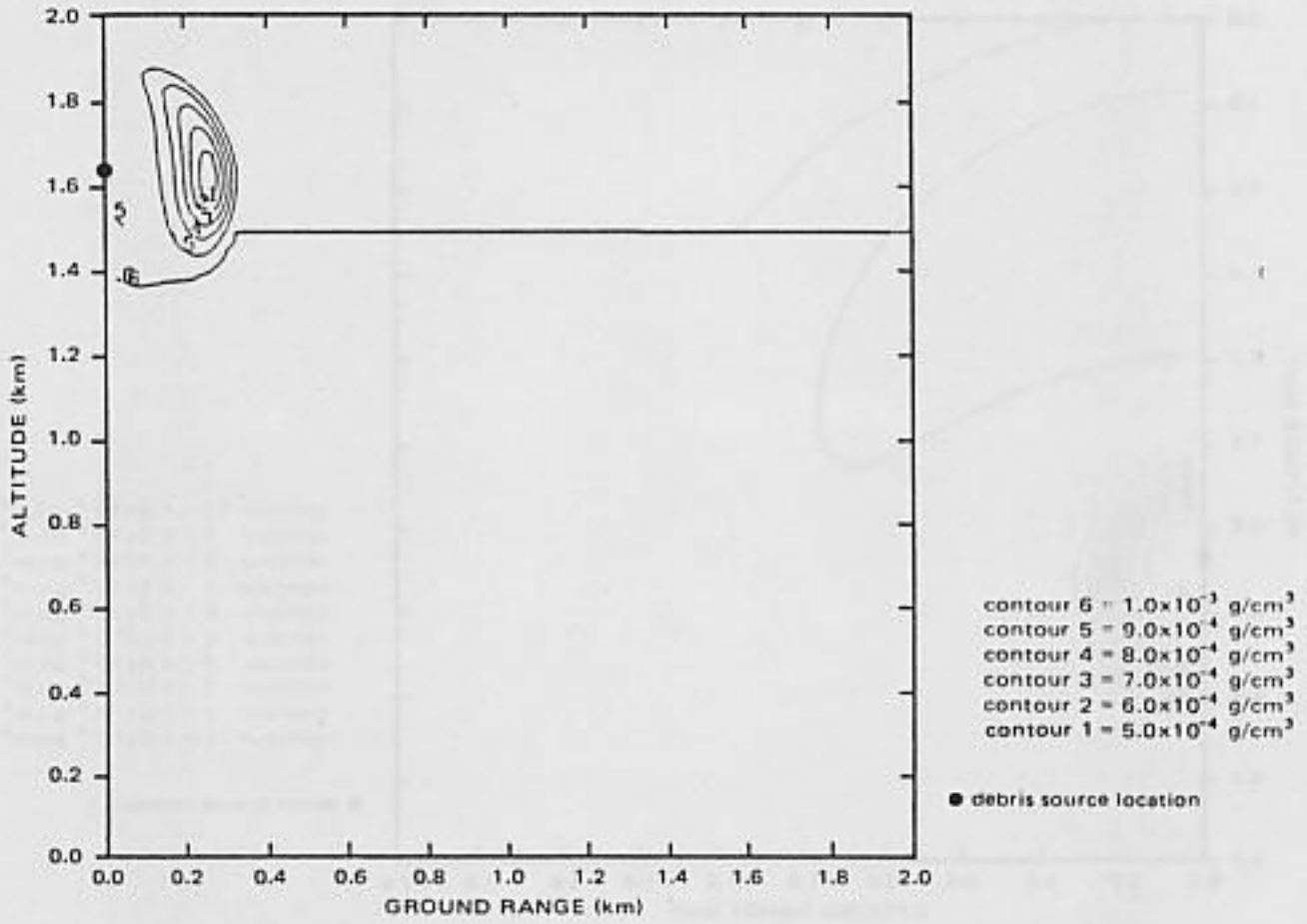

Figure 52. Iso-contours of air density at Nagasaki 20.004 seconds after the explosion

has not yet interacted with the ground. When this does occur and the reflected shock moves through the fireball, between one and three seconds, the fireball is little perturbed by the event. However, as in the case of the Plumbbob tests, a torus has formed by 10 seconds and the cloud has risen substantially by 20 seconds.

With the constraints of the current delayed-radiation model, the effect of moving the source along the axis of the system is rather small, as shown in the exposure rate calculations for Hiroshima (Figures 53 to 56) and Nagasaki (Figures 57 to 60).

As a reminder in examining these figures, the heavy solid line is the nominal source location, the dotted line is the low and the dashed line is the high. The light solid line is the extreme case of no ground-shock interaction, which produces an unrealistic cloud rise and is, therefore, of only academic interest, though it produces only a small increase in exposure.

Tables 11 and 12 give the exposure values at four ground ranges for Hiroshima and Nagasaki, respectively, with and without a moving source. The numbers in parentheses are the ratios of the given values to those for the nominal (static) source location. As

Table 11. The Free-field Kerma due to Delayed Gamma Rays at Hiroshima for the Nominal Source Location and for Several Approximations to a Moving Source

Time (s)	Source Location	Range (m)			
		700	1000	1500	2000
0- 1	N				
1- 3	N	913.90	238.30	26.10	3.33
3-10	N	(1.00)	(1.00)	(1.00)	(1.00)
>10[a]	N				
0- 1	H				
1- 3	NH	833.50	222.10	24.50	3.12
3-10	NL	(0.91)	(0.93)	(0.94)	(0.94)
>10	L				
0- 1	NH				
1- 3	N	920.60	241.00	25.90	3.23
3-10	NL	(1.01)	(1.01)	(.99)	(0.97)
>10	L				
0- 1	N				
1- 3	NH	885.80	236.10	26.05	3.28
3-10	N	(0.97)	(0.99)	(1.00)	(0.98)
>10	L				

[a]Greater than 10 seconds.

noted previously, there is no unambiguous source location model. It is expected that such a model would be a function of yield and burst height. Nevertheless, given the three location variations examined, none change the results by more than 10%. Given the high altitude of the Hiroshima and Nagasaki explosions together with their low yield, the third source-movement sequence, consisting of nominal, nominal-high, and nominal and low, is probably the most likely. It produces total exposures virtually identical to the nominal case. However, it does redistribute the exposure slightly in time. Multiplicative factors were calculated using

Table 12. The Free-field Kerma due to Delayed Gamma Rays at Nagasaki for the Nominal Source Location and for Several Approximations to a Moving Source

Time (s)	Source Location	Range (m)			
		700	1000	1500	2000
0- 1	N				
1- 3	N	1818.00	420.50	41.01	4.84
3-10	N	(1.00)	(1.00)	(1.00)	(1.00)
>10[a]	N				
0- 1	H				
1- 3	NH	1660.00	397.10	38.88	4.69
3-10	NL	(0.91)	(0.94)	(0.95)	(0.97)
>10	L				
0- 1	NH				
1- 3	N	1826.80	423.60	40.92	4.81
3-10	NL	(1.00)	(1.01)	(1.00)	(0.99)
>10	L				
0- 1	N				
1- 3	NH	1755.20	412.80	40.96	4.86
3-10	N	(0.97)	(0.98)	(1.00)	(1.00)
>10	L				

[a]Greater than 10 seconds.

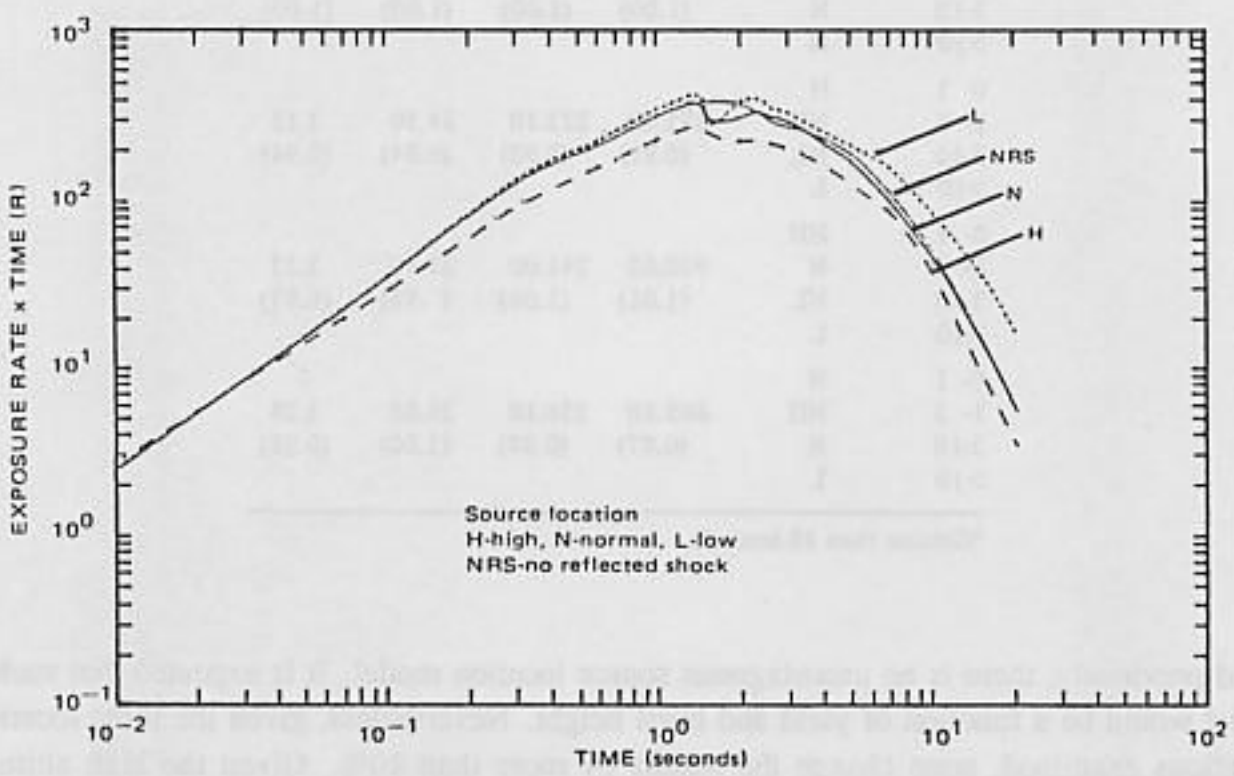

Figure 53. Calculated exposure rates at 700 m ground range at Hiroshima for three source locations along the eenterline and with and without a ground-reflected shock wave

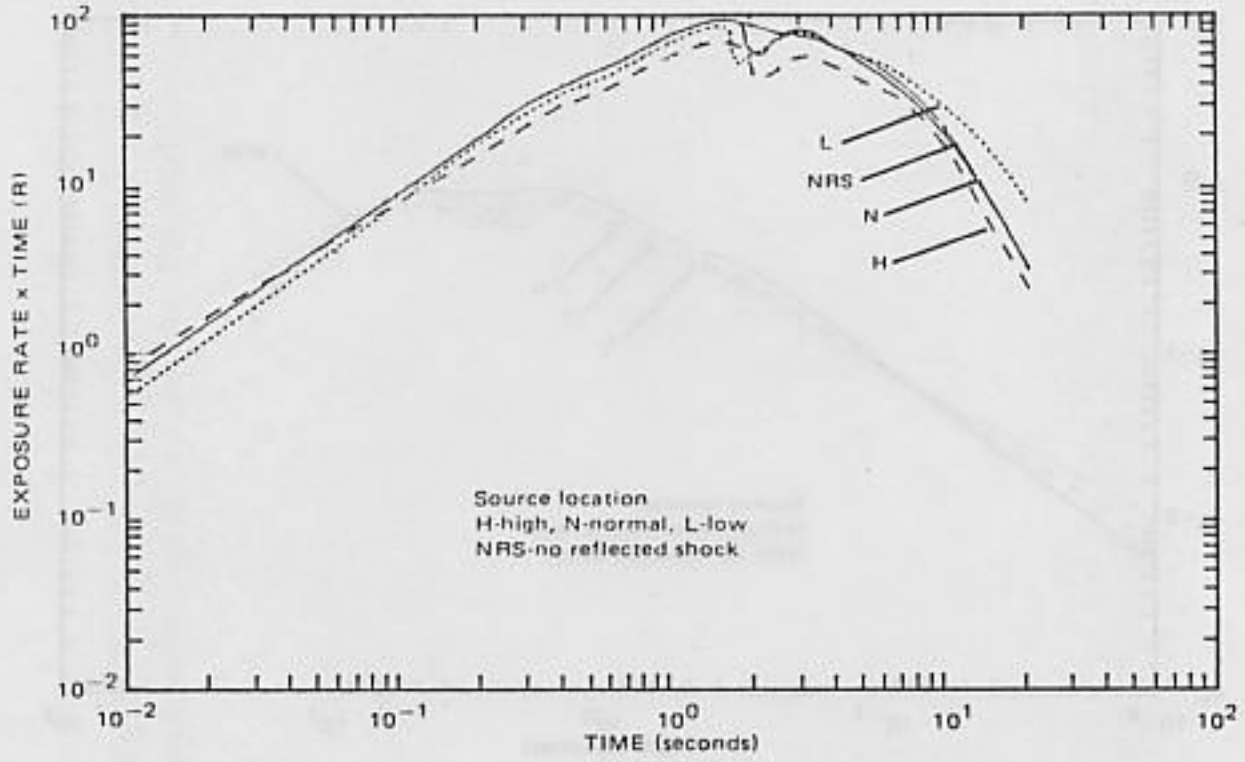

Figure 54. Calculated exposure rates at 1000 m ground range at Hiroshima for three source locations along the centerline and with and without a ground-reflected shock wave

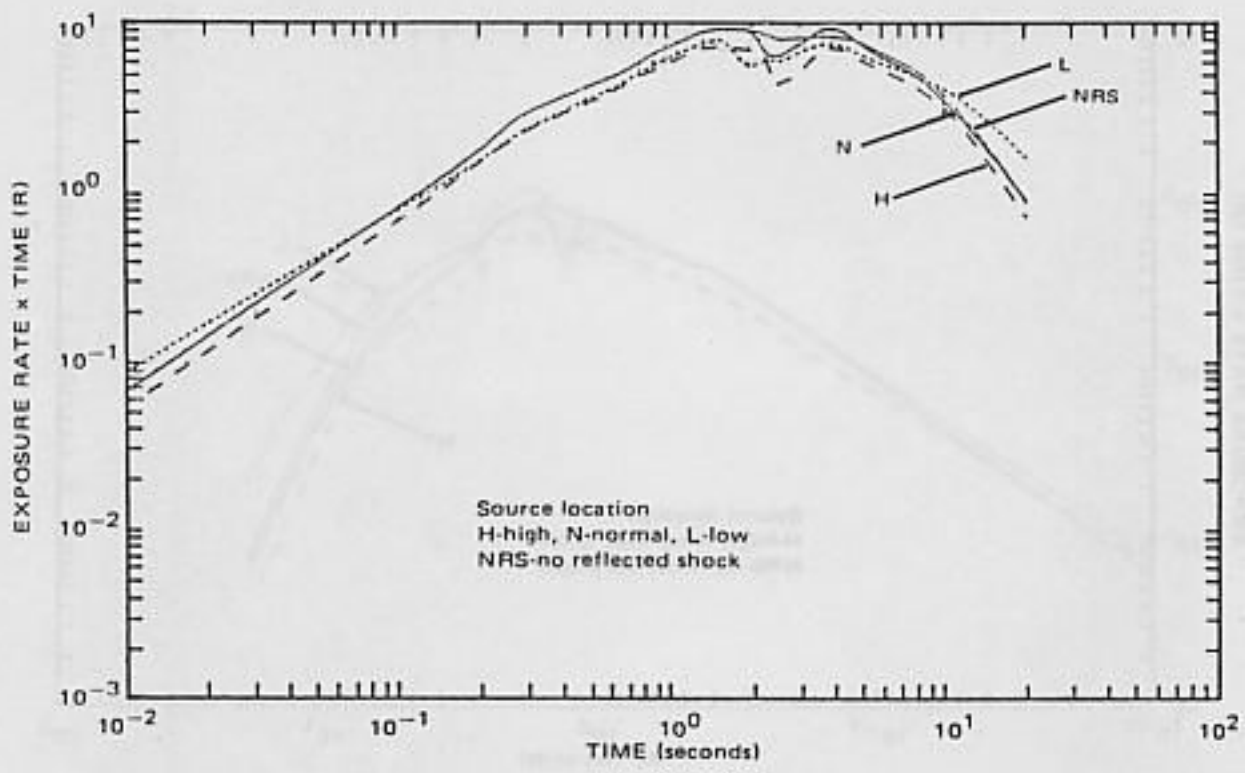

Figure 55. Calculated exposure rates at 1500 m ground range at Hiroshima for three source locations along the centerline and with and without a ground-reflected shock wave

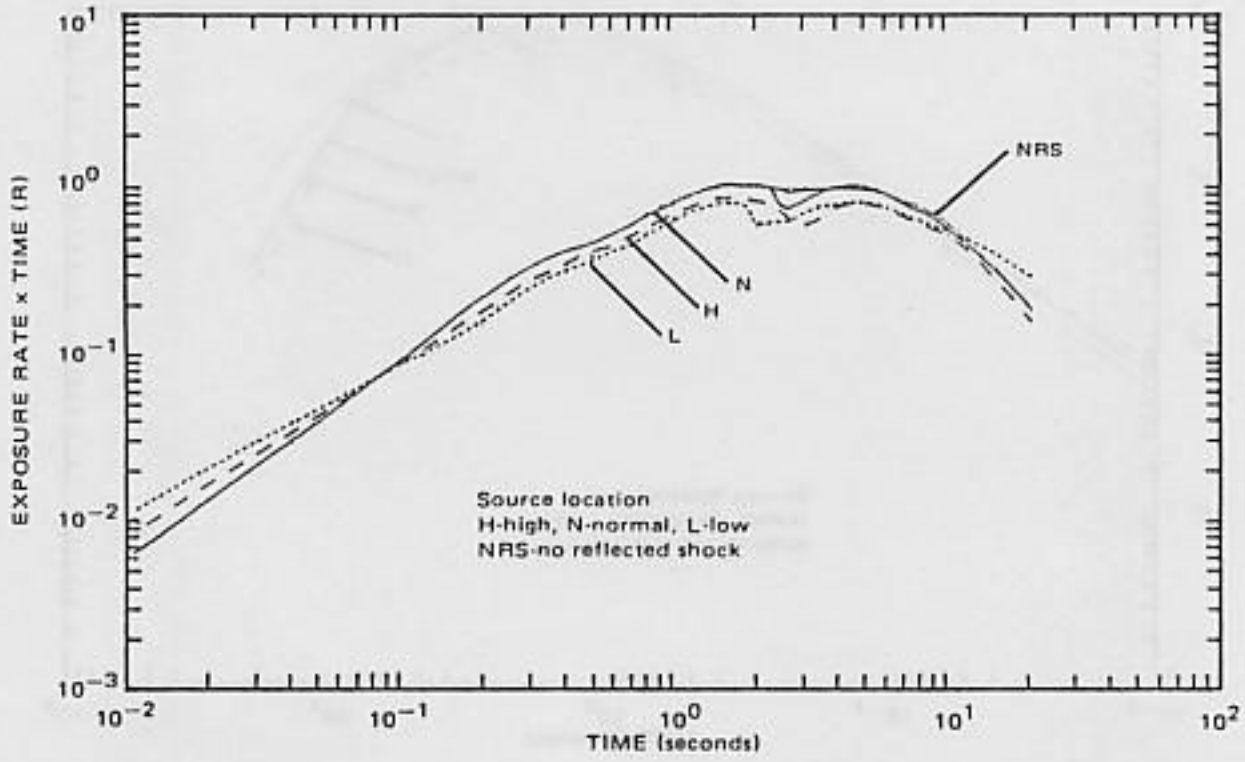

Figure 56. Calculated exposure rates at 2000 m ground range at Hiroshima for three source locations along the centerline and with and without a ground-reflected shock wave

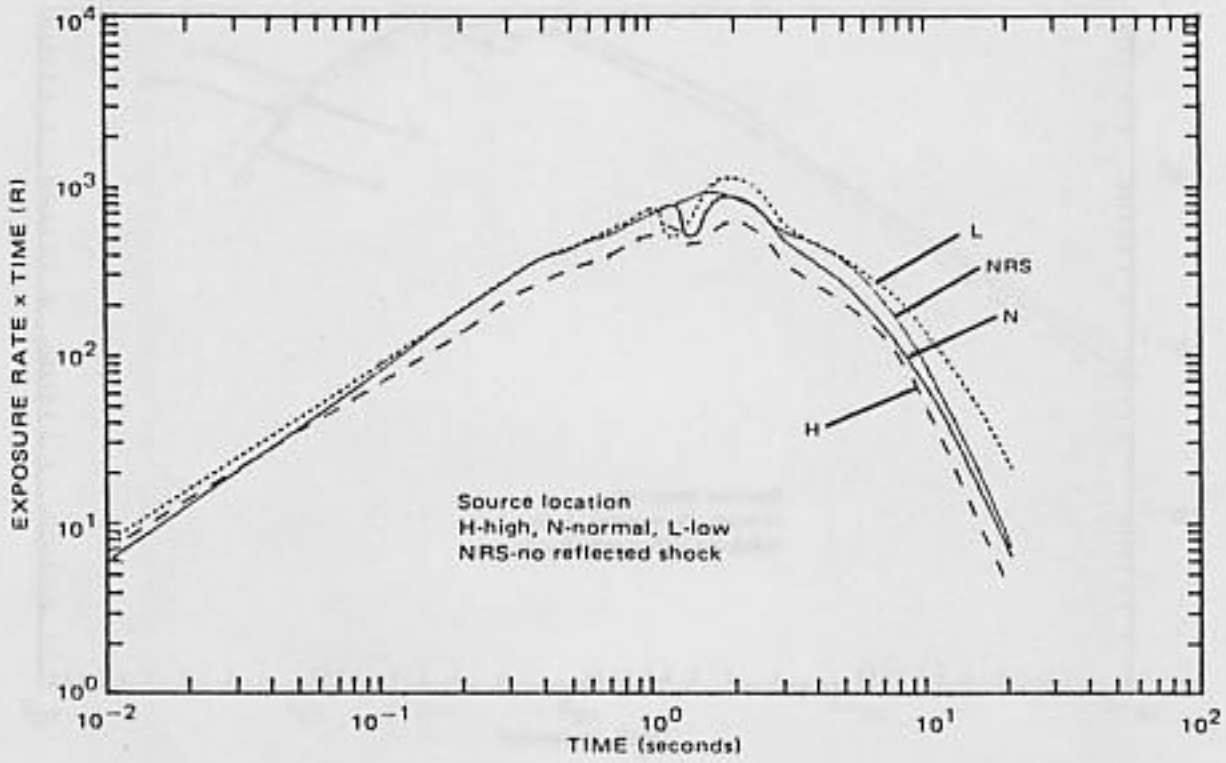

Figure 57. Calculated exposure rates at 700 m ground range at Nagasaki for three source locations along the centerline and with and without a ground-reflected shock wave

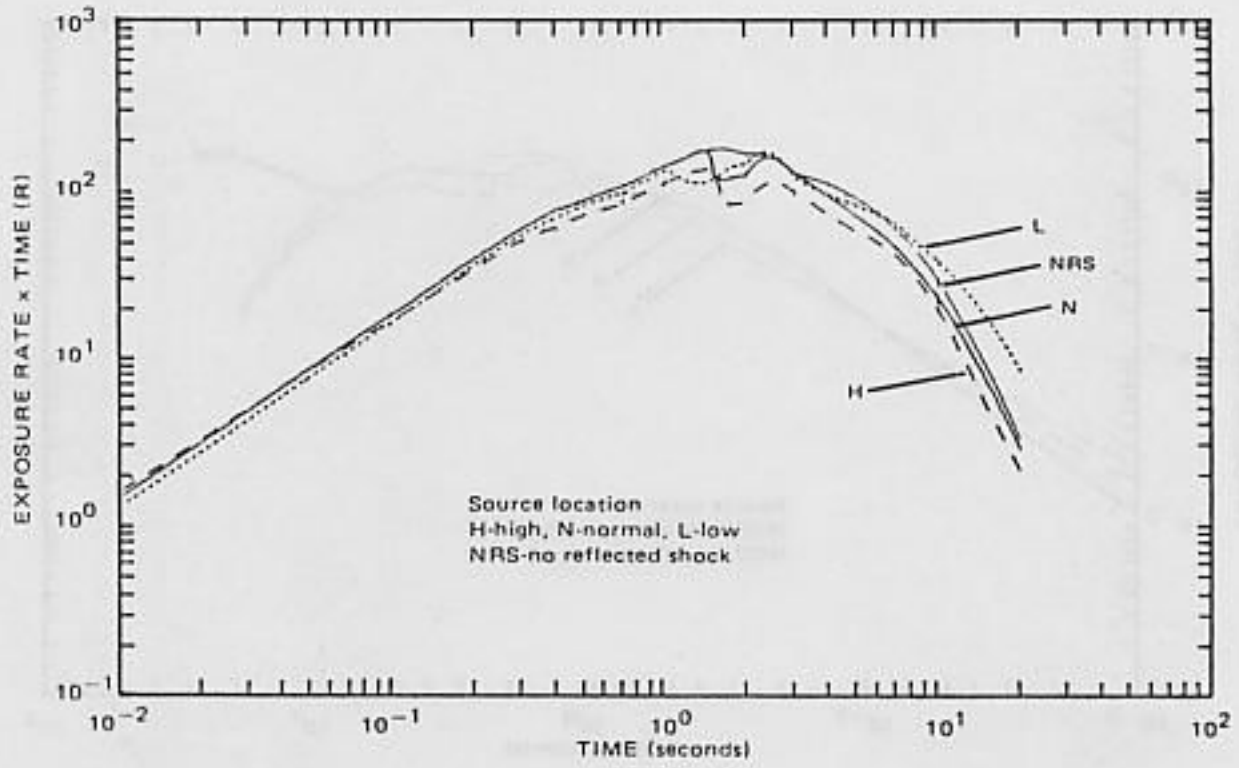

Figure 58. Calculated exposure rates at 1000 m ground range at Nagasaki for three source locations along the centerline and with and without a ground-reflected shock wave

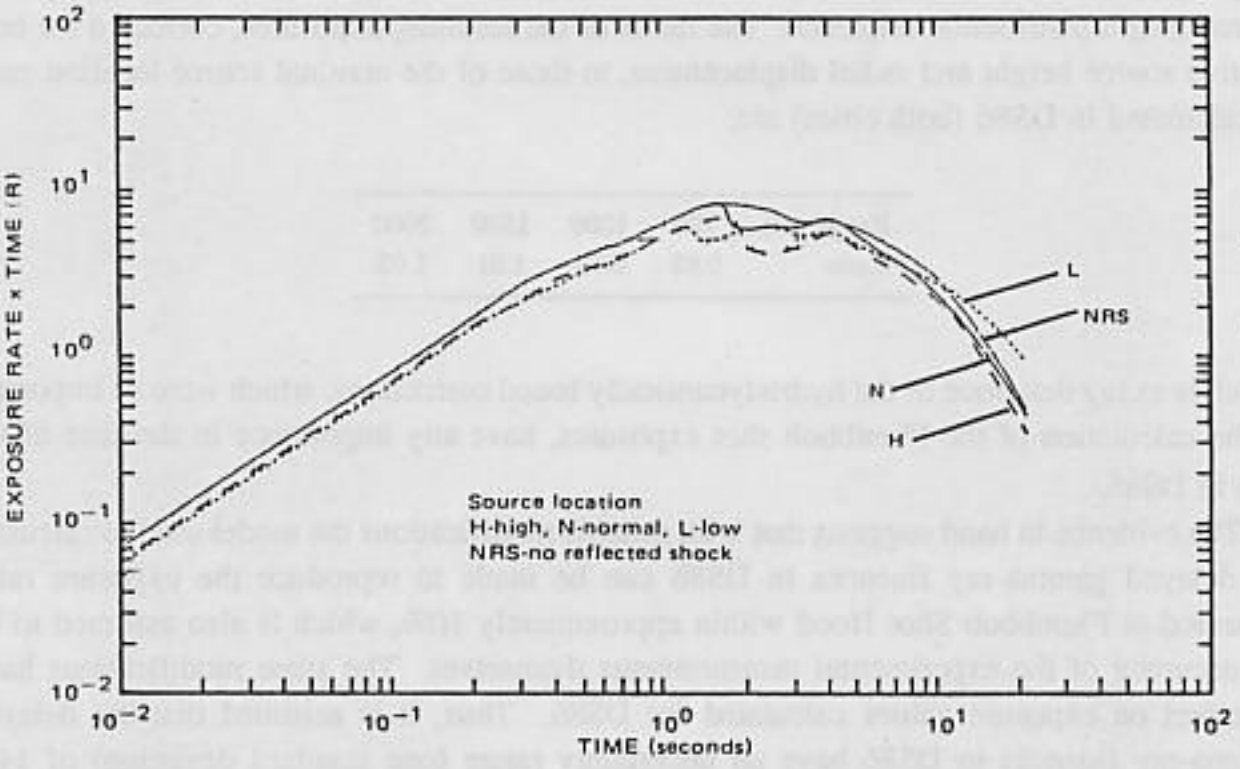

Figure 59. Calculated exposure rates at 1500 m ground range at Nagasaki for three source locations along the centerline and with and without a ground-reflected shock wave

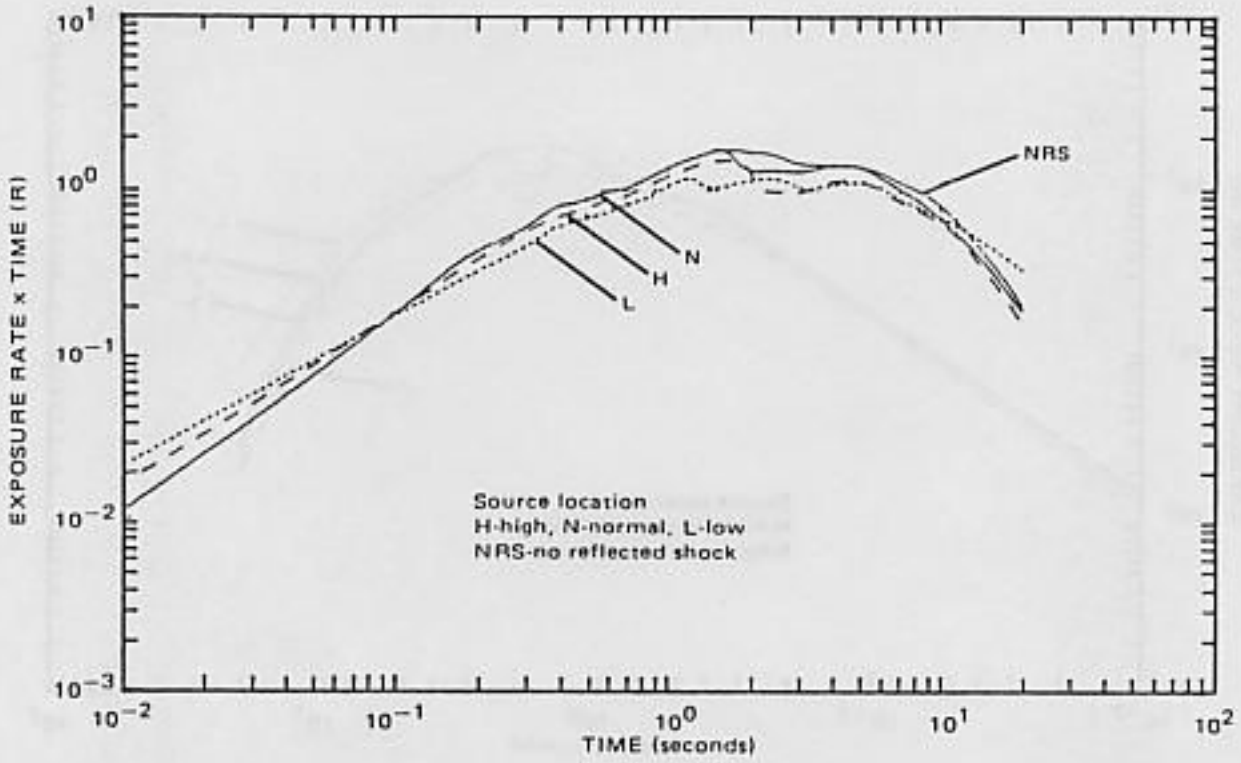

Figure 60. Calculated exposure rates at 2000 m ground range at Nagasaki for three source locations along the centerline and with and without a ground-reflected shock wave

simple point-kernel techniques to account for the radial displacement of the source in that source-height distribution sequence. The ratios of the resulting exposures, corrected for both relative source height and radial displacement, to those of the nominal source location case, as calculated in DS86 (both cities) are:

Range (m)	700	1000	1500	2000
Ratio	0.98	0.99	1.01	1.02

which is to say that none of the hydrodynamically based corrections, which were so important to the calculation of the Plumbbob shot exposures, have any importance in the case of the data in DS86.

The evidence in hand suggests that with suitable modifications the model used to calculate the delayed gamma-ray fluences in DS86 can be made to reproduce the exposure rates measured at Plumbbob Shot Hood within approximately 10%, which is also assumed to be the accuracy of the experimental measurements themselves. The same modifications have no effect on exposure values calculated for DS86. Thus, it is assumed that the delayed gamma-ray fluences in DS86 have an uncertainty range (one standard deviation) of 14% about a value that is 5% greater than the DS86 value. The offset accounts for a suspected but unproven discrepancy between the number of gamma rays produced by thermal- and fast-neutron induced fission. Thus, the DS86 delayed gamma rays are postulated to have an uncertainty range (one standard deviation) of +19% to -9%.

References

1. Maienschein, F. C., Peele, R. W., Zobel, W., and Love, T. A., 1958. Gamma rays associated with fission. In Second United Nations International Conference on the Peaceful Uses of Atomic Energy, vol. 15. New York: United Nations.
2. Maienschein, F. C., 1968. Prompt-fission gamma rays. In Engineering Compendium on Radiation Shielding, R. G. Jaeger, Ed., vol. 1. Vienna: International Atomic Energy Agency.
3. Fisher, P. C. and Engle, L. B., 1962. Energy and Time Dependence of Delayed Gammas from Fission. Los Alamos, NM: Los Alamos National Laboratory, report LAMS-2642.
4. Fisher, P. C. and Engle, L. B., 1964. Delayed gammas from fast-neutron fission of ^{232}Th, ^{233}U, ^{235}U, ^{238}U, and ^{239}Pu. Phys. Rev. 134:B796-B816.
5. Dickens, J. K., Love, T. A., McConnell, J. W., and Peelle, R. W., 1980. Fission-product energy release for times following thermal-neutron fission of ^{235}U between 2 and 14000 s. Nucl. Sci. Eng. 74:106-129.
6. Dickens, J. K., Love, T. A., McConnell, J. W., and Peelle, R. W., 1981. Fission-product energy release for times following thermal-neutron fission of ^{239}Pu and ^{241}Pu between 2 and 14000 s. Nucl. Sci. Eng. 78:126-146.
7. Akiyama, M. and An, S., 1982. Measurements of fission-product decay heat for fast reactors. In Nuclear Data for Science and Technology, Bockoff, Ed.
8. England, T., 1985. Private communication. Las Alamos National Laboratory.
9. Haywood, F. F., Auxier, J. A., and Loy, E. T., 1964. An Experimental Investigation of the Spatial Distribution of Dose in an Air-over-Ground Geometry. Washington, DC: Department of Energy (U. S. Atomic Energy Commission report CEX-62.14).
10. Gritzner, M. L., 1975. A User's Manual for the Two-Dimensional Discrete Ordinates Code DOTSAI. Schaumberg, IL: Science Applications International Corporation, report SAI-75-74-HU.
11. Roussin, R. W., Weisbin, C. R., White, J. E., Greene, N. M., Wright, R. Q., and Wright, J. B., 1980. Vitamin-C: The CTR Processed Multigroup Cross-Section Library for Neutronics Studies. Oak Ridge, TN: Oak Ridge National Laboratory, report ORNL/RSIC-37.
12. Huszar, L., Woolson, W. A., and Straker, E. A., 1976. Version 4 of ATR (Air Transport of Radiation). Washington, DC: Defense Nuclear Agency, report DNA 3995F.
13. Weisbin, C. R., Roussin, R. W., Wagschal, J. J., White, J. E., and Wright, R. O., 1979. An ENDF/B-V Multigroup Cross Section Library for LMFBR Core and Shield, LWR Shield, Dosimetry and Fusion Blanket Technology. Oak Ridge, TN: Oak Ridge National Laboratory, report ORNL- 5505.
14. Bartine, D. E., Knight, J. R., Pace, J. V., III, and Roussin, R. W., 1977. Production and Testing of the DNA Few Group Coupled Neutron-Gamma Ray Cross-Section Set. Oak Ridge, TN: Oak Ridge National Laboratory, report ORNL/TM-4840.
15. Rhoades, W. A., 1974. Development of a Code System for Determining Radiation Protection of Armored Vehicles (The VCS Code). Oak Ridge, TN: Oak Ridge National Laboratory, report ORNL-TM-4664.
16. Engle, W. W., Jr., 1967. A User's Manual for ANISN, A One-Dimensional Discrete Ordinates Transport Code with Anisotropic Scattering. Oak Ridge, TN: Union Carbide Corporation, report K-1693.
17. Straker, E. A., Scott, W. H., and Byrn, N. R., 1972. The MORSE Code with Combinatorial Geometry. Washington, DC: Defense Nuclear Agency, report DNA 2860T.
18. Dean, D., 1982. Private communication. McDonnell-Douglas Corporation.
19. Needham, C. E. and Wittwer, L. A., 1975. Low Altitude Multiple Burst (LAMB) Models. Albuquerque, NM: Air Force Weapons Laboratory, report AFW-DYD-TN-75-2.
20. Carp, G., Johnson, O., Baldwin, T., Larrick, R., Markow, B., Lavicka, F., and McAfee, W., 1961. Initial Gamma Radiation Intensity and Neutron-induced Gamma Radiation of NTS Soil. Washington, DC: Defense Atomic Support Agency, report WT-1414.

21. Ehrlich, M., 1984. Energy dependence of instrument sensitivity. Paper presented at the Workshop on Radiation Survey Instruments and Calibration, National Bureau of Standards.

22. Dudziak, W. F., 1974. Photographic Atlas of Event Climax. Washington, DC: Defense Nuclear Agency, report DNA 3326T (classified).

23. Storm, E., 1952. Operation Buster-Jangle Project 10.5 Gamma Radiation Exposure as a Function of Distance. Los Alamos, NM: Los Alamos National Laboratory, report WT-408.

24. Storm, E., 1952. Gamma ray exposure as a function of distance. In Operation Ranger, Volume 4, Program Reports - Gross Weapon Measurements. Los Alamos, NM: Los Alamos National Laboratory, report WT-201.

25. Storm, E., 1981. Gamma vs distance LA film badge correction factors for the 1951-55 Nevada tests. Los Alamos, NM: Los Alamos National Laboratory, memo to John Malik.